

ABSTRACT

MISHRA, KAUSHAL KISHOR: Development of a Thermal Neutron Imaging Facility at the N.C. State University PULSTAR reactor. (Under the guidance of Prof. Ayman I. Hawari)

A Thermal Neutron Imaging facility is being set up at the PULSTAR reactor at North Carolina State University. The PULSTAR is an open pool type light water moderated research reactor with a full power of 1-MWth and fuel that is enriched to 4% in U-235. It is equipped with 6 Beam Tubes (BT) to extract the radiation out of the reactor core. BT #5 is being used for the neutron imaging facility.

Neutron imaging has expanded rapidly as a means of Non-Destructive Testing of materials. It offers some very explicit advantages over the usual γ -ray (or x-ray) imaging. Neutron cross-sections, being almost independent of the atomic number (Z) of the material, result in neutron imaging being capable of discerning materials of similar Z and/or low Z materials even when they are present inside high Z surroundings. Also, hydrogen, which is a very important element in determining the properties of materials, can be imaged even if present in minute quantities due to its significant neutron scattering and absorption cross-sections. Neutrons also offer the advantage of being capable to differentiate between isotopes of an element. Furthermore, radioactive materials which cannot be imaged using photons due to fogging of the detector can be imaged with neutrons using the transfer technique.

The facility at the PULSTAR is intended to have both radiographic and tomographic capabilities. The radiography capabilities include using conventional film, digital image plate systems, as well as a real-time radiography system. In the present work the design of the facility is being presented. The collimator constitutes the major part of the imaging

facility. The collimator design and its performance were simulated using MCNP. The designed collimator has a poly-crystal bismuth filter that is 4-inches in length, and a single crystal sapphire filter that is 6-inches in length. To aid in the design process, the bismuth and sapphire thermal neutron scattering cross-sections were calculated and implemented as libraries that can be used in MCNP calculations. The L/D of the system ranges from 100 to 150. The filter length can be changed to vary the estimated neutron flux from 1.8×10^6 to 7×10^6 n/cm².sec at full power with a sub-cadmium neutron content >98% as estimated by the MCNP simulations. Using the designed collimator, the beam divergence angle is 2° which translates to a beam size of 35-cm at 6-m from the aperture.

Radiography and tomography simulations were also performed using MCNP and the effect of scattering was observed in the image. In addition, the Point Spread Function (PSF) for different detection systems was simulated and the corresponding resolution defined by the FWHM for film, image plate and real time detection systems was obtained and found to be between 33 to 50-μm, 106 to 118-μm and 113 to 118-μm respectively. The results obtained were in good agreement with the measurement performed using a 25-μm thick gadolinium foil. The designed beam was evaluated using the standards of the American Society of Testing and Materials (ASTM) and it was found that the designed beam achieves quality I^A ranking. Initial radiographs using the facility have been taken and are presented. The real-time radiography and tomography system will be setup in the near future.

**Development of a Thermal Neutron Imaging Facility at the
N.C. State University PULSTAR reactor**

By

Kaushal Kishor Mishra

A thesis submitted to the Graduate Faculty of
North Carolina State University
in partial fulfillment of the
requirements for the Degree of
Master of Science

NUCLEAR ENGINEERING

Raleigh

2005

BBBhattacharyya



Ayman Hameed
Chair of Advisory Committee

Dedication

This thesis is dedicated to my beloved Parents

Biography

Kaushal Kishor Mishra was born February 15th 1981, at Bokaro Steel City, Jharkhand India to Shri Ram Nath Mishra and Smt. Lalita Devi. Bokaro Steel City is a small place in south east of Jharkhand with an Integrated Steel Plant and a population of about one million. The author did his schooling there.

In August 1999, the author began attending Indian Institute of Technology at Kanpur (IITK), India and obtained a degree in Mechanical Engineering in May 2003. During his junior year the author came in contact with Dr. P. Munshi, a professor of nuclear engineering at IITK, and worked under him on beam hardening in computed x-ray tomography. This work made him interested in the field of Radiation Imaging.

In his senior year the author decided to continue his education by going for graduate studies in Nuclear Engineering. The author joined North Carolina State University (NCSU) as a graduate student in Nuclear Engineering in August 2003. He started in the field of Neutron Imaging under Dr. Ayman Hawari perusing his interest in Radiation Imaging.

The work on neutron imaging needed a Thermal Neutron Imaging Facility and therefore the author started setting up a facility at the PULSTAR reactor. In the mean time the author worked to estimate the characteristic of setup facility using MCNP and to develop the necessary background for neutron imaging. In this work the author presents the design of the imaging facility at the PULSTAR that is ready for experimentation.

Acknowledgements

The author would like to extend his deepest gratitude to Dr. Ayman Hawari for his guidance throughout the course of this project. He appreciates the opportunity granted to him with this project and allowing him the ability to work with so many diligent people.

The author would like to express his gratitude to Dr Man Sung Yim and Dr Bibhuti Bhattacharya who agreed to spend their time becoming his thesis committee members and guided him successfully towards its completion.

The author also appreciates the interaction with the technical staff at the National Institute of Standards and Technology (NIST) and their much useful input regarding the experience with neutron imaging at NIST. He would also like to thank Dr. Victor Gillette who worked with him and guided him in the initial phase of the setup. He expresses his sincere gratitude to Mr. Tong Zhou for his assistance with MCNP. The author would also like to express his thanks to Mr. Iyad Al-Qasir who helped him in developing the filter cross-section libraries for MCNP.

Thanks should also be given to Dr. Jianwei Chen for his assistance with MCNP and the preliminary work performed by him while working with the Nuclear Reactor Program of North Carolina State University.

Last but not the least, the author would like to thank Mr. Andrew Cook, Mr. Larry Broussard and Mr. Kerry Kincaid for their much valuable assistance in developing the Neutron Imaging Facility. He also conveys his sincere thanks to all the student operators who assisted in the erection of the facility. Finally the author expresses his thanks to the faculty of the Department of Nuclear Engineering and to fellow colleagues for providing him the opportunity and assistance during his stay at NCSU.

Table of Contents

	Page
List of Tables	vii
List of Figures	viii
Chapter 1 Introduction	1
1.1 Introduction to Neutron Imaging	1
1.2 History of Neutron Imaging.....	6
1.3 Literature Review.....	8
1.3.1 Collimator Design.....	9
1.3.2 Detector Systems	13
Chapter 2 Physics of Neutron Imaging	15
2.1 Neutron Radiograph Formation	15
2.2 Image Detection System	20
2.2.1 Film Detection System.....	20
2.2.2 Image Plate Detection	22
2.2.3 Scintillation Screens and CCD Detection.....	26
2.3 Image Degradation.....	27
2.4 Real-time Neutron Radiography	32
2.5 Neutron Tomography.....	33
Chapter 3 Design of the Neutron Imaging System	38
3.1 PULSTAR Reactor	38
3.2 MCNP Simulation of the Collimator	46
3.2.1 MCNP Code.....	46
3.2.2 Collimator Model.....	46
3.3 Secondary Collimator Test	56
3.4 Collimator Fabrication	60
3.5 Beam Shutter.....	65
3.6 Shielding for the imaging facility	65
3.7 Radiography and Tomography System.....	66
3.7.1 Film and Digital Radiography System.....	66
3.7.2 Real-time Radiography and Tomography System.....	68
Chapter 4 Characterization and Test Results	73
4.1 Simulated Test Results.....	73
4.1.1 ASTM Beam Purity Indicator Radiograph Simulation.....	73
4.1.2 Tomogram Simulation	76
4.1.3 Point Spread Function MCNP Simulation.....	80
4.2 Measurements and Characterization	87
4.2.1 Flux Measurements.....	87
4.2.2 ASTM Standardization	88
4.2.3 Spread Function and Resolution	91

4.3	Comparison with other Neutron Imaging Facilities.....	95
Chapter 5 Conclusion and Future Work.....		97
5.1	Conclusion	97
5.2	Future Work.....	98
5.2.1	Facility Improvements	98
5.2.2	Phase Contrast Imaging	100
References		101

List of Tables

	Page
Table. 3.1. MCNP calculations done for filter length selection.....	55
Table. 3.2. Estimated parameters of the imaging facility.	59
Table. 4.1. Average neutron flux in different regions of BPI.	74
Table. 4.2. ASTM parameters calculated using the simulated BPI.	75
Table. 4.3. The specification of Sample 2 used for tomograph simulation.	78
Table. 4.4 ASTM parameters calculated using image plate PSL values.	90
Table. 4.5. The LSF data for the film.	92
Table. 4.6. The LSF data for the image plate.....	93
Table. 4.7. Comparison table of some NR facilities.	96
Table. 5.1. Neutron wavelength pairs with an equal attenuation coefficient for different materials [89].	99

List of Figures

	Page
Fig. 1.1. Performance of various detection systems [44].	14
Fig. 2.1. Illustration showing the association of various radiation flux quantities with functional planes and system components.	15
Fig. 2.2. Neutron absorption in the neutron converter and the production of secondary radiation.	17
Fig. 2.3. The image plate detection process flow chart [50].	26
Fig. 2.4. A typical point spread function of a radiography system [45].	30
Fig. 2.5. The line spread function associated with a radiography system [45].	31
Fig. 2.6. Different forms of LSF which can be used in radiography [53].	32
Fig. 2.7. Projection data collection geometry in Computed Tomography (a) Parallel Beam Geometry [60] (b) Cone Beam Geometry [61].	34
Fig. 3.1. A schematics of the PULSTAR reactor showing various beam tubes. Beam tube #2 which is through tube is not shown in this figure.	39
Fig. 3.2. The MCNP model of PULSTAR reactor core showing beam tubes 4, 5 and 6.	40
Fig. 3.3. The neutron energy spectrum at the entry of BT #5 as calculated using MCNP.	41
Fig. 3.4. Gamma energy spectrum at the entry of BT #5 as calculated using MCNP.	41
Fig. 3.5. Schematics of aperture location calculation.	48
Fig. 3.6. Sapphire cross-section generated to be used in MCNP. Comparison to the published theoretical and experimental data is shown in the figure.	52
Fig. 3.7. Bismuth cross-section generated to be used in MCNP.	53
Fig. 3.8. The neutron energy spectrum at (a) the source (neutron flux = 2.5×10^{12} n/cm ² .sec), (b) at 6-m image plane without filter (neutron flux = 8.5×10^6 n/cm ² .sec), (c) at 6-m image plane with 4-inches Bi and 6-inches Sapphire filter using free atom cross-section (neutron flux = 5.6×10^3 n/cm ² .sec) (d) at 6-m image plane with 4-inches Bi and 6-inches Sapphire filter using generated bound cross-sections (neutron flux = 1.8×10^6 n/cm ² .sec).	54
Fig. 3.9. The MCNP geometry of secondary collimator.	57
Fig. 3.10. The effect of secondary collimation on the neutron beam.	57
Fig. 3.11. MCNP model of the imaging facility collimator with the beam shutter.	58
Fig. 3.12. Neutron flux image at 6-m from the aperture plane.	59
Fig. 3.13. Flux image at the image plate at 6m from the aperture plane.	60
Fig. 3.14. A sectional view of the assembly drawing of the collimator.	61
Fig. 3.15. The 6-inches sapphire crystal used in the collimator.	63
Fig. 3.16. Bare beam tube #5 of the reactor.	63
Fig. 3.17. The fabricated collimator casing.	63
Fig. 3.18. Inserted collimator casing inside the beam tube.	64
Fig. 3.19. The inserted collimator with the aperture alignment done using laser.	64
Fig. 3.20. The beam shutter for the imaging facility.	66
Fig. 3.21. The image reader and the eraser system for digital radiography.	67
Fig. 3.22. The sample positioning system for real-time radiography and tomography.	69
Fig. 3.23. The camera box and the camera box positioning system.	71

Fig. 3.24. A Schematic of the real-time radiography and tomography setup at the PULSTAR.	72
Fig. 4.1. ASTM BPI test sample.	73
Fig. 4.2. ASTM SI test sample.	73
Fig. 4.3. The MCNP simulated radiograph of BPI. In figure (c) and (d) the inverse log image is the image where $-1/\log(\phi)$ is the neutron flux.	75
Fig. 4.4. Tomographic reconstruction of Sample 1.	77
Fig. 4.5. Imaging and tomographic reconstruction of Sample 2.	79
Fig. 4.6. The PSF obtained with MCNP using a 50- μm grid resolution for object screen distance of 10-mm and L/D of 100 (a) with point source at the center of the square grid and (b) at the boundary of the square grid.	83
Fig. 4.7. Vertical cross-section of the PSF (a) for the point source at the grid center and (b) for the point source at the grid boundary.	84
Fig. 4.8. Modulation transfer function obtained using simulated PSF (a) for the point source at the grid center and (b) for the point source at the grid boundary.	85
Fig. 4.9. Simulated PSF for different detection systems.	86
Fig. 4.10. The neutron flux profile on the image plate.	87
Fig. 4.11. BPI digitized radiograph from film.	89
Fig. 4.12. SI digitized radiograph from film.	89
Fig. 4.13. BPI digitized radiograph from image plate.	89
Fig. 4.14. SI digitized radiograph from image plate.	89
Fig. 4.15. (a) ESF obtained using films and (b) the LSF for the radiographic film.	92
Fig. 4.16. (a) ESF obtained from the image plate and (b) LSF for the image plate.	94
Fig. 5.1. Radiograph of a spark plug at (a) 6.9 \AA (b) 3.2 \AA (c) Division of the two radiographs [89].	99
Fig. 5.2. (a) Contact (b) Phase contrast image of a lead sinker shown between them (c) Contact (d) Phase contrast image of a wasp [91].	100

Chapter 1

Introduction

1.1 Introduction to Neutron Imaging

An image may be defined as a two-dimensional function $f(x, y)$, where x and y are the spatial co-ordinates and the amplitude of f at any pair of co-ordinates (x, y) is called the intensity or the *gray level* of the image at that point. The gray level can be representative of any property of the object whose image has been obtained and depends upon the source which has been used to generate the image. In general there can be different kinds of images of the same object depending upon the source, each representing different physical characteristics of the object. In day to day life what we commonly use is visible light imaging in which the gray level represents the optical intensity at each point of the surface of the object which is being imaged. But apart from this there are many different kinds of imaging depending upon the source such as gamma-ray imaging, x-ray imaging, neutron imaging, infrared imaging, microwave imaging, radio-wave imaging, electron imaging, ultrasound imaging etc.

In the case of neutron imaging the image obtained by passing the neutron beam through the object represents the two dimensional variation of the neutron attenuation characteristics of the object. There is a very basic difference between visible light imaging and neutron imaging. In case of visible light imaging only the information of the surface of the object is represented in the image but in neutron imaging the interior of the object is also depicted. This is because neutrons (being neutral particles) can penetrate objects. Due to

this, neutron imaging, in its most common form, is performed using the transmitted beam contrary to visible light imaging where the reflected beam is used.

Neutron Imaging is being used as a Non Destructive Testing (NDT) and Non Invasive Measurement (NIM) technique since the 1950's. Unlike x-rays, neutrons interact with various materials with very specific cross-sections largely independent of atomic number (Z) of the material. Examples of high absorption cross-section materials include hydrogen and boron while iron has lower neutron cross-sections. Hence with neutron imaging it is possible to image such materials even if they are present in minute quantities in the specimen. This varied nature of interaction of neutrons with matter is due to the fact that neutrons being neutral interact with the nucleus of atoms unlike the photons which interact mainly with electrons. Hence the photon cross-sections increase with the increase in ' Z ' of the material. Due to this it is not possible with photons to see light (low ' Z ') materials in a specimen and also it is difficult to distinguish high ' Z ' materials if the atomic number is not sufficiently different.

But despite the advantages which neutron imaging offers over photons (γ - and x-rays) it also has some difficulties associated with it. The first difficulty associated with the neutron imaging is the availability of neutron sources with high flux. In the case of photons the sources can be obtained or manufactured (x-rays) easily with required flux and it is also not very costly. In the case of neutrons the available sources can be divided into three types: [1]

- Reactor source
- Accelerator-based sources
- Radioactive sources

These sources are arranged in decreasing order of neutron flux. But cost wise, these sources (except radioactive sources which have the least neutron flux comparatively) are significantly more expensive than photon sources. The other problem associated with neutrons source is the “thermalization” of the beam. A neutron is mainly categorized based on its energy into five categories [1]:

- Cold Neutron (below 0.01 eV)
- Thermal Neutron (0.01 to 0.3 eV)
- Epithermal Neutron (0.3 to 10,000 eV)
- Fast Neutron (10 keV to 20 MeV)
- Relativistic (> 20 MeV)

Neutron imaging is performed mainly in the thermal and cold region due to the large cross sections for attenuation and detection in this energy range. The advantages of neutron imaging mentioned above are applicable for thermal and cold neutron beams. Hence the fast neutrons generated from the source must be moderated by some means. Usually hydrogenous material (e.g., water) or graphite is used for this purpose. But this tends to increase the size of the sources and hence decrease their portability.

Although high energy neutrons are being considered presently for imaging purposes with some specific applications, they require substantial shielding. At Lawrence Livermore Laboratory, research experiments have demonstrated the power of using high energy neutrons as a non-destructive inspection tool for evaluating the integrity of thick objects such as nuclear warheads and their components. The experiments conducted at Ohio University show that high energy neutron imaging has a promising potential in probing the structure of

thick objects composed of material that are essentially opaque to x-rays [2]. But fast neutron imaging is not in wide use presently.

The second difficulty associated with the neutron imaging is the imaging technique. In the case of photons the image can be directly taken on a film. But neutrons will not form image directly on a film. Hence, some mechanism is required which converts the neutron signal into photon signal without adding much noise or without reducing the signal strength appreciably. For this purpose a converter screen is used which in principle absorbs the neutrons and emits photons which can be imaged. This extra process tends to add some noise in the image.

The third problem which is associated with neutron source is the radiation dose and shielding concerns. The quality factor for neutrons is 20 times more than that of photons [3]. Therefore, neutrons are potentially more damaging to human tissue than photons. Therefore, the shielding material and shield thickness for neutrons should be considered in more elaborate manner than the photons.

But there are some applications where neutron imaging is the only feasible option to do the testing. One example is the inspection of radioactive materials, a problem which is becoming more prevalent in this nuclear age. The radioactivity of the inspection sample can present problems for conventional radiographic methods because the x-ray films become fogged by the radioactive decay radiation from the sample. For this a special neutron radiographic technique, called the transfer detection method can be used [1]. Additional types of applications become obvious when one appreciates that significant neutron-attenuation differences often occur between isotopes of the same element [4]. Such isotopic differentiation could not be considered with conventional radiographic techniques. Useful

neutron radiographic work in this area has included differentiation between ^{113}Cd and other cadmium isotopes in an irradiated reactor control element [5] and between isotopes of uranium. Also the difference between neutron cross-section of hydrogen and deuterium is used to establish the contrast matching concentration in biological analysis of tissues.

Hydrogen is the lightest element. Photon transmission imaging of hydrogenous materials tends to fail in providing adequate information of hydrogen distribution. The high cross-section for hydrogen makes neutron imaging very attractive for the imaging of hydrogenous materials (which constitute the majority of common materials) like water, living tissues, hydrocarbons etc. The presence of hydrogen can often have a detrimental effect on the mechanical properties of metals. Hydrogen segregation to grain boundaries is thought to play a critical role in embrittlement phenomena [6]. Neutron imaging is very useful in the non destructive testing of materials in which hydrogen segregation and hydride formation takes place in course of time. For example hydride precipitate formation takes place in Zirc-alloy cladding of reactor fuel which is a brittle phase. Also in reactor pressure vessel (RPV) steels hydride formation takes place with radiation exposure. These hydrides in heavy metals could be imaged better by using neutron imaging than x-ray imaging. Neutron imaging can also be used to study the distribution of hydrogen and its isotopes which diffuses in metals like palladium due to electro-transport forces [7].

With the possibility of real-time imaging with neutrons additional applications become evident. The fluid flow visualization of two-phase flow can be done using real-time neutron imaging in different equipment like heat exchangers, fuel cells, boilers etc. [8]. Void fraction calculations can also be done in flowing two phase systems using neutron imaging [9]. Another application of real-time imaging is the imaging of moving parts in a mechanical

system. Computed tomography can also be done to obtain a three dimensional image of the object.

In the recent years, to enhance contrast in the images taken with neutrons the wave particle dual nature of neutrons was used. In this case, along with attenuation differences, phase information is used to enhance the contrast when attenuation contrast is not sufficient (e.g., is the case of adjacent light materials). Therefore, three major areas of advantage can be cited for neutron radiography:

- Contrast differences from x-ray radiography as determined by elemental attenuation differences.
- Possibilities for isotopic differentiation
- Capability to radiographically examine highly radioactive material without the film fogging which is a problem for conventional radiography.

Consequently, with the development of a neutron imaging facility at the PULSTAR reactor we will be able to handle a wide area of NDT imaging and can use the facility for industrial part testing. This facility will be further upgraded to have neutron tomography capabilities in the very near future.

1.2 History of Neutron Imaging

Radiography with neutrons began shortly after the discovery of the neutron in 1932. The initial experiments in neutron radiography were performed in Germany in the late 1930's by H. Kallmann and E. Khun. In the years 1935 to 1938 H. Kallmann and Khun [10] used Ra-Be sources and a small neutron generator at the research laboratory of the I.G. Farben Aktiengesellschaft to develop methods of photographic detection of neutrons. Using these methods, O. Peter [11,12] from the Forschungsanstalt der Deutschen Reichspost was able to

produce radiographs of different objects by using the much higher intensity of an accelerator neutron source. The findings of the study by Kallmann and Khun got published several years after the work was finished and reported in several patents conclusively showing the potential of neutron radiography [10]. Later in 1961 J.P Barton was working in neutron radiography in the Department of Physics at Birmingham University [13]. In United States Harold Watts, Dan Polanski and Harold Berger started communicating and developing this further [13]. In Japan the research on NR started and a series of domestic symposia on neutron radiography were periodically held at the Research Reactor Institute of Koyto University since in 1970 [14]. In 1984, the Research Committee on Neutron Radiography was organized by Science and Technology Agency of the Japanese Government [14]. In 1979 the Neutron Radiography Working Group (NRWG) was constituted under the auspices of the Commission of the European Communities [15]. The main tasks of NRWG were the coordination of common interest activities in the field of neutron radiography and the promulgation of information and knowledge on NR [15]. In 1981, the First World Conference on Neutron Radiography was held in San Diego, California USA. In the conference, it was decided to continue publishing the “International Neutron Radiography Newsletter” (INRNL) with J.C. Domanus as the editor [16]. The first issue of the INRNL appeared in Vol.26, No. 2 of the British Journal of Non-destructive Testing (BJNDT) [16]. By the year 1989 the international neutron radiography community had expanded to include many Asian countries [17, 18, and 19].

The formalization of this existing worldwide community of scientists into the International Society of Neutron Radiology (ISNR) started in 1992 [20]. Following the Fourth World Conference on Neutron Radiography in San Francisco a series of four annual

editions of the International NR Newsletters provided through questionnaires for review, discussion and mailed in votes on the proposed ISNR constitution. The constitution was verified in the Fifth World Conference on NR at Berlin in 1996 [20].

Along with the formalization of the NR as a NDT technique, development was also being made to improve the quality of radiographs obtained by improving the detection system. Detection techniques included films with direct and transfer methods, track-etch systems and electronic techniques like scintillator-camera system, neutron image intensifiers and fast framing systems [21]. The CCD and CMOS camera system introduction improved the real-time radiographic techniques. In recent years photo stimulated luminescence (PSL) has been also demonstrated and applied successfully in detection systems which made digital neutron radiography much more convenient.

In the mean time as progress in neutron radiography was being achieved the organizations were also working for the standardization of the technique for non-destructive testing. There exist ASTM standards for neutron radiography facilities to be standardized [22]. A recent compilation lists 104 established centers for neutron radiography around the world, about 75 of them making use of nuclear reactor sources [21].

1.3 Literature Review

Extensive literature review was done for the design of the neutron radiography and tomography setup and their characteristics at other existing places were thoroughly studied. The imaging techniques and their pros and cons were also reviewed.

1.3.1 Collimator Design

The collimator is the basic component in neutron imaging which decides the quality of the image given the source type and hence collimator designs at the other facilities were reviewed prior to its design for the present facility. In this regard a compilation published by Neutron Radiography Working Group (NRWG) on Collimators for Thermal Neutron Radiography compiled by J.C. Domanus has information about many different types of collimators and also has general guidelines. It consists of collimator design data from 144 publications. The following general aspects of collimator were reviewed from the compilation [23]:

- Geometric Shape of the Collimator
- Materials of the walls and their lining
- Filling of the Collimator
- Shutters and diaphragms at the ends of the collimator.
- Gamma and neutron filters

1.3.1.1 Geometric Shape of the Collimator

The divergent beam collimator is mainly used after the conclusion of Barton in 1967 that divergent beam collimators produce highest resolution [24]. Among them the most commonly used physical form is a truncated cone or pyramid [23]. Conical (truncated cone) collimators have been used in the earlier NR facilities [25, 26, 27, and 28]. A truncated pyramid, either with a square or a rectangular cross-section is also used commonly in collimator design [29]. Collimators with convergent-divergent shape were used in facilities [30, 31]. A divergent collimator can also be constructed with several cylinders with

increasing diameters [23]. Collimators are constructed in segments and then assembled together [32]. The advantage of this type of construction is each single part does not become too heavy. Also each of the segments can be changed separately if required.

1.3.1.2 Materials of the Walls and their lining

The most important item of each collimator is its lining [23]. Unlike charged particles, neutrons cannot be focused [23]. Hence the neutron beam must be collimated by suitable lining in the collimator. To prevent stray neutrons from reaching the radiographed object and to reduce the scattering of neutrons within the collimator the lining must be done with neutron absorbing material. The materials suitable for this purpose are: *boron, cadmium, dysprosium, europium, gadolinium and indium* [23]. The effectiveness of these materials varies with the neutron energy spectrum. The use of boron is recommended because it gets less activated, which facilitates maintenance of the collimator [23]. Generally boron in the form of Boral (B_4C) is used in the collimator. For the aperture 2.5-cm thick Boral plate was used inside the collimator [33]. The collimator lining for many old NR facilities in Europe is given in Ref. 34. The collimator walls are made up of either aluminum (sheet or cast) or stainless steel [23]. The following is the list of material which has been used before in NR facilities for collimator lining [23].

Cadmium

Cadmium + Indium

Cadmium + Indium + Boron

Lead + Cadmium

Polyethylene + Cadmium

Epoxy + Cadmium

Boral + Cadmium + Indium

Cadmium + gadolinium + Indium + Dysprosium + Gold

Boral

Boral + Indium

Lead + Boral

Polyester + Lead + Boral
Boron
Borated Paraffin
Lithium
Lithium fluoride + Lead
Europium oxide (Eu_2O_3) + Aluminum

Boron nitride is also a material which can be used in the collimator as it is easy to machine and therefore unlike boral, complicated shapes can be easily cut of it. As it can be observed there are many choices for the lining of the collimator. There is no explicit advantage of one above the other. Also the thickness of these materials can be varied. Hence suitability must be decided based on the requirement, availability and the cost of the lining.

1.3.1.3 Filling of the Collimator

The neutron beam gets attenuated by 5% per meter in a collimator filled with air [34]. This reduces the flux at the image plane and also results in more scattering of neutrons which produces blurring of the image. This attenuation can be decreased to less than 1% per meter when helium is used as the filling gas [34]. The use of argon as the filling gas has also been reported [35].

1.3.1.4 Shutters and diaphragms

For the shutter, neutron absorbing materials are used so that when the beam is shut by it there is no leakage or scattering of neutrons outside. Materials such as cadmium, boral, masonite, indium, boral + lead have been used in the past [23]. Similarly for the diaphragm (or aperture) boral + aluminum, boral, lead + boral, cadmium + lead + indium eutectic mixture, gadolinium etc. have been used in the past [23]. Different designs of beam shutter are there depending on the requirements of the facility. But two of the basic designs are the rotating drum type and the lifting block type.

1.3.1.5 Gamma and Neutron Filters

To filter out the gamma rays from the beam, lead and bismuth filters are used [23]. As long as 200-mm thick lead and bismuth filters have been used to suppress the gamma rays [32, 36]. Mono-crystals of bismuth of thickness 10 to 15-cm used as a gamma filter have also been reported in the past [37]. The effectiveness of the gamma filter is defined by the N/γ (or N/G) ratio. The ratio varies from facility to facility depending upon the imaging technique followed. But the deleterious effect of gamma rays on the image also depends on the object to be radiographed [38]. The least recommended value is about $5 \times 10^4 \text{ cm}^{-2} \cdot \text{mR}^{-1}$ [39]. But with the development of new gamma insensitive neutron detection plates a ratio less than this can also be justified.

Neutron filters are also required to filter out the fast neutrons from the beam. Single crystal sapphire (Al_2O_3), silicon, quartz and bismuth act as fast neutron filters [40-42]. Sapphire (Al_2O_3) is an effective fast-neutron filter because its transmission for neutrons of wavelengths less than 0.04-nm (500 meV) is less than 3% for a filter thickness of 100-mm [40]. It is also an effective filter of thermal neutrons with wavelengths less than about 0.1-nm, since there is a great density of high-order reflections available to scatter the incident beam [40]. It has been shown that high quality single-crystal sapphire at room temperature is a better fast neutron filter than silicon and quartz even when they are cooled to liquid nitrogen temperature [43]. Single crystal bismuth along with being a gamma filter is also a good neutron filter. A Bi crystal cut along the [111] plane has been shown to have a thermal neutron window [42].

1.3.2 Detector Systems

X-ray films with a neutron absorbing converter screens have been traditionally used as detectors in neutron radiography. Although good spatial resolution ($\sim 20\text{-}\mu\text{m}$) can be obtained from films, there are many drawbacks which demand new detection systems. In addition, there are new detection systems with more flexible performances especially with respect to time resolution, dynamic range and quantitative information from the images. Apart from film, presently the following neutron detection systems are available [44]:

- CCD-camera detection systems observing light from a neutron sensitive scintillator.
- Intensified camera systems, which enhance the sensitivity and deliver other and extended performance features.
- Image plate systems, where the excitation of meta-stable electronic states is used for image formation.
- Amorphous silicon flat panels, which are in direct contact with a scintillation screen.
- Pixel detectors, where neutrons are converted into electrons by means of neutron capture in Gd. Then electrons are registered by pixel detectors (in which processes of ionization and subsequent charge collection takes place). Scintillators with Li-6 doping are preferred in neutron imaging; the other detector systems are mostly using Gd as a converter.

The performance characteristics of the various detector systems have been studied at NEUTRA radiography facility at PSI [44] and are shown in Fig. 1.1.

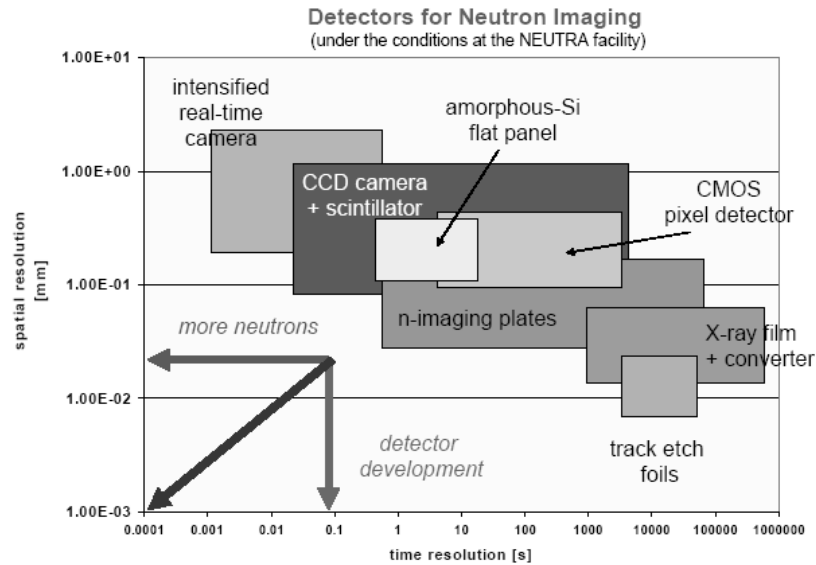


Fig. 1.1. Performance of various detection systems [44].

The advantages of using these detectors over films are:

- High sensitivity and efficiency.
- Fast read-out, high frame rate.
- High linearity and wide dynamic range.
- Reasonable spatial resolution.
- Digital information directly suitable for quantitative evaluation.
- Image post-processing possible.
- Archiving and data transfer.
- Tomography becomes possible.

These advantages make alternative detection systems much more attractive than films.

Chapter 2

Physics of Neutron Imaging

2.1 Neutron Radiograph Formation

In order to provide mathematical and physical basis of the various processes which take place in neutron radiography we need to define the following terms which are depicted in Fig. 2.1.

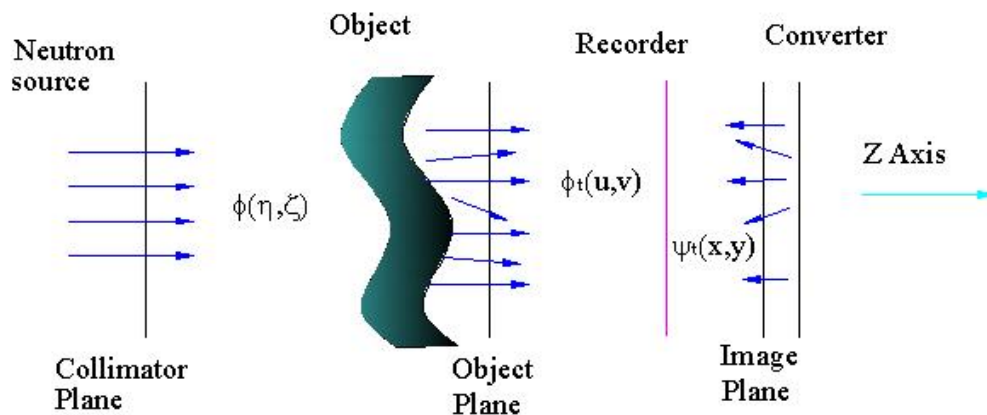


Fig. 2.1. Illustration showing the association of various radiation flux quantities with functional planes and system components.

(η, ζ) = The “collimator” plane associated with the neutron beam from a collimator device; the flux function $\phi(\eta, \zeta)$ on this plane will generally represent the spatial distribution of neutrons which are directed towards the object to be radiographed.

(u, v) = The “object” plane associated with the object of radiographic interest; the associated function $\phi_t(u, v)$ will generally represent the spatial distribution of the neutron beam after its passage through the object.

(x,y) = The “image” plane is associated with the neutron radiographic image; the function $\psi(x,y)$ describes the film blackening secondary radiation emerging from the converter or the photo stimulated luminescence in case of image plates and incident upon the recorder.

The flux $\phi(\eta,\zeta)$ is fully determined by the characteristics of the neutron source and the collimator device. The flux $\phi_t(u,v)$ depends upon the flux $\phi(\eta,\zeta)$ and the object. The function $\psi(x,y)$ represents a flux of a certain type of radiation induced by the neutrons from the $\phi_t(u,v)$ beam captured in the converter. Hence $\psi(x,y)$ is a function of $\phi_t(u,v)$. However the end result is the optical density or gray level $D(x,y)$ on the film or the image plate. The radiographic process can be illustrated by the following sequence of functions:

$$\phi(\eta, \zeta) \rightarrow \phi_t(u, v) \rightarrow \psi(x, y) \rightarrow D(x, y). \quad (2.1)$$

For the object, both neutron scattering and absorption will generally be possible, so the total cross-section at a coordinate z is given by

$$\Sigma_t(z) = \Sigma_a(z) + \Sigma_s(z) \quad (2.2)$$

and the uncollided flux can be written as

$$\phi_{unc}(z) = \phi \exp \left[- \int_0^z \Sigma_t(s) ds \right] \quad (2.3)$$

The total flux ϕ_t can be written using the build up factor $B(\Sigma_s, \Sigma_a, z)$ as

$$\phi_t(z) = \phi B(\Sigma_s, \Sigma_a, z) \exp \left[- \int_0^z \Sigma_t(s) ds \right] \quad (2.4)$$

For materials which possess high scattering cross-section such as hydrogenous compounds, silicon, nickel, copper and other metals build up is most significant [45].

The transmitted flux containing the information about the compositional and geometrical aspects of the object transfers that information to the recorder by means of a conversion technique. The neutrons are absorbed in the converter and the concurrent

production of film blackening radiation (or corresponding radiation/signals for other detector systems) takes place. This secondary radiation field is represented by $\psi(x,y)$. The process of neutron conversion is shown in Fig. 2.2. The distance between the recorder and the converter plane is much less than the cross-sectional dimensions of the recorder, hence, the dependence of the interaction process of $\psi(x,y)$ with the recorder can be safely taken as only function of z . Notice that in this case the assumption is made that the neutrons pass through the recorder unattenuated.

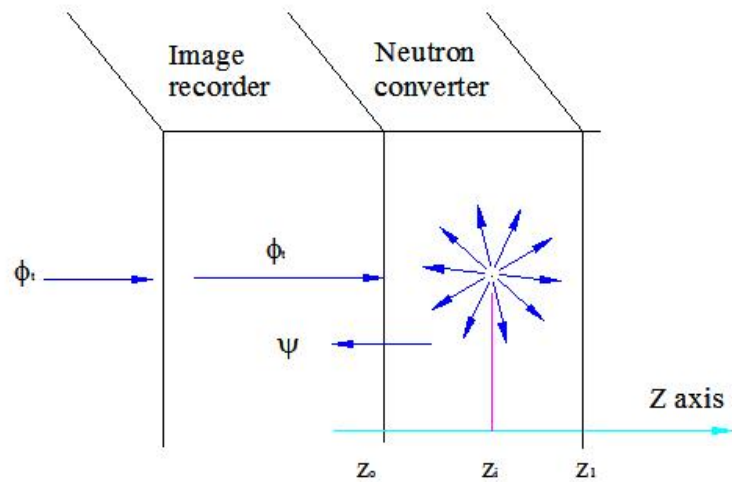


Fig. 2.2. Neutron absorption in the neutron converter and the production of secondary radiation.

The converter plate is a neutron absorbing material hence the neutron flux at the location z_i in the converter is given by

$$\phi(z_i) = \phi_t \exp(-\Sigma_a(z_i - z_0)) \quad (2.5)$$

The neutron absorption rate per unit volume at the coordinate z_i is given by

$$R(z_i) = \Sigma_a \phi_t \exp(-\Sigma_a(z_i - z_0)) \quad (2.6)$$

The yield rate of the secondary radiation at z_i is directly proportional to the reaction rate and can be written as

$$Y(z_i) = \varepsilon_1 \Sigma_a \phi_t \exp(-\Sigma_a(z_i - z_0)) \quad (2.7)$$

where ε_1 is the proportionality constant. The secondary radiation can consist of γ -ray, β particles, α particles or internal conversion electrons. If $P(z_i \rightarrow z_o)$ represents the probability of the secondary radiation reaching to z_o from z_i then the secondary radiation flux entering the recorder can be written as

$$\psi(x, y) = \varepsilon_1 \Sigma_a \phi_t \int_{z_o}^{z_1} \exp[-\Sigma_a(z_i - z_o)] P(z_i \rightarrow z_o) dz_i \quad (2.8)$$

The probability $P(z_i \rightarrow z_o)$ can be written as $\exp[-\mu(z_i - z_o)]$ where μ is the effective attenuation parameter for the secondary radiation in the converter, which also takes into account the fact that emission is over all solid angles. Substituting the expression for $P(z_i \rightarrow z_o)$ in the expression for $\psi(x, y)$ we get the final expression form as

$$\psi(x, y) = \varepsilon_1 \Sigma_a \phi_t \int_{z_o}^{z_1} \exp[-\Sigma_a(z_i - z_o)] \exp[-\mu(z_i - z_o)] dz_i \quad (2.9)$$

which upon integration can be written as

$$\psi(x, y) = \frac{\varepsilon_1 \Sigma_a \phi_t}{(\Sigma_a + \mu)} \{1 - \exp[-(\Sigma_a + \mu)(z_1 - z_o)]\} \quad (2.10)$$

In this equation the role of the various parameters can be seen in controlling the converter response. The energy dependence of the absorption cross-section and the flux can be taken into account to get the energy dependent converter response. It can be observed that the thinner the converter is the better is the converter response if other parameters can be maintained the same. But in reality other parameters also vary with the thickness and hence their rate of change will decide the optimum thickness of the converter plate. Also it should be noted that the emission of secondary radiation is isotropic and hence the x and y coordinates of the interaction point of the secondary radiation with the recorder is not

necessarily the same as that of the secondary radiation emission x and y co-ordinates. This introduces an unsharpness in the recorded image called the converter unsharpness.

The image formation process begins with the secondary radiation flux ψ produced by the converter, being absorbed in the recorder. Two considerations are important in this process:

- The total exposure of the secondary radiation onto the recorder, i.e., the total fluence, and
- Recorder response to the exposure.

The exposure of the recorder at an arbitrary point (x,y) on the image plane is given by the integration of the secondary radiation flux $\psi(x,y,t)$ (considering ψ as time dependent) over exposure time τ_f . If the recorder exposure is defined as $E(x,y)$ then it can be written as

$$E(x, y) = \int_0^{\tau_f} \psi(x, y, t) dt \quad (2.11)$$

The exposure $E(x,y)$ of the recorder generates an optical density function $D(x,y)$ on the recorder. The relationship between $D(x,y)$ and $E(x,y)$ depends upon the type of recorder, the exposure time, the type of secondary radiation emitted by the converter and the development method (for films) or readout method (for electronic sensors) of the recorder. This relationship is known as the characteristic curve of the recorder. The linearity in the characteristic curve over the wide range of the exposure is a highly desired feature in the recorder. The range of exposure over which the curve is linear is called the *latitude* of the recorder. The range of optical density variation which is produced in the *latitude* is called the *dynamic range* of the recorder. In the case of digital detection the dynamic range can also be specified by the number of gray levels which is used. The recorder should be used in this range to get the optical density which is directly proportional to the amount of exposure

or else the precise characteristic curve should be known. But in no situation it should be allowed to saturate because after that optical density becomes constant and hence no differentiation can be achieved between different exposures of the recorder due to different sample composition.

2.2 Image Detection System

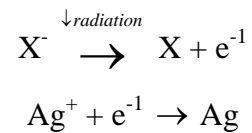
Historically x-ray film with a converter screen has been used as the image detection system. But with the development of digital radiography techniques many other detection techniques have evolved as has been discussed in the literature review presented in chapter 1. Here the basic physics of film, image plates and scintillation screens with CCD will be presented as these systems will be primarily used in the present facility.

2.2.1 Film Detection System

The efficient use of a photosensitive emulsion for information collection and storage requires a full knowledge of its performance characteristics. The photo sensitive emulsions are usually made up of silver halide grains. Performance data required from film is broadly categorized as: speed, contrast, spectral response and resolving power [46]. The speed and contrast of a film are usually presented as its ‘characteristic curve’ – a plot of density against exposure. The use of an intensifying screen in conjunction with the films is necessary since neutrons usually have insufficient direct effect on the emulsion. The intensifying screens absorb neutrons and emit ionizing radiation to which film is highly sensitive. A latent image is formed on the film when it is exposed to ionizing radiation, which is subsequently rendered visible by development of the film. Development is the process of amplifying the latent image. All silver halide crystals have a small probability of developing without

exposure to ionizing radiation. Exposure of crystals induces a chemical change in them which increases their probability of development.

Silver halide crystals have *frenkel* defects in them which are the sites of latent image formation [47]. Chemically the process can be written in the following two steps:



Here X denotes the halide atom which can be chlorine, bromine, iodine etc. The X^- and the Ag^+ are the frenkel ion pairs. The initial silver formation is an unstable process and can be reversed due to decay of the silver atom, which produces electrons that recombine with the halide ions. Halogen atom formed in the process can also attack the silver atom. Therefore, gelatine is used in the emulsion, which accepts halogen atom. This process of decay affects the validity of the reciprocity law as will be explained later on and can have an effect on the imaging parameters such as effective loss of speed of the film and increase in contrast [47].

The spectral response is the efficiency of the film against radiation energy and is controlled by the absorption properties and thickness of the screen. The speed of the film relates to the exposure required to produce an optical density of one (on log scale) above the background density. It is defined as the reciprocal of the required exposure. Therefore for fast film the exposure time required is less than for slow film. The chief advantage of using slower film though, is that the latitude (useful exposure range) of the system can be increased. In addition, statistical unsharpness due to non uniformity in the neutron beam can be reduced using slow film.

In the case of neutron radiography with film, the reciprocity law fails to hold [46]. The reciprocity law states that to obtain a given density the product of the radiation intensity

I and the exposure time t must be a constant. This law is strictly obeyed only when the rate of ionization in the emulsion is high. This is always the case when ionizing radiation is composed of charged particles that produce sufficiently intense ionization in the silver halide grain through which they travel. This causes that grain to pass immediately through the unstable phase in latent image formation.

With scintillating screens, on the other hand, the light intensity at the emulsion following the absorption of a neutron is not necessarily high enough to take the latent image through its unstable phase sufficiently quickly. In addition, there is the possibility that the image will decay before another neutron is absorbed in the same area. Therefore, the law in this case is modified to $I t^p = \text{constant}$ [46, 48]. Here p is called the Schwarzschild parameter and has a typical value of 0.75.

Because of the failure of the reciprocity law in neutron radiography there are two types of characteristic curves which can be defined: the “time scale” curve and the “intensity scale” curve. To obtain the “time scale” curve, beam intensity is held constant and the exposure time is varied over a range of values and the final curve is plotted with density of film against exposure time. To obtain the “intensity scale” curve the time is held constant and the intensity is varied and the curve is plotted with density against intensity. Usually the “time scale” characteristic curve is used. But if the parameter p is known then the slopes of the two curves can be related.

2.2.2 Image Plate Detection

Image plates are well known in the field of x-ray imaging. But their use in neutron imaging is relatively new. Image Plates (IP's) have inherent advantages compared to other imaging detectors, such as [49]

- No accumulation of intrinsic dark signals during the exposure;
- No limitation in the count or dose rate;
- A high dynamic range in dose of more than 8 orders of magnitude;
- High efficiency;
- No principal limitation of the detection area.

The neutron sensitive IP's are made up of a thin phosphor layer consisting of a mixture of storage phosphor, neutron converter and organic binder that is coated on a polymer film [49].

The operational principle of the IP's can be divided into following two parts:

- Neutron exposure of the IP's.
- The optical readout of the IP's.

During exposure the neutrons are absorbed by the neutron converter and converted into ionizing secondary radiation. This process is controlled by the neutron absorption cross-section of the converter material used. Many materials can be used as neutron converters in IP's like ${}^6\text{Li}$, ${}^{10}\text{B}$, Gd, ${}^{235}\text{U}$ etc. Generally Gd compounds which are transparent and are available in fine powders such as Gd_2O_3 or just Gd is used. Lithium-6 is generally used in the form of ${}^6\text{LiF}$ powder. The average diameter of these powders of Gd_2O_3 and ${}^6\text{LiF}$ are $\sim 3.3\text{-}\mu\text{m}$ and $3.5\text{-}\mu\text{m}$ respectively [50]. Due to the high absorption cross-section of these materials, a layer thickness of $8.3\text{-}\mu\text{m}$ is sufficient to absorb 63% of the neutrons for Gd. The secondary radiation which is emitted by Gd is the conversion electrons of $\sim 70\text{ keV}$ and the γ -radiation of 0.3, 0.4, 1.2 MeV and other energies from different cascades of de-excitation of the excited Gd nuclei [50]. ${}^6\text{Li}$ produces α -particles of 2.05 MeV and tritium of 2.74 MeV [50]. This secondary radiation is absorbed in the storage phosphor and generates electron/hole pairs which are subsequently stored in electron and hole storage centers. The

storage is made up of BaFBr:Eu photo stimulable phosphor or some other complex like this. It has an average diameter of $\sim 5\text{-}\mu\text{m}$. To absorb the secondary radiation efficiently, the absorption coefficient of the storage phosphor is kept high. Also their thickness is kept more than $1/\mu$ which is the range of secondary radiation. But still γ -radiation is not absorbed by the layer as its range is more.

During the process of absorption by the phosphor electron-holes pairs are created. Subsequently the electrons are trapped in halide vacancies and the holes are stored in the complex close to the dopant ion. About 8 such sites are generated per keV of absorbed energy. This translates to about 640 such pairs per absorbed neutron in Gd converter screens [49].

After the radiographic image is transferred to an IP, it is scanned point-by-point by a laser beam in an image reader. A series of the photo stimulated luminescence (PSL) emissions corresponding to the scanned pixels is detected by a photomultiplier tube through a high efficiency light guide and converted into electric signals. During the readout process of IP's the laser beam is broadened by light scattering in the phosphor layer of the IP. This process can be attributed to the diffusion of photons [49]. For sufficiently small sizes of the laser focus, the resulting intensity distribution is a function of three parameters: the average length l until a photon is scattered uniformly, the light absorption per scattering length a , and the thickness of the phosphor layer d . In the case of low laser light absorption the spatial resolution of the scanned image is roughly half of the thickness of the phosphor layer.

The scattered laser light causes photo stimulation of the electron storage centers. During the photo-stimulation, the electron at the F-centers is excited from 1s ground state to the 2p excited state. Subsequently the surrounding lattice relaxes bringing the F-centers into

relaxed excited state (RES). From here the electron can either be transferred by thermally activated band transport or tunneling transport to the *hole* storage centers [51]. At the hole centers the electrons combine with the hole centers and the stored energy is released and is transferred to the dopant ion, which emits the energy in the form of a characteristic luminescence. To keep this separate from the stimulating laser light the corresponding emission band is kept at a different frequency. Besides the emission wavelength the value of decay time of the storage phosphor is also important as it limits the maximum possible readout time.

After the emission of the PSL at the specific location in the storage phosphor layer the photon has to travel to the surface of the IP and escape in order to get detected by a photo-detector. This can again be described by photon diffusion. After the escape of the photon from the surface of the IP it is collected by glass or mirror optics and is sent in the photocathode of photomultiplier tube. In good scanners, up to 70% of the light is collected and passed through optical filters. The filter removes nearly 20% of the collected photons. Hence the total collection efficiency is around 50 to 60%. At the photocathode the PSL is converted into photoelectrons. These photoelectrons are amplified by a factor of around 100. This creates a signal that is easily detectable by the data acquisition system which digitizes the signal and forms a digital image. The entire process from exposure to neutrons to image formation is shown in Fig. 2.3. The figure also shows the type of noise which enters into the image signal at different steps of the image formation process. Among the five noise components shown three are fixed noise sources and do not vary with the IP type and composition. The light photon quantum noise is negligible as the number of light quanta emitted per neutron absorbed is sufficiently larger than unity. Therefore the main component

of the quantum noise is the neutron absorption efficiency of the IP and the absorption of secondary ionization particle by the PSL phosphor [50]. Therefore Gd-IPs are better than ^6Li -IPs in the sense of keeping the quantum noise low. However, the amplification rate in the conversion and excitation process of the Gd-IPs is about 30 times lower. Therefore, the Li-IPs are expected to be more suited if the gamma content in the beam is high.

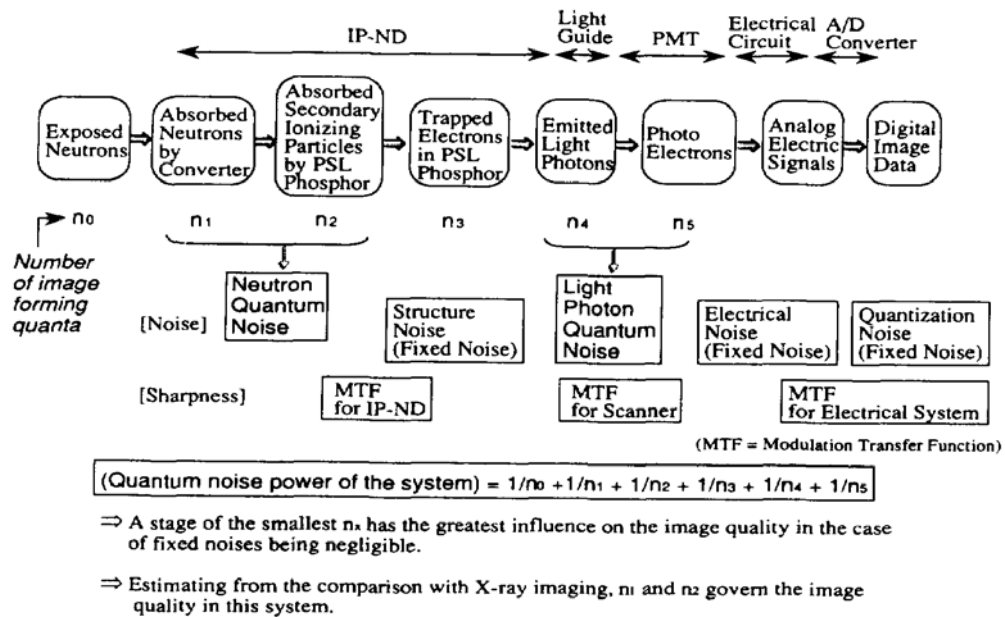


Fig. 2.3. The image plate detection process flow chart [50].

2.2.3 Scintillation Screens and CCD Detection

Scintillation screens are also used for the conversion of neutrons into a visible photon signal, which can be later detected by a charged coupled device (CCD) system. This approach is based on the neutron capture and phosphorescence phenomena. Phosphorescence is the luminescence produced by certain substances after absorbing radiant energy or other types of energy. In the scintillation screen the neutron is absorbed by a high cross-section neutron absorbing material. The product particles produced in the absorption

event interacts with the phosphor to produce the light signal, which is later detected by the CCD. The screen which is being used in the present case is ^6Li based. The phosphor is ZnS:Cu,Al,Au which emits green light to which a CCD is most sensitive.

The CCD chip is an array of Metal-Oxide-Semiconductor capacitors (MOS capacitors), each capacitor representing a pixel. By applying an external voltage to the top plates of the MOS structure, charges (electrons (e-) or holes (h+)) can be stored in the resulting potential well. These charges can be shifted from one pixel to another pixel by digital pulses applied to the top plates (gates). In this way the charges can be transferred row by row to a serial output register. The image is the display of the electron distribution. In the present case these electrons are optical generated by the light signal emitted by the scintillation screen, i.e., the electrons are transferred from the valence band to the conduction band by these photons. But some electrons can also get transferred due to thermal excitation. This constitutes the noise and is called dark current in the CCD. This can be minimized by reducing the temperature of the CCD. Also images that include dark current can be corrected by subtracting the dark frame image, which is the image taken with the shutter closed.

This type of neutron detection system is mainly used in real-time radiography. This is because the CCD read out time is less compared with image plates. Also erasing of the CCD is fast and external intervention is not required.

2.3 Image Degradation

In neutron radiography the major image degradation type is the *edge blurring* or *edge unsharpness*. Image degradation in general, and edge unsharpness in particular, is influenced by the following major factors:

- Recorder Unsharpness: the inherent unsharpness of the recorder used to get the

radiographic image. In the case of film, it depends on the size of the silver halide particles and in general is around 20- μm .

- Converter Unsharpness: the capture of a neutron in a converter leads to the isotropic emission of secondary radiation which may lead to the formation of a developable center in the recorder at some orthogonal distance from the incident neutron path. This also depends upon the thickness of the converter and the proximity of the recorder with the converter.
- Scattering degradation: neutrons scattered anywhere in the system lose their collimation and if they reach the detection system then it leads to reduction in the contrast and signal to noise ratio. Even the scattering in the sample results in image degradation and some image artifacts can also develop depending on what is the fraction of the scattered component.
- Geometric Unsharpness: an increase in beam divergence will tend to geometrically increase the unsharpness. Geometrical unsharpness of a system is often described by the L/D ratio, where L is the object aperture distance and D is the aperture diameter.
- Motion Unsharpness: object motion during an exposure contributes to image blurring. This can be the major source of blurring in real-time imaging if the frame rate of the camera is much less than the motion of the object.
- System Noise: Any other source of noise like the background in the system, the dark current in the CCD detection systems, blurring due to film development techniques in the case of film and the spread of the laser spot in the read out of image plates.

In general, the produced image of an object is a blurred version of the ideal image formed by the radiation that is emitted by the object. An object $f(x, y)$ is formed of the

points $f(x, y)dxdy$. If linearity and shift invariance of the imaging system is assumed, which is the case if the image has been taken in the linear portion of the characteristic curve, then the image of array of points $f(x, y)dxdy$ will be the sum (or integral) of the image of the various points. Here, linearity property of the imaging system refers to the fact that the image due to the weighted sum of inputs is equal to the same weighted sum of the corresponding individual images. The shift invariance property can be stated as if $g(x, y)$ is the image of $f(x, y)$ then $g(x - x_o, y - y_o)$ is the image of $f(x - x_o, y - y_o)$. If $h(x, y)$ represents the image of a unit point located at $(x=0, y=0)$ then the image $g(x, y)$ due to the array of point elements is given by [52]

$$g(x, y) = \int \int_{-\infty}^{\infty} f(\xi, \eta)h(x - \xi, y - \eta)d\xi d\eta \quad (2.12)$$

which can also be written as Eq. (2.13) by a simple change of variable.

$$g(x, y) = \int \int_{-\infty}^{\infty} f(x - \xi, y - \eta)h(\xi, \eta)d\xi d\eta \quad (2.13)$$

In imaging parlance, the function $h(x, y)$ normalized by the system gain is known as the point spread function (PSF). The PSF depicts the spread of a point which takes on the image plane due to various sources of unsharpness. Thus the final image obtained is the two dimensional convolution of the object function $f(x, y)$ and the PSF multiplied with the gain Λ associated with the imaging system.

$$g(x, y) = \Lambda \int \int_{-\infty}^{\infty} f(x - \xi, y - \eta)PSF(\xi, \eta)d\xi d\eta \quad (2.14)$$

where Λ and can be written as $\Lambda = \int \int_{-\infty}^{\infty} h(\xi, \eta)d\xi d\eta$ and $PSF(x, y) \equiv h(\xi, \eta) / \Lambda$.

A typical PSF is shown in Fig. 2.4. In the figure x and y are the variable co-ordinates and (u_o, v_o) is the point whose PSF is being considered. Along with the shift invariance property the PSF also generally has circular symmetry which makes PSF independent of the theta co-ordinate in polar form.

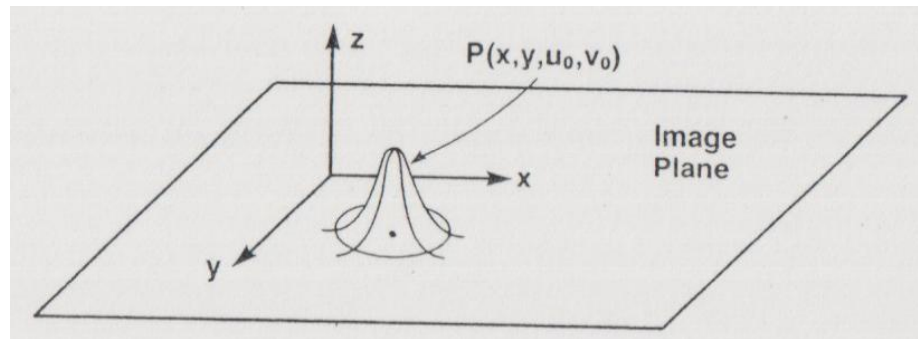


Fig. 2.4. A typical point spread function of a radiography system [45].

To obtain PSF a point source can be created by making a pin hole of a few microns in diameter in highly neutron absorbing materials like gadolinium and obtaining its radiograph on the image plane. This process is shown in Fig. 2.4. Since it is difficult to obtain an actual point neutron source, usually the PSF associated with an imaging system is calculated from a line spread function (LSF) which is a one dimensional description of an image plane response with variation in only one of the possible directions. To obtain the LSF from a radiograph an infinitesimally narrow line neutron source is required which can be created by making a slit of a few microns in width on a highly neutron absorbing material. Figure 2.5 depicts this process of obtaining a LSF. But again it is a difficult task to obtain a line source like that. Therefore LSF, which is like system response to a delta function input, is obtained by differentiating the edge spread function (ESF) which is the radiograph of an edge function and can be obtained easily from a real radiograph of an edge of a neutron absorbing sample.

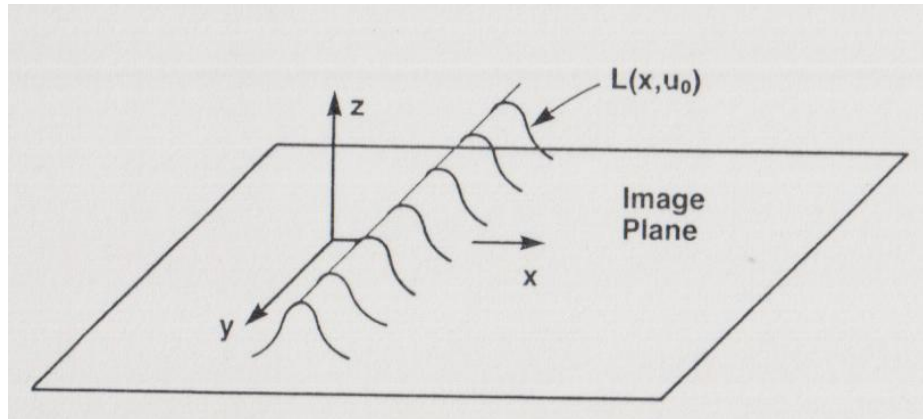


Fig. 2.5. The line spread function associated with a radiography system [45].

The PSF and the LSF are of fundamental importance in characterizing the resolution of the imaging system. The full-width at half maximum (FWHM) spread of the PSF or the LSF can be taken as the resolution of the radiograph. But there can be other definition of resolution which can be found in literature [53, 54]. There are four potential candidate functions which can be used as LSF.

- Rectangular ($y = t$ for $-c < x < c$)
- Gaussian ($y = c \exp(-ax^2)$)
- Lorentzian ($y = \frac{1}{1+cx^2}$)
- Exponential ($y = \exp(-c|x|)$)

Figure 2.6 shows graphically each of the LSF candidates.

The rectangular function makes too gross an approximation. From the figure it is clear that Gaussian LSF is too large near the origin and too narrow near the wings. The Lorentzian and exponential LSF forms provide a reasonable good fit depending upon the range of x taken. Numerical curve fit has shown that Lorentzian can provide better curve fit than exponential for the experimental data near zero while exponential performs better for large values of x [53]. Also for neutron radiography Lorentzian has been found better than

exponential LSF [55]. But it has also been shown that for the LSF obtained from neutron image plates a Gaussian is a better approximation than a Lorentzian [56].

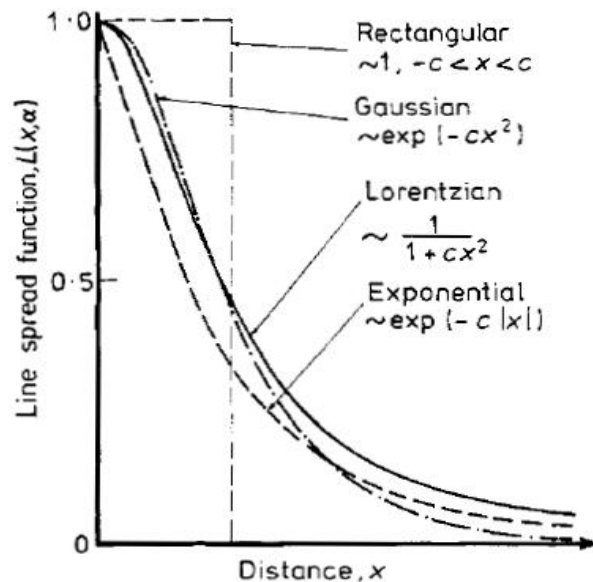


Fig. 2.6. Different forms of LSF which can be used in radiography [53].

The Modulation transfer function (MTF) is also often used along with PSF and LSF to describe the unsharpness in radiography [45, 55 and 57]. The MTF is the frequency domain description of the radiographic process. It is defined as the modulus of the optical transfer function (OTF) [45]. The OTF is equivalent to the two-dimensional Fourier transform of the systems $PSF(x, y, u_o, v_o)$ [52].

2.4 Real-time Neutron Radiography

Real-time radiography is an imaging technique that uses penetrating radiation to produce images which are viewed concurrent with the irradiation [58]. In the case of dynamic systems, real-time imaging allows image interpretation to be performed simultaneously with the progress of the event. In this case the conversion of neutrons to light is done by the phosphor which can then form an image on a CCD. The CCD is read in real-

time by an attached computer. In real-time imaging spatial resolution is usually compromised at the gain of increase in time resolution. Light Intensifier X-ray Image (LIXI) can also be used to obtain real-time neutron images. In such devices, neutron scintillations are amplified by a light intensifier and a video camera captures the resulting light and thus an analog image is obtained [59]. Other basic principles of radiography remain the same as discussed above.

2.5 Neutron Tomography

In tomography the third dimension of the object is reconstructed by taking radiographs of the sample at different angles by rotating the sample relative to the source. A computed tomography (CT) image is a result of the superposition of all planes normal to the direction of propagation of the beam [60]. The data collected from the different radiographs are called the projection data of the sample. Projection data can be mainly classified into two types depending upon the geometry of the beam being used:

- Parallel beam projection data.
- Fan beam projection data.

The beam geometry for the parallel beam and fan beam data is shown in Fig. 2.7. In our case, the beam geometry can be assumed to be parallel and therefore this will be discussed in brief below.

In the parallel beam geometry the projection data $p(r, \theta)$ can be shown to be the Radon transform of the two dimensional neutron attenuation coefficient $f(x, y)$ of the sample.

$$p(r, \theta) = \mathfrak{R}(f(x, y)) \quad (2.15)$$

where

$$\begin{aligned}x &= r \cos \theta - s \sin \theta \\y &= r \sin \theta + s \cos \theta\end{aligned}\tag{2.16}$$

Here r - s is the rotated co-ordinate system in counterclockwise direction by angle θ .

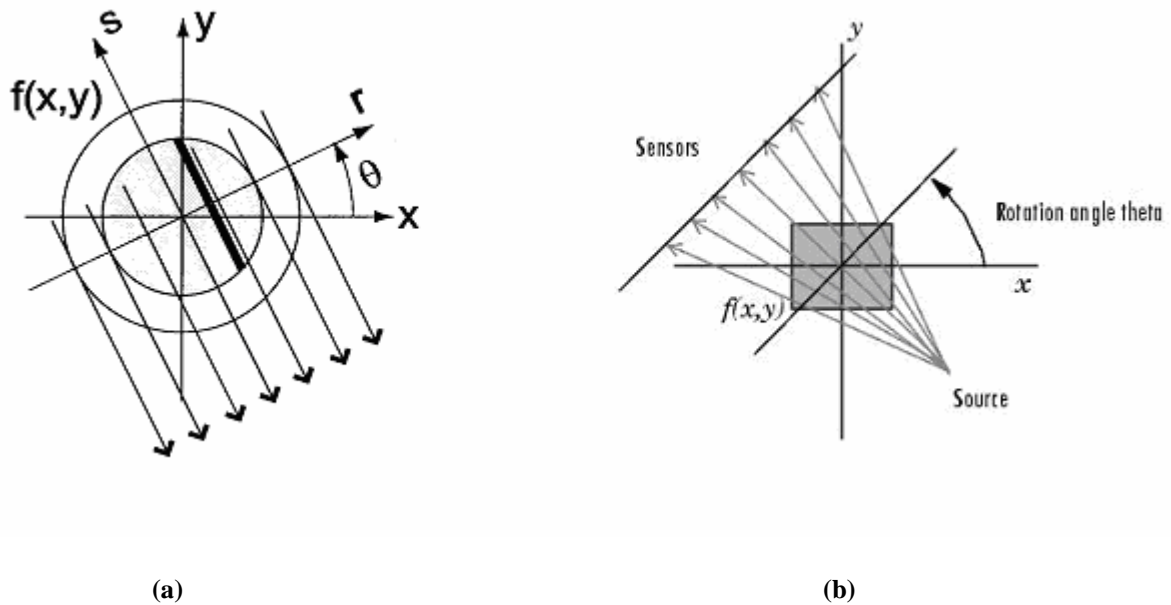


Fig. 2.7. Projection data collection geometry in Computed Tomography (a) Parallel Beam Geometry [60] (b) Cone Beam Geometry [61]

The family of projections $p(r, \theta)$ for an object function is called the sinogram. The reconstruction of the sinogram necessitates the calculation of inverse radon transform of the projection data $p(r, \theta)$. For the reconstruction of the projection data there are many different algorithms with each having its advantage and drawbacks. The commonly used algorithms for reconstruction are:

- Transformation based techniques like Fourier techniques, Convolution Back Projection (CBP), Filtered Back Projection (FBP), Wavelet based reconstruction techniques etc.
- Iterative Techniques like algebraic reconstruction technique (ART) and Modified ART (MART).
- Statistical reconstruction technique like Maximum Likelihood and Expectation

Maximization Techniques.

- Unconventional and mixed techniques like genetic algorithms, CBP and ART combined reconstruction etc.

The FBP technique is one of the commonly used reconstruction technique that has been implemented in this work and is discussed here. In the back projection technique the measurements obtained along each projection is projected back along the same angle. In this case, each back-projection is identical to the other. Mathematically, the back projection along an unknown density line is given by

$$b_{\theta}(x, y) = \int p_{\theta}(r) \delta(x \cos \theta + y \sin \theta - r) dr \quad (2.17)$$

Where $b_{\theta}(x, y)$ is the back-projected density due to the projection $p_{\theta}(r)$. The $\delta(\dots)$ function is Dirac delta function having a value of one at $r = 0$. The back-projection distributes the density on the line.

Adding back-projections over all the angles we get what is called a laminogram.

$$f_b(x, y) = \int_0^{\pi} b_{\theta}(x, y) d\theta = \int_0^{\pi} \int_{-\infty}^{+\infty} p_{\theta}(r) \delta(x \cos \theta + y \sin \theta - r) dr d\theta \quad (2.18)$$

This laminogram represents the distorted picture of the sample which needs to be corrected. Each projection of the δ function is also a δ function at the origin. If these functions are back-projected the resulting response (known as the *impulse response*) is given by

$$h_b(r) = \int_0^{\pi} \int_{-\infty}^{\pi} \delta(r) \delta(r \cos(\theta - \phi) - r) dr d\theta = \frac{1}{r} \quad (2.19)$$

Knowing the response to the impulse and assuming that linear systems theory applies, the following relationship holds

$$f_b(x, y) = f(x, y) * \frac{1}{r} \quad (2.20)$$

where the * denotes the convolution operation. Practically this means that the actual image is blurred by the $\frac{1}{r}$ term. The 2D Fourier transform of equation is given by

$$F_b(k, \theta) = F(k, \theta) \frac{1}{k} \quad (2.21)$$

where k is the Fourier frequency. The $\frac{1}{r}$ blurring can be removed by the filtered back-projection. In this case Central Slice Theorem (CST) which is fundamental to computed tomography is used. Let $F(k_x, k_y)$ be the 2D Fourier transform of the function $f(x, y)$ i.e.

$$F(k_x, k_y) = \int_{-\infty}^{\infty} \int_{-\infty}^{\infty} f(x, y) \exp\{-2\pi j(k_x x + k_y y)\} dx dy, \quad (2.22)$$

where k_x and k_y are the orthogonal Fourier frequencies with units of radians per distance.

Also let $P_\theta(k)$ be the 1D Fourier transform of the projection $p_\theta(r)$ i.e.

$$P_\theta(k) = \int_{-\infty}^{\infty} p_\theta(r) \exp(-2\pi jkr) dr. \quad (2.23)$$

Allowing θ to vary from 0 to π radians and stacking them to get $P(k, \theta)$. Then CST states

that

$$P(k, \theta) = F(k_x, k_y) \quad (2.24)$$

$$k_x = k \cos \theta$$

$$\text{where } k_y = k \sin \theta \quad (2.25)$$

$$k = \sqrt{k_x^2 + k_y^2}$$

which in short can be stated as *the set of 1D Fourier transform in r of the Radon transform of a function is equal to the 2D Fourier transform of that function.*

Using CST Eq. (2.18) can be written as

$$f_b(x, y) = \int_0^\pi b_\theta(x, y) d\theta = \int_0^\pi \int_{-\infty}^{+\infty} \int_{-\infty}^{\infty} F(k, \theta) \exp(2\pi jkr) dk \left[\delta(x \cos \theta + y \sin \theta - r) dr d\theta \right] \quad (2.26)$$

Integrating over r , Eq. (2.26) reduces to

$$f_b(x, y) = \int_0^{\pi+\infty} \int_{-\infty}^{\infty} F(k, \theta) \exp\{2\pi j k(x \cos \theta + y \sin \theta)\} dk d\theta. \quad (2.27)$$

Comparing Eq. (2.27) with the exact inverse 2D Fourier transform of the 1D Fourier transform of the projection data which is

$$f(x, y) = \int_0^{2\pi+\infty} \int_0^{\infty} F(k, \theta) \exp\{2\pi j k(x \cos \theta + y \sin \theta)\} k dk d\theta = \int_0^{\pi+\infty} \int_{-\infty}^{\infty} F(k, \theta) \exp\{2\pi j k(x \cos \theta + y \sin \theta)\} |k| dk d\theta \quad (2.28)$$

a difference of a factor of k is observed which was expected. Substituting the $F(k, \theta)$ with 1D Fourier transform $\mathfrak{F}\{p_\theta(r)\}$ and weighting it with $|k|$ along each radial line to remove the blurring in the back-projection as well as multiplying and dividing by $|k|$ we obtain

$$f(x, y) = \int_0^{\pi+\infty} \int_{-\infty}^{\infty} \frac{\mathfrak{F}\{p_\theta(r)\} \bullet |k|}{|k|} \exp\{2\pi j k(x \cos \theta + y \sin \theta)\} |k| dk d\theta. \quad (2.29)$$

Equation (2.29) is the FBP reconstruction technique. The equation involves only 1D Fourier transform which is calculated using Fast Fourier Transform (FFT) techniques. Hence the reconstruction can be obtained fast. The FBP algorithm can be written as:

- Each projection is individually transformed.
- The transformed projection is weighted with $|k|$.
- The result is inverse transformed.
- The result is back projected.

The implementation of the FBP on computer requires a discrete version of it. The $|k|$ terms act as a ramp filter which is not stable. Therefore it is modified in order to remove the instabilities using various different kinds of filters that have different advantages and drawbacks. There are standard computer routines available for image reconstruction using FBP [61].

Chapter 3

Design of the Neutron Imaging System

3.1 PULSTAR Reactor

The PULSTAR Reactor is the fourth reactor to be operated on the campus of N.C. State University. This reactor became fully operational in 1972. It has a full power output of 1-MWth. It is operated in an open pool of pure water that provides access for observation and maintenance. Water acts as both coolant and the moderator. The water temperature is about 105°F. An aluminum tank acts as the pool liner, which is surrounded by concrete shielding [62]. The core having a size of 24"x15"x13", is loaded with 359-kg of Uranium Dioxide pin-type fuel with 4% enrichment. Uranium dioxide fuel pellets are enclosed in zircaloy cladding. This fuel gives the PULSTAR Reactor response characteristics that are very similar to commercial light water power reactors. There are 6 Beam Tubes (BT's) positioned around the core. The layout of the beam tubes in the reactor is shown in Fig. 3.1.

The imaging facility has been setup on BT5 of the reactor. As it is clear from Fig. 3.1 BT5 is the radial beam tube with a direct line of sight at the core. The beam tube is circular with two steps. The diameter at the entry of the beam tube (reactor side) is 6-inches which increases to 9-inches at the first step and to 12-inches at the second step which comes out of the biological shield of the reactor. The steps in the beam tube can be observed in Fig. 3.1. The measured total neutron flux at the beam port entry is $\sim 2.5 \times 10^{12}$ n/cm².sec at full power. The measurement of the neutron flux was performed using cobalt foil activation. The Cd ratio was measured to be ~ 90 . The gamma flux is also high in the beam tube due to its direct observation of the core. MCNP simulation of the reactor core was done to obtain the neutron

and gamma energy spectrum at the entry of the beam tube. The MCNP core model is shown in Fig. 3.2. The energy spectrum of neutrons and gammas at the entry of beam tube is shown in Fig. 3.3 and 3.4 respectively. The Y-axis in the figures gives the probability density function of the particle flux with respect to energy normalized to a maximum of unity. From the neutron spectrum it can be clearly observed that the neutron beam is sufficiently thermalised and further moderation is not required. However, fast neutrons are also present and should be removed to approach a pure thermal beam. The gamma spectrum shows a sharp peak at 2.2 MeV which are prompt gammas emitted by the absorption of neutrons by hydrogen in water. The total gamma flux at the beam port entry is estimated to be $\sim 5 \times 10^{14}$ $\gamma/\text{cm}^2 \cdot \text{sec}$ at full power.

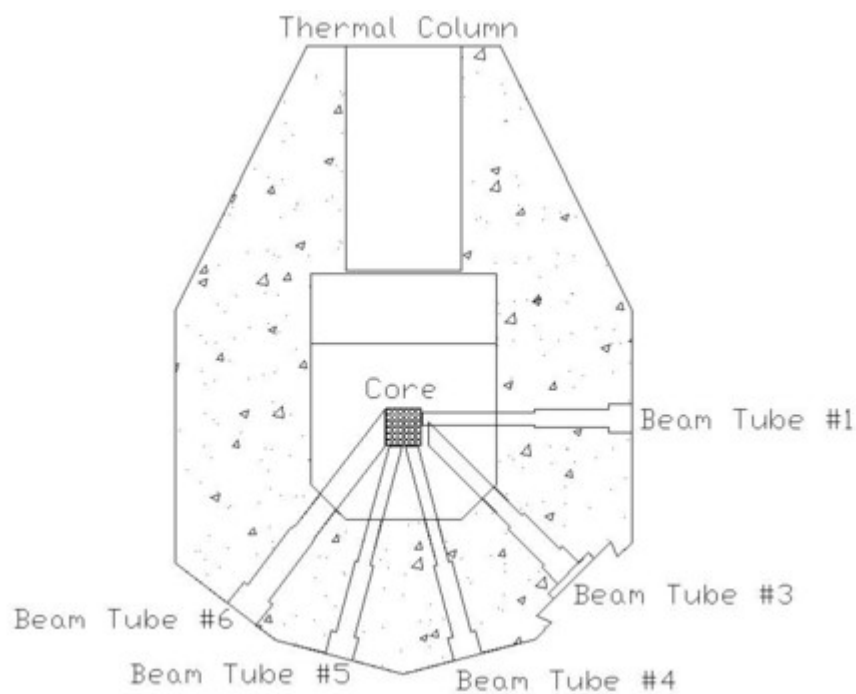


Fig. 3.1. A schematics of the PULSTAR reactor showing various beam tubes¹. Beam tube #2 which is through tube is not shown in this figure.

¹ Courtesy of Mr. Andrew T. Cook, North Carolina State University, Nuclear Reactor Program.

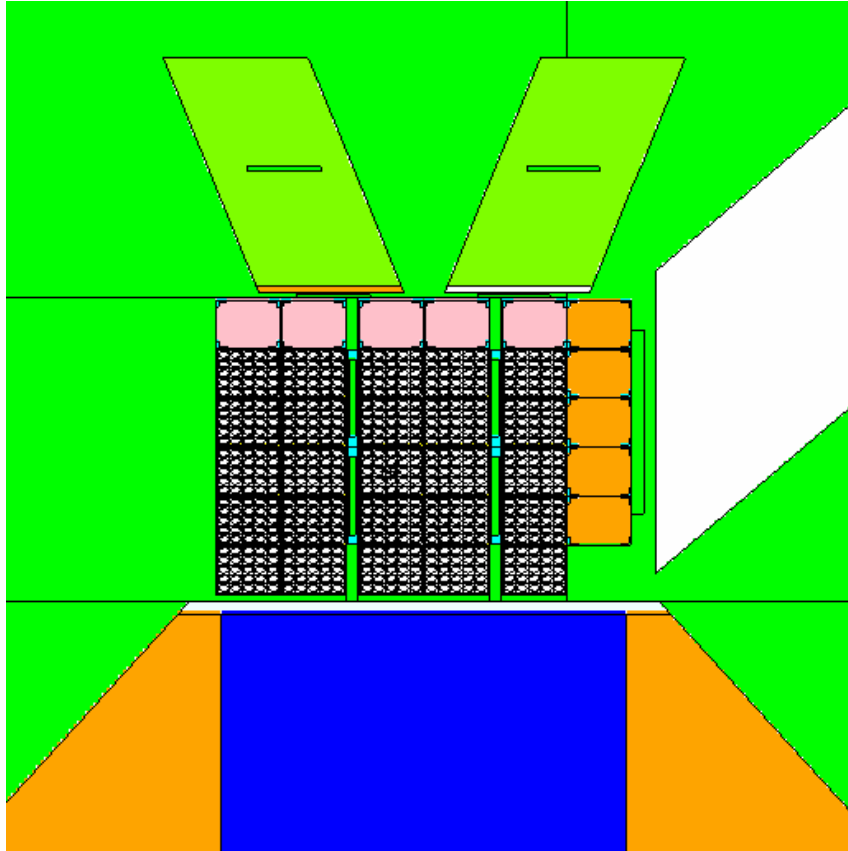


Fig. 3.2. The MCNP model of PULSTAR reactor core showing beam tubes 4, 5 and 6.²

Given the type and characteristics of the neutron source the main components that should be considered during the design of a neutron imaging facility are:

- The beam collimator
- The beam shutter
- The shielding and beam stop
- The radiographic and tomographic sample positioning system
- The screen (film or digital detectors) and screen positioning system
- The screen development or read out system

² This model was started by Dr. Jianwei Chen while at the Nuclear Reactor Program at North Carolina State University and enhanced during his work.

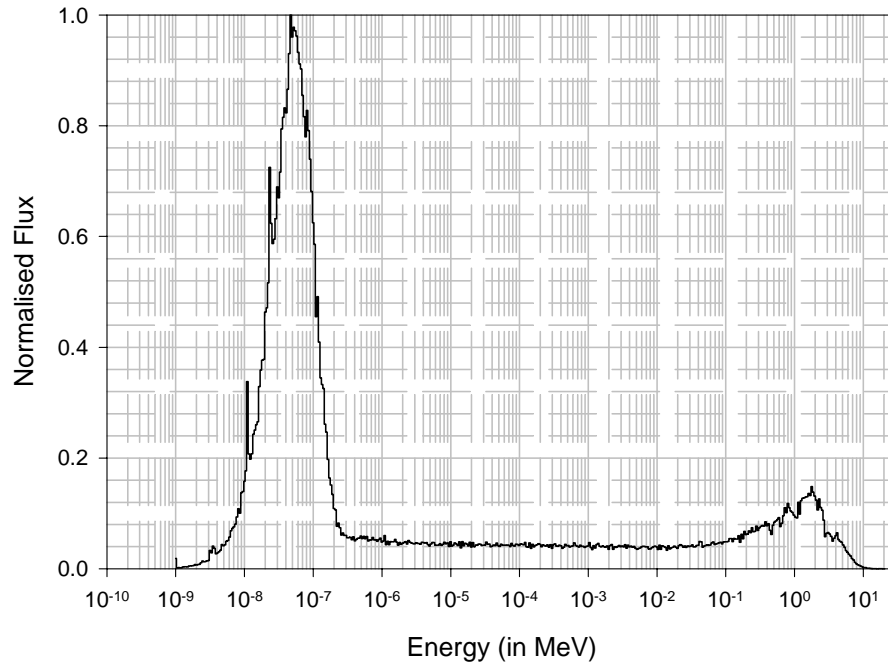


Fig. 3.3. The neutron energy spectrum at the entry of BT #5 as calculated using MCNP.

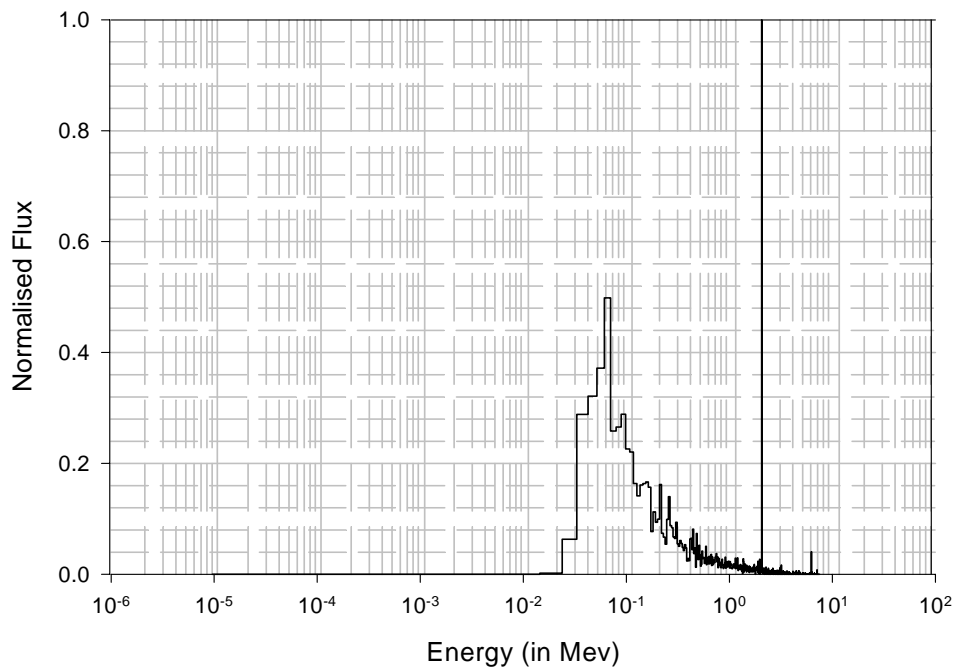


Fig. 3.4. Gamma energy spectrum at the entry of BT #5 as calculated using MCNP.

Three main types of collimators have been used for neutron imaging [3]:

- The simple straight parallel collimator [10, 63]
- Soller Slit approach to cover a reasonably large radiographic area yet maintain parallel neutron paths [64, 65]
- Divergent beam collimator [66, 67]

In the early years of the application of neutron radiography the idea prevailed that parallel beams of neutrons are needed to obtain a good image. But in 1967 Barton concluded that a divergent-beam collimator produces the highest resolution [67]. Therefore in this work we decided to install a divergent beam collimator. In fact, the collimator is initiated with a short convergent section which defines the aperture more properly. Hence the collimator can be classified as convergent-divergent in shape, which is expected to give the best definition of the aperture.

After deciding the collimator shape, the basic components of the collimator were considered. In general this included the following components:

- Beam scattering element- To scatter the neutrons in the beam tube so that the inlet neutron flux at the entry of the beam tube can be increased and hence the total thermal flux at the imaging plane.
- Beam moderating element- In the case of thermal neutron radiography, the inlet neutron energy spectrum should have a peak around 0.1eV. If the spectrum is harder than that, then neutron moderators such as water or graphite are recommended to use [38].
- Beam Filters and their cooling- Even after moderating the beam, the remaining fast neutron flux should be filtered out by using fast neutron filters. Furthermore, the gamma-ray flux is reduced using gamma filters to obtain a favorable N/G ratio (cf.,

section 1.3.1.5 of chapter 1). Using a pure thermal beam enhances the quality of the produced radiographs. In addition, in tomography applications, it is crucial to have the least amount of noise possible in the radiographs from which tomograms are created.

- Aperture- The aperture is the window which is provided for the collimated neutron beam to reach the object. The size and shape of the aperture defines the flux and beam size at the image plane. Along with that, geometric unsharpness in the radiograph also depends on the aperture (D), which defines the L/D ratio of the beam, where L defines the distance from the aperture to the image plane. Proper definition of the aperture in the collimator should be established so that the neutrons do not leak from the surface outside the window. Otherwise, depending upon leakage, the geometric unsharpness will be more than that predicted from the L/D ratio.
- Gamma shielding- Gamma shielding is provided to reduce the gamma flux leakage from outside the beam defining volume.
- Collimator casing- Collimator casing is the outside casing in which collimating pieces are assembled. It is advantageous to have a modular design of the collimator in which some components can be changed if required without the need of replacing the entire collimator or its major components. This type of design provides greater flexibility during the course of the facility's operation life in terms of both time requirement for change and the cost of change of the component.
- Collimator lining- The collimator lining is made up of neutron absorbing material. A possible list of materials which can be used for this is given in section 1.3.1.2 of chapter 1. This lining is also crucial to decrease the scattering and hence getting a properly collimated beam.

- Fill Gas- The neutron flux is decreased by about 5% per meter of air thickness [38]. Hence if the flux is under consideration then the loss due to air can be reduced to less than 1% by replacing air with helium or in some cases argon as mentioned in section 1.3.1.3 of chapter 1.

In this work no beam scatterer was considered necessary. In addition, the presence of the beryllium reflector and the water moderator between the core and the beam tube entry gives sufficiently moderated beam as is clear from the energy spectrum shown in Fig. 3.3. Hence, beam moderating elements were also not required as their presence would significantly decrease the total flux without any further moderation. Consistent with the design objectives the material selection for the other collimator components was done. The choice of the collimator materials were chosen to be as light, inexpensive and easy to machine as possible. This resulted in the following choices:

- Aluminum - for collimator casing as it is light weight and is fairly cheap and has reasonable strength and very good machinability. Also it has fairly low neutron scattering and absorption cross-section.
- Boral – for aperture definition and collimator lining as it has boron which has very high thermal neutron absorption cross-section and does not get severely activated. Boral is difficult to machine but is easy to cut using a water jet cutting process or similar techniques. Also it was in stock and hence the material cost was saved.
- Lead and bismuth – for the gamma shielding outside the beam defining volume. Lead was already available with us and is a better gamma shield than bismuth. Also lead can be machined without much difficulty. Therefore lead was selected for gamma shielding.
- Borated polyethylene (5% boron) and boron nitride – for neutron shielding in the

outside beam defining volume as both of them have good machinability and fairly high absorption cross-section to provide a good shielding from the neutrons which escape from getting absorbed in the collimator lining.

- RX-277 – as filling material in the collimator. It is a heat resistant shielding material with about 1.6% of boron content by weight. The other active element present in this is hydrogen [68]. The density of the material is 1.68gm/cm^3 . This is specifically suited for neutron attenuation in power reactors. It is available in dry mix that can be cast in place.
- Beam filters – for filtering out the fast neutrons and photons from the collimated beam. Single crystal sapphire and single crystal bismuth were chosen to be used for the purpose. As discussed in chapter 1 sapphire is a better fast neutron filter than silicon and quartz. Also the transmission properties of sapphire are not altered by irradiation even after years within a beam tube of a reactor [69]. Along with that, cooling of sapphire to liquid nitrogen temperature is not required as with other filters since neutron attenuation is reduced by only about 30% by cooling it to 80K [69]. This attenuation would translate into just about 18% increase in the transmission from sapphire on cooling from 300K to 80K in comparison to 125% increase for beryllium where cooling is highly desirable [43]. This makes sapphire the best option to choose. In addition, bismuth is a photon filter along with having a thermal window for neutrons. That is why it was chosen for photon filtering.

3.2 MCNP Simulation of the Collimator

3.2.1 MCNP Code

MCNP is a general purpose Monte Carlo N-particle code which can be used for neutron, photon, and electron or coupled neutron/photon/electron transport, including the capabilities of calculating eigenvalues for critical systems. The code treats an arbitrary three dimensional configuration of materials in geometric cells bounded by first and second degree surfaces and fourth degree elliptical tori [70].

Pointwise cross-section data are used in MCNP calculations. For neutrons, all reactions given in a particular cross-section evaluation (such as ENDF/B-VI) are accounted for. Thermal neutrons are described by both the free gas and $S(\alpha,\beta)$ models. For photons, the code accounts for incoherent and coherent scattering, the possibility of fluorescent emission after photoelectric absorption, absorption in pair production with local emission of annihilation radiation, and bremsstrahlung. A continuous-slowing-down model is used for electron transport that includes positrons, k x-rays, and bremsstrahlung, but does not include external or self-induced fields.

The model is submitted in the form of a text input file to MCNP. The input file contains the geometry information, source information, material information and the type of output required in terms of standard tallies already provided in MCNP.

3.2.2 Collimator Model

After selecting the materials which have to be used in the collimator, the next task was to decide the filter length, the aperture size, the aperture defining boral plate thickness, and the divergence angle of the beam. The design objective was to have a thermal neutron

flux of $>1 \times 10^6$ n/cm².sec at full reactor power with the maximum thermal neutron content (TNC), the least photon content (i.e. maximum neutron to gamma (N/G) ratio), and a maximum L/D of at least 150 (as defined in ASTM Standards E748 and E1316 Section H [22]). Based on a study of other existing facilities, the selected design parameters were observed to be adequate to obtain the desired contrast and resolution in a given exposure time. To establish these parameters, the collimator was simulated using MCNP5. The MCNP simulation was performed in two steps: first the full MCNP model including the reactor core was run to establish the neutron and gamma-ray energy spectra at the core-side entrance of BT5. Second, the model of the collimator was executed starting at the entrance of BT5 and up to the image plane. In the second step the neutron and gamma-ray energy spectra that were used are those shown in Fig. 3.3 and 3.4. In this case, the spatial distribution of the source was taken to be uniform over the cross-section of the beam tube, which is a good assumption to make considering the geometry of the beam tube and the fact that its diameter is small (6-inches) compared to the core size. The initial direction was assumed to have a cosine distribution. The angle of interest which was important to the result was the maximum angle that is subtended by the beam tube exit at its entrance, which is 6° . Therefore the cosine distribution from 0 to 6° only was taken to improve statistics as well as reduce the runtime without affecting the result.

The location of the aperture in the beam tube was decided by the simple similar triangle analysis as shown in Fig. 3.5 [71].

From the figure it is clear that

$$\frac{d_1}{d_2} = \frac{L_1}{L_2 - L_1}. \quad (3.1)$$

With $d_1 = 15.24\text{-cm}$ (6-inches) and the beam size at 6-m (L_2-L_1) chosen to be 19-inches ($d_2 = 48.3\text{-cm}$) to accommodate large size film, the aperture location can be obtained to be $L_1 = 189\text{-cm}$. Also, based on the above analysis the divergence angle of the collimator is chosen to be $\sim 2^\circ$.

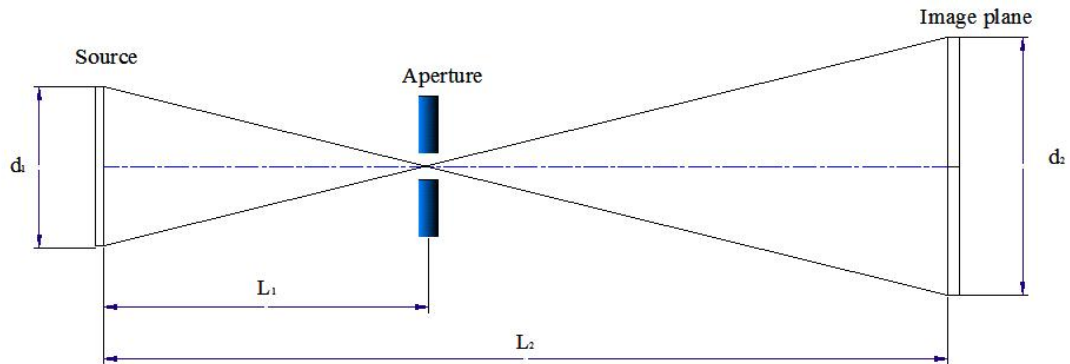


Fig. 3.5. Schematics of aperture location calculation.

The collimator has a modular design with three sections:

- The initial converging cone section
- The filter section
- The diverging section

The converging section helps to properly define the aperture by removing the neutrons not converging to the aperture. Lead and bismuth were both tested for use as gamma shielding in the converging section. But no significant difference was observed. Therefore, lead was selected for use in the convergent section due to prior availability of high purity lead. For the neutron shielding boron nitride (BN) and borated polyethylene (5% boron) both were tested using MCNP. Again no differences in collimator characteristic parameters were observed at the image plane, hence considering their price borated

polyethylene was selected. The converging section angle was kept greater than the angle subtended by the beam tube entry face at the filter section entry so that the collimator faces full area of the beam tube from the flux point of view.

The maximum distance which is available between the aperture and the image plane is 6-m. Therefore to attain the L/D of 150 at this distance the maximum aperture size which can be used is 4-cm. The aperture shape was kept square to match the rectangular shape of the film and image plates and at the same time to keep the horizontal and vertical geometric unsharpness arising due to the L/D effect the same.

After deciding the aperture size and shape, the filter requirement and their length had to be decided. A preliminary run of the model was performed without using any filters to check if neutron and gamma filtering is required or not. The energy spectrum of the neutrons at the 6-m image plane, obtained without using the filter is shown in Fig. 3.8 (b). The tally used the same energy bins as the source (Fig. 3.3) to have one to one correspondence with the inlet neutron spectrum. From the spectrum it can be observed that thermal neutrons were more absorbed inside the collimator than fast neutrons and the emerging neutron beam is somewhat harder.

To optimize the thermal neutron content of the beam, sapphire is used as a fast neutron filter. Sapphire single crystal filters are available in circular shape and at different sizes. To use the whole filter cross-sectional area it was decided to make the converging section circular in cross-section. Also as stated above the maximum size of aperture which can be used is 4-cm. This translates into a filter diameter of ~ 6 -cm. Hence the sapphire filter diameter was specified to be 2.5-inches keeping some margin. For the same reasons, the bismuth filter was also taken to be of the same diameter.

Another MCNP run was performed using a tentative length of the filter to verify the filtering effect on the emerging neutron beam. The spectrum of the emerging neutron beam is shown in Fig. 3.8 (c). Contrary to what was expected there was no filtering effect observed and instead the thermal neutrons were more attenuated and the energy spectrum became much harder. Also the predicted neutron flux was reduced to 5.6×10^3 n/cm².sec using 4-inches of bismuth and 6-inches of sapphire, which is much less than the design goal of 10^6 n/cm².sec. This is due to the fact that the free-atom neutron cross-sections for sapphire are used in MCNP. To assure more accurate simulations in MCNP, an estimation of the bound sapphire cross sections was made using ab-initio atomistic and crystal dynamics simulations. The efficiency of the filter is dependent on the magnitude of various components of the cross-section [40]:

- The absorption cross-section σ_{abs} , which is usually linearly dependent on the neutron wavelength and always independent of temperature.
- The coherent Bragg-scattering cross-section σ_{el} , which is dependent on the neutron wavelength, temperature and crystal orientation and perfection.
- The incoherent elastic cross-section σ_{inc} , which is usually small and independent of wavelength.
- The inelastic or phonon-scattering cross-section σ_{inel} , which also varies with neutron wavelength and is dependent on the crystal temperature (the value of σ_{inel} can be reduced significantly by cooling to low temperatures).

It has been shown by Mildner *et.al* [40] that elastic Bragg peaks are drastically reduced for high quality sapphire crystal. Therefore only the inelastic scattering cross-section was generated using NJOY for modeling purposes of sapphire in MCNP. The

generated cross-section of sapphire using both a Debye and ab initio generated (from the VASP/PHONON code [72]) phonon frequency spectra are shown in Fig. 3.6. Figure 3.6 also shows the cross-section of sapphire as calculated by Freund [52] as well as Cassels function [40, 73] which are given by

$$\text{Freund's Formula: } \Sigma = A\lambda + C \left(1 - \exp \left\{ - \left[\left(\frac{B}{\lambda^2} \right) + \left(\frac{D}{\lambda^4} \right) \right] \right\} \right). \quad (3.2)$$

$$\text{Cassel's Function: } \Sigma = A\lambda + C \left(1 - \frac{\lambda^2}{2B} \left(1 - \exp \left\{ - \left[\left(\frac{2B}{\lambda^2} \right) + \left(\frac{D}{\lambda^4} \right) \right] \right\} \right) \right). \quad (3.3)$$

Hemex, Hemlux and Hemlite are the different grades of sapphire supplied by Crystal Systems Inc. The fitting parameters for both functions for the different grades of sapphire were obtained from Ref. 40. The experimental data shown in the figure was also taken from Ref. 40. As it can be seen, the cross-section generated in this work is very close to what is given by Cassels function. Fig. 3.6 also shows the free atom cross-sections used by MCNP, which are clearly different from the bound ones.

The cross-section library was also developed for the bismuth crystal using the Debye model taking θ_D (the debye temperature) to be 119K [74]. The generated inelastic scattering cross-section of bismuth is shown in Fig. 3.7. The figure also shows the free atom cross-sections used by MCNP and the experimental data presented by Freund [42, 75] for both poly-crystal and mono-crystal bismuth at 300K. The cross-section calculations done by Adib *et.al.* [42] are also presented. The difference observed between our cross-section and Adib calculation is probably due to the difference in Debye temperature θ_D which is 300K in Adib's model. From the figure it can be observed that there is a sharp Bragg's peak at $\sim 2 \times 10^{-3}$ eV below which poly-crystal bismuth has a total cross-section very close to the generated inelastic cross-section. Above that energy, the cross-section becomes equal to the free atom cross-section. However, in the case of a mono-crystal the Bragg component is not

present. In our case the bismuth filter being used is made of large pieces of mono-crystals and therefore mono-crystal bismuth was assumed and the generated Debye model cross-sections were used in the MCNP simulations of collimator performance. The change in the neutron energy spectrum using the generated filter cross-sections can be observed in Fig. 3.8 (d) and can be compared to the normalized spectra calculated at different locations and using various filter cross section libraries.

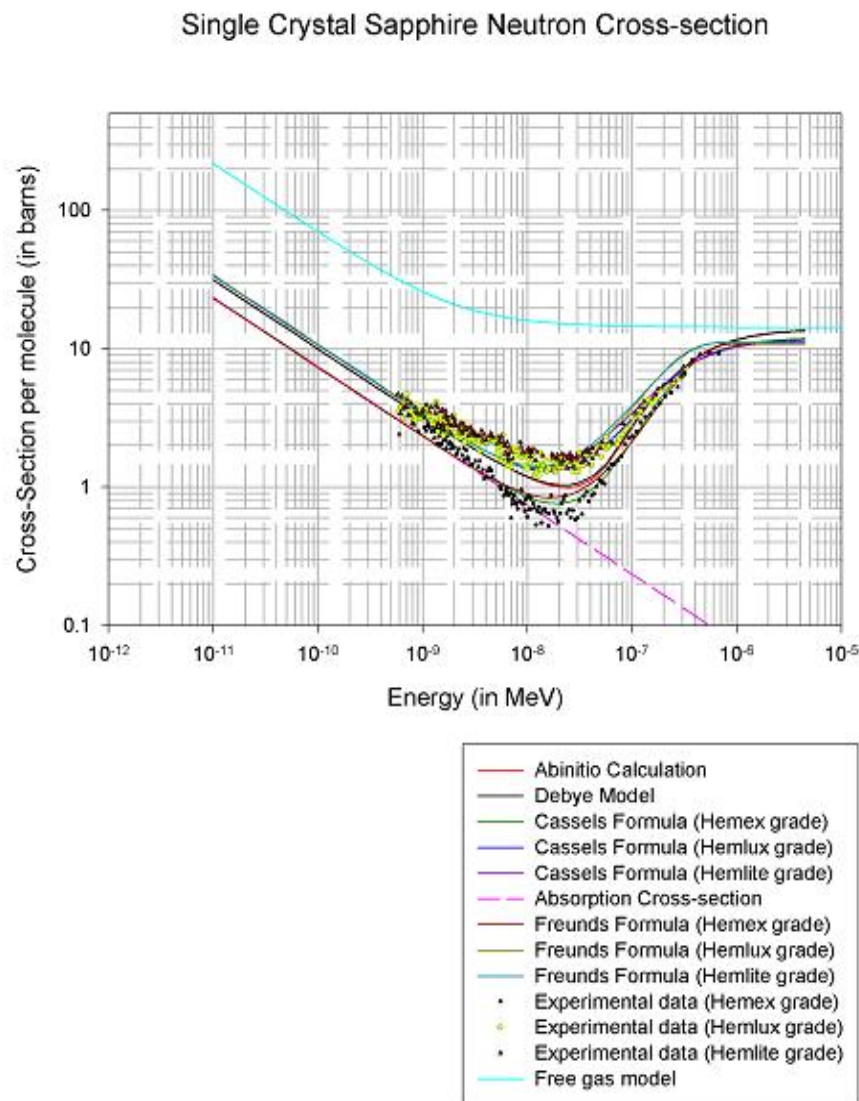


Fig. 3.6. Sapphire cross-section generated to be used in MCNP. Comparison to the published theoretical and experimental data is shown in the figure.

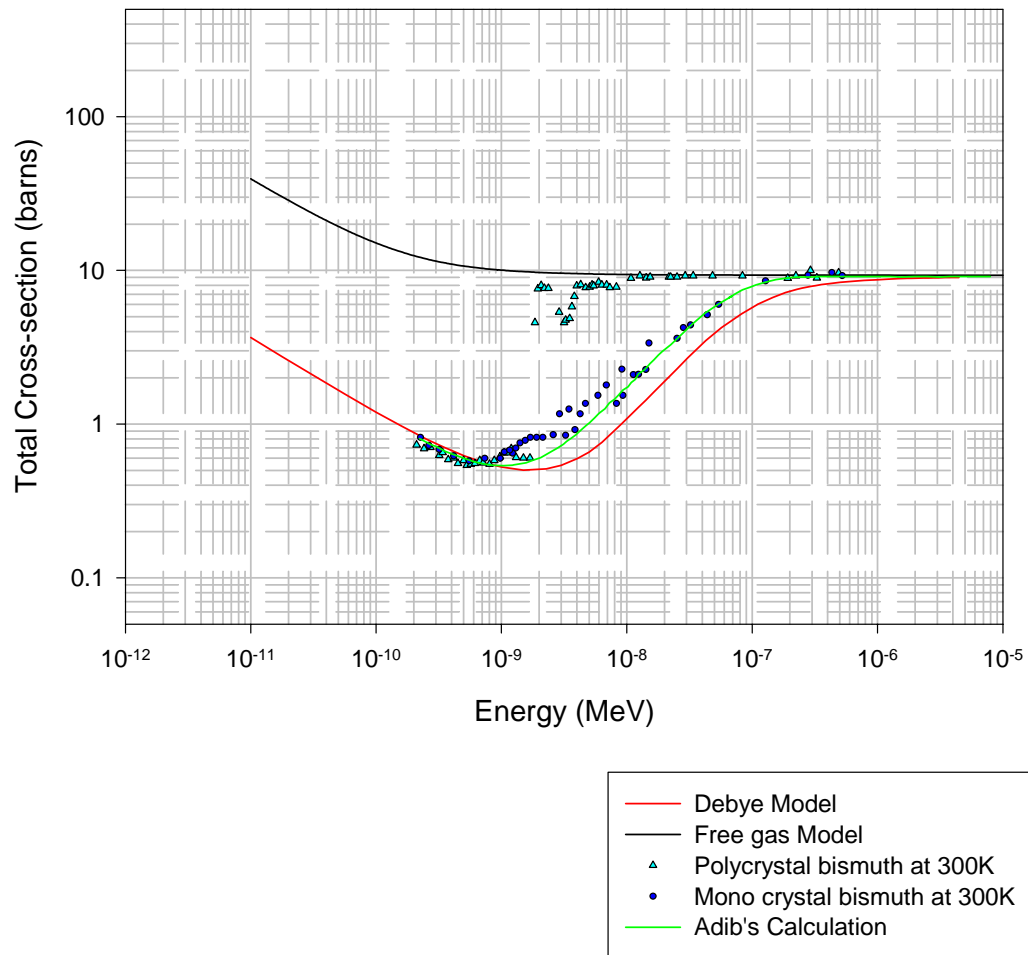
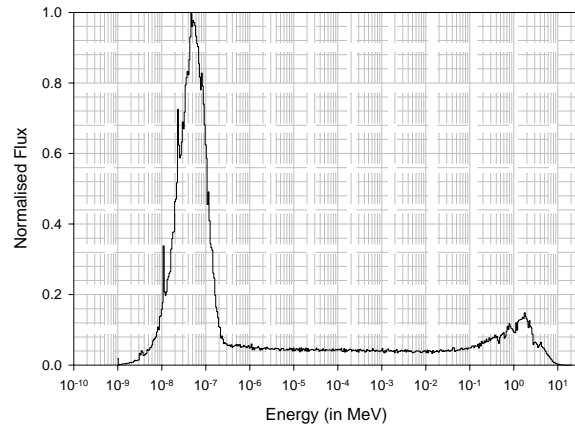
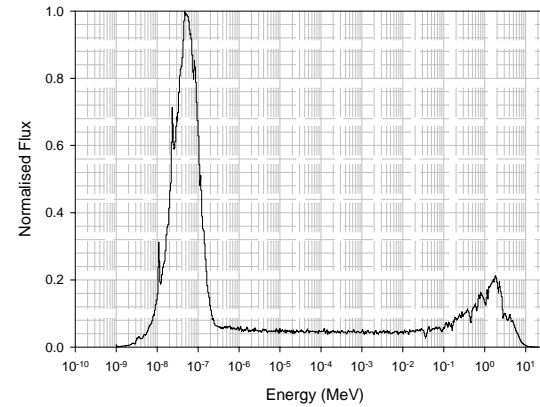


Fig. 3.7. Bismuth cross-section generated to be used in MCNP.

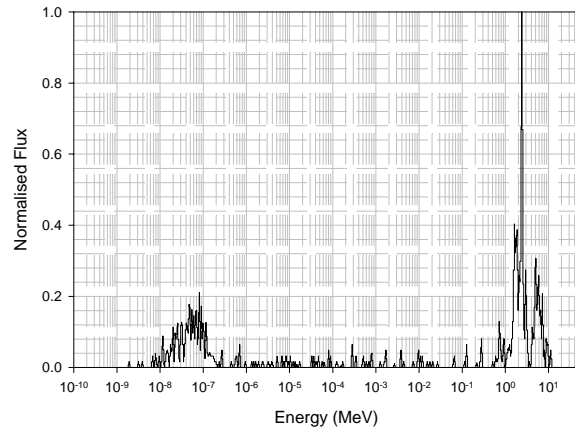
Next the filter length was optimized to get high thermal neutron content, low gamma-ray contamination and the required flux. Table 3.1 shows the possible choices of the lengths of the filter. From the available choices of length, 4-inches bismuth and 6-inches sapphire was selected to be used in our collimator. This length has the largest TNC of $> 99\%$ with an N/G ratio of $1.34 \times 10^6 \text{ cm}^{-2} \text{ mR}^{-1}$. The filter holder is made up of aluminum 6061 and is filled with lead and RX-277 to provide gamma and neutron shielding.



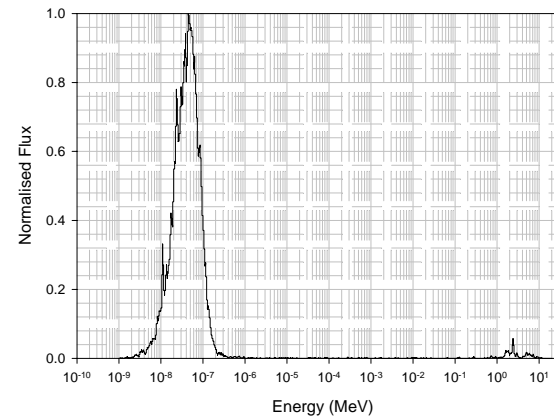
(a)



(b)



(c)



(d)

Fig. 3.8. The neutron energy spectrum at (a) the source (neutron flux = 2.5×10^{12} n/cm².sec), (b) at 6-m image plane without filter (neutron flux = 8.5×10^6 n/cm².sec), (c) at 6-m image plane with 4-inches Bi and 6-inches Sapphire filter using free atom cross-section (neutron flux = 5.6×10^3 n/cm².sec) (d) at 6-m image plane with 4-inches Bi and 6-inches Sapphire filter using generated bound cross-sections (neutron flux = 1.8×10^6 n/cm².sec).

Table 3.1. MCNP calculations done for filter length selection.

Sapp							
Bi	0	1	2	3	4	5	6
0	N Flux = 1.9×10^7 N/G = 8.48×10^3 TNC = 61.16%	N Flux = 1.38×10^7 N/G = 1.05×10^4 TNC = 77%	N Flux = 1.1×10^7 N/G = 1.34×10^4 TNC = 86.9%	N Flux = 9.5×10^6 N/G = 1.80×10^4 TNC = 92.7%	N Flux = 8.4×10^6 N/G = 2.42×10^4 TNC = 96.0%	N Flux = 7.57×10^6 N/G = 3.28×10^4 TNC = 97.7%	N Flux = 6.88×10^6 N/G = 4.43×10^4 TNC = 98.65%
1	N Flux = 1.3×10^7 N/G = 2.34×10^4 TNC = 68.7%	N Flux = 1.0×10^7 N/G = 2.76×10^4 TNC = 82.5%	N Flux = 8.4×10^6 N/G = 3.50×10^4 TNC = 90.35%	N Flux = 7.3×10^6 N/G = 4.55×10^4 TNC = 94.8%	N Flux = 6.5×10^6 N/G = 6.00×10^4 TNC = 97.1%	N Flux = 5.9×10^6 N/G = 8.00×10^4 TNC = 98.2%	N Flux = 5.4×10^6 N/G = 1.08×10^5 TNC = 99.0%
2	N Flux = 9.3×10^6 N/G = 5.34×10^4 TNC = 75.0%	N Flux = 7.5×10^6 N/G = 6.5×10^4 TNC = 86.9%	N Flux = 6.4×10^6 N/G = 8.19×10^4 TNC = 92.8%	N Flux = 5.7×10^6 N/G = 1.12×10^5 TNC = 96.2%	N Flux = 5.1×10^6 N/G = 1.42×10^5 TNC = 97.9%	N Flux = 4.7×10^6 N/G = 1.92×10^5 TNC = 98.8%	N Flux = 4.3×10^6 N/G = 2.56×10^5 TNC = 99.2%
3	N Flux = 6.9×10^6 N/G = 1.20×10^5 TNC = 80.4%	N Flux = 5.7×10^6 N/G = 1.44×10^5 TNC = 90.13%	N Flux = 5.0×10^6 N/G = 1.88×10^5 TNC = 94.7%	N Flux = 4.5×10^6 N/G = 2.51×10^5 TNC = 97.2%	N Flux = 4.1×10^6 N/G = 3.37×10^5 TNC = 98.4%	N Flux = 3.8×10^6 N/G = 4.59×10^5 TNC = 99.0%	N Flux = 3.5×10^6 N/G = 6.14×10^5 TNC = 99.4%
4	N Flux = 5.2×10^6 N/G = 2.68×10^5 TNC = 84.7%	N Flux = 4.5×10^6 N/G = 3.33×10^5 TNC = 92.5%	N Flux = 4.0×10^6 N/G = 4.45×10^5 TNC = 96.13%	N Flux = 3.6×10^6 N/G = 5.88×10^5 TNC = 97.9%	N Flux = 3.3×10^6 N/G = 7.46×10^5 TNC = 98.8%	N Flux = 3.0×10^6 N/G = 1.04×10^6 TNC = 99.4%	N Flux = 2.8×10^6 N/G = 1.34×10^6 TNC = 99.6%
5	N Flux = 4.1×10^6 N/G = 5.94×10^5 TNC = 88.24%	N Flux = 3.6×10^6 N/G = 7.43×10^5 TNC = 94.3%	N Flux = 3.2×10^6 N/G = 9.78×10^5 TNC = 97.0%	N Flux = 2.9×10^6 N/G = 1.32×10^6 Nth/Nft = 98.5%	N Flux = 2.7×10^6 N/G = 1.73×10^6 Nth/Nft = 99.1%		
6	N Flux = 3.3×10^6 N/G = 1.31×10^6 TNC = 90.9%	N Flux = 2.9×10^6 N/G = 1.66×10^6 TNC = 95.7%	N Flux = 2.6×10^6 N/G = 2.14×10^6 TNC = 97.7%	N Flux = 2.4×10^6 N/G = 2.85×10^6 TNC = 98.8%			

Units

Filter length – inches

Neutron flux – $\text{n/cm}^2 \cdot \text{sec}$ N/G – $\text{neutrons cm}^{-2} \text{mR}^{-1}$

* The parameters are calculated at 4m from aperture.

** TNC defined as ratio of flux below 0.3eV to the total neutron flux.

After the sapphire filter the boral diaphragm is placed with the aperture of size $4 \times 4 \text{ cm}^2$ cut into it. Less than 1-cm of boral is sufficient to attenuate most of the thermal neutrons where as more than 10-cm of boral is needed to reduce the fast neutron intensity by an order of magnitude [76]. A boral thickness of 1-inch was selected for the aperture. The divergent collimating piece starts just after the diaphragm with a divergence angle of 2° as has been calculated before. The collimator length has been kept up to the exit of the beam tube. The inside surface of the divergent piece is lined with 0.1-inch thick boral with the outside being filled with RX-277+boral.

3.3 Secondary Collimator Test

MCNP simulations were performed to test the need for a secondary collimation which may be installed in the future. The secondary collimation will start after the beam shutter as shown in Fig. 3.9. The collimator will maintain the divergence angle and will be fabricated in pieces of half or one meter length. In the simulation the secondary collimator was taken to be made of RX-277 with inner boral lining of the same thickness as the primary collimator. The scattered neutron fraction and the total neutron flux were calculated and are shown in Fig. 3.10. The data is normalized to a maximum of unity which occurs at zero secondary length. It can be observed that the scattering component reduces considerably with the increase in length of the collimation. The total flux is not affected much as most of it is constituted by the uncollided flux which is desirable. The decrease of flux at 300-cm of secondary collimator length is steep due to the decrease in the uncollided flux along with the scattered flux. The noise which the scattered component can introduce in the images obtained can be observed in the simulated radiographs and tomographs in chapter 4.

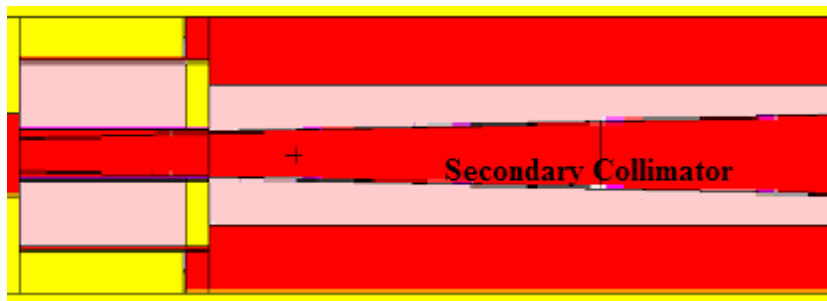


Fig. 3.9. The MCNP geometry of secondary collimator.

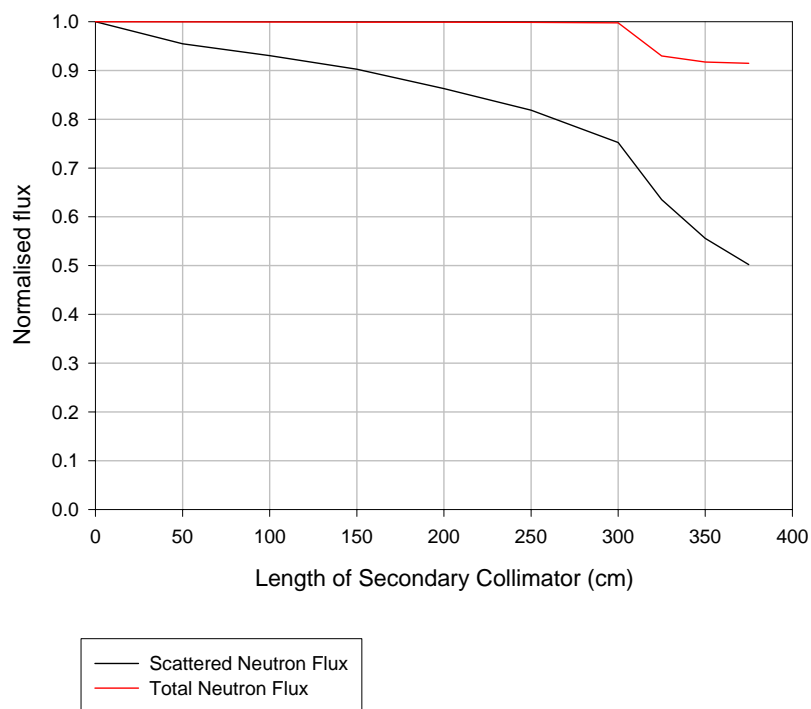
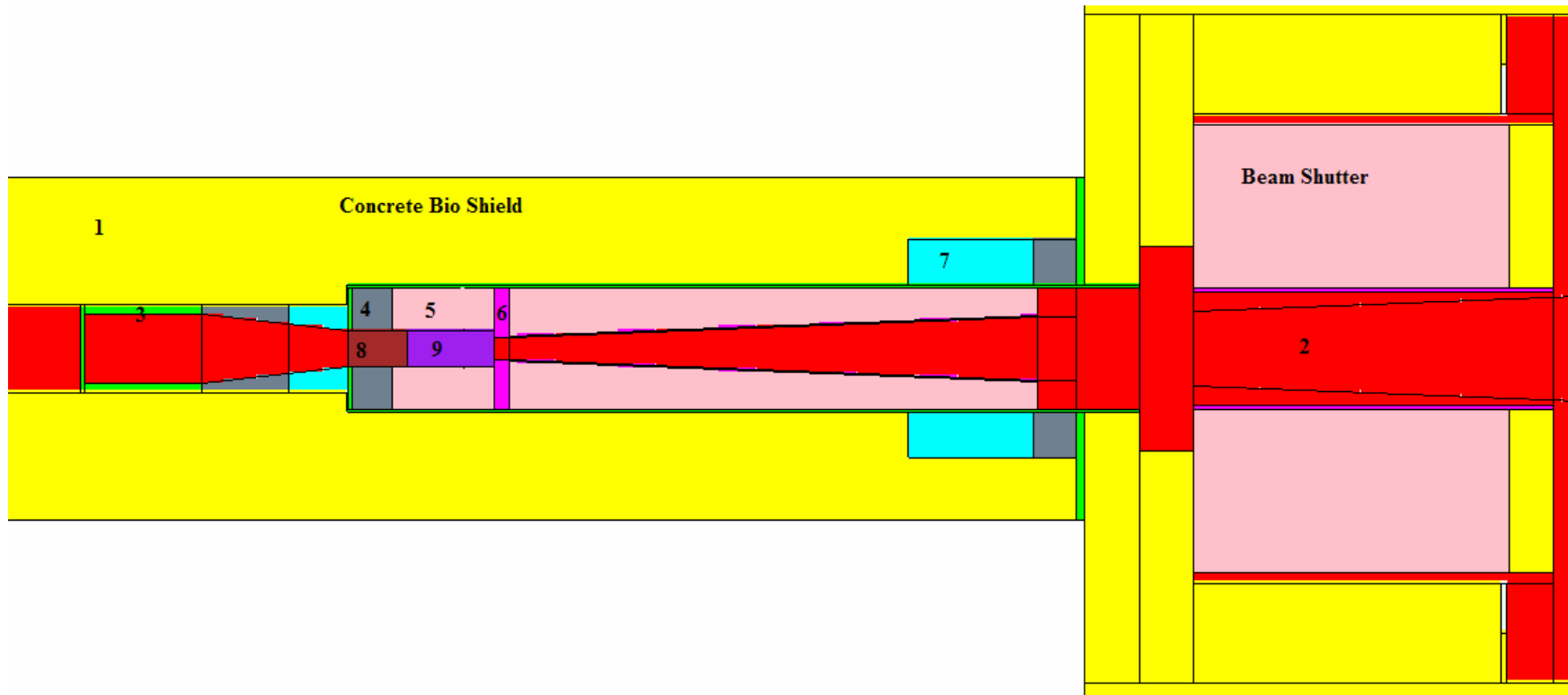


Fig. 3.10. The effect of secondary collimation on the neutron beam.

The final model of the collimator (without secondary collimation) was simulated in MCNP5 to get the neutron flux at the image plane. The MCNP geometry of the simulated model is shown in Fig. 3.11. The neutron spectrum after the filters (4-inches bismuth and 6-inches sapphire) is shown in Fig. 3.8 (d). The model includes the beam shutter and the concrete shielding which will be used in the facility. The neutron flux at the 6-m image plane is 1.8×10^6 n/cm².sec at full power. Other parameters of the collimator are given in table 3.2.

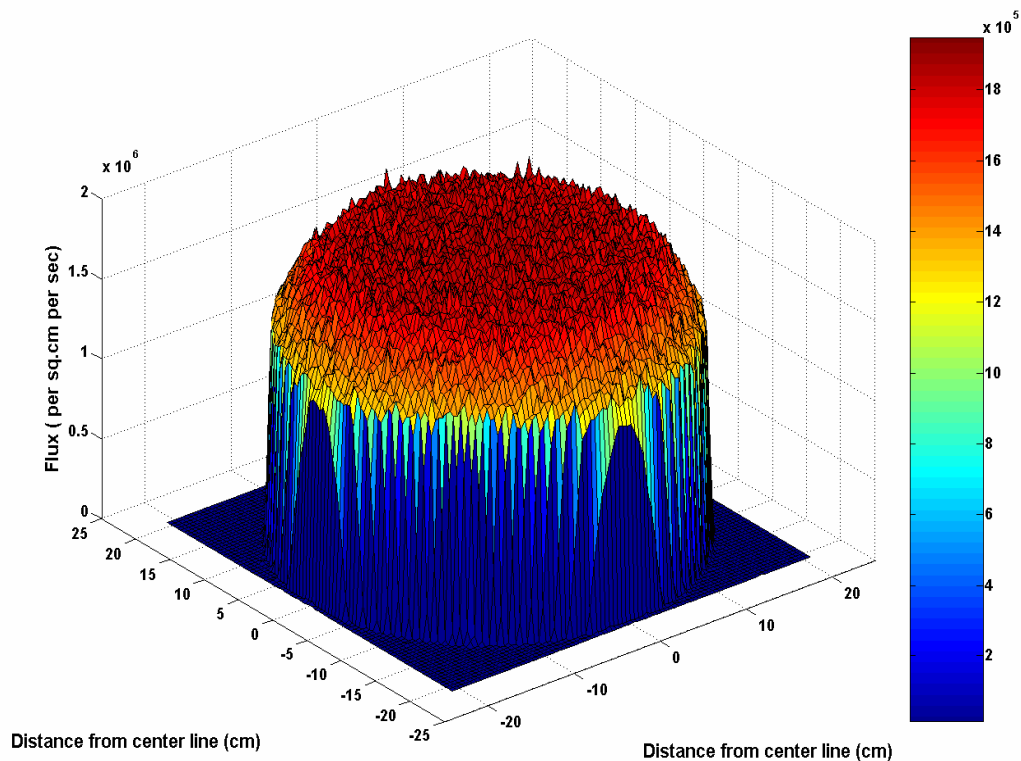


1. Concrete 2. Air 3. Aluminum 4. Lead 5. RX-277 6. Boral 7. Borated Polyethylene 8. Bismuth Filter 9. Sapphire Filter

Fig. 3.11. MCNP model of the imaging facility collimator with the beam shutter.

Table 3.2. Estimated parameters of the imaging facility.

Parameter	Value
Neutron Flux	$7 \times 10^6 - 1.8 \times 10^6 \text{ n/cm}^2 \cdot \text{sec}$
L/D	100-150
TNC	~99%
N/G	$4.43 \times 10^4 - 1.34 \times 10^6 \text{ neutrons cm}^{-2} \text{ mR}^{-1}$

**Fig. 3.12. Neutron flux image at 6-m from the aperture plane.**

MCNP calculations were also performed for the beam size and beam uniformity at the image plane. The MCNP detector flux pin-hole camera tally was used to estimate the flux image at the image plane. The pin-hole size can be adjusted to the region of interest to improve statistics. The thermal neutron flux image at the image plane is shown in Fig. 3.12. From the figure it can be observed that the neutron flux is nearly uniformly distributed at a value of

$\sim 1.8 \times 10^6$ n/cm².sec over ~ 35 -cm width on each side. This makes the beam size at the 6-m image plane to be 35×35 cm² which is sufficient for large size film. The neutron image plate which will be generally used to perform digital neutron radiography is 20×25 cm². The calculated flux image on the image plate is shown in Fig. 3.13. The flux is fairly uniform and varies from $\sim 1.67 \times 10^6$ to $\sim 1.95 \times 10^6$ n/cm².sec.

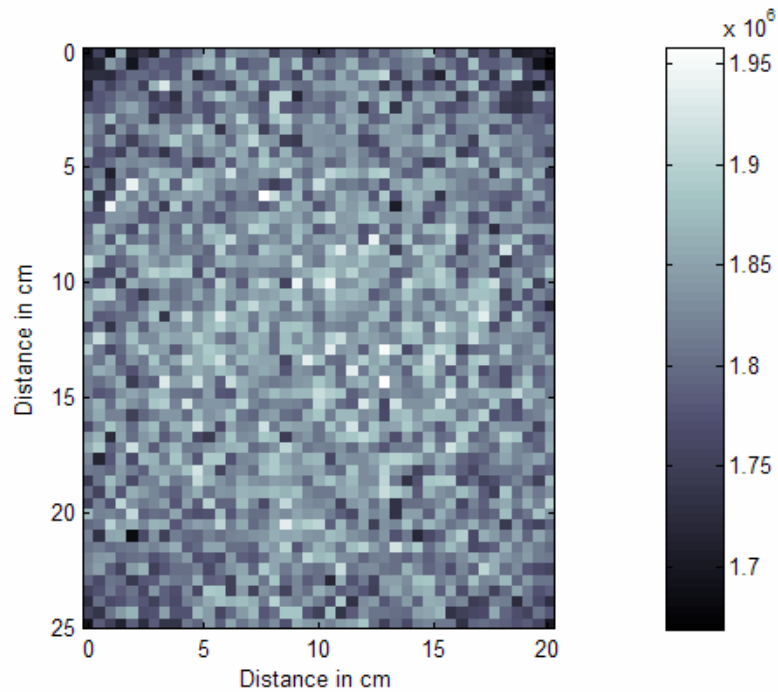


Fig. 3.13. Flux image at the image plate at 6m from the aperture plane.

3.4 Collimator Fabrication

The collimator fabrication was done at the machine shop available in Burlington Labs. The assembly drawing of the collimator is shown in Fig. 3.14. The collimator has modular design and was manufactured into three separate modules:

- The converging section.
- The filter holder.
- The diaphragm and the divergent collimating piece.

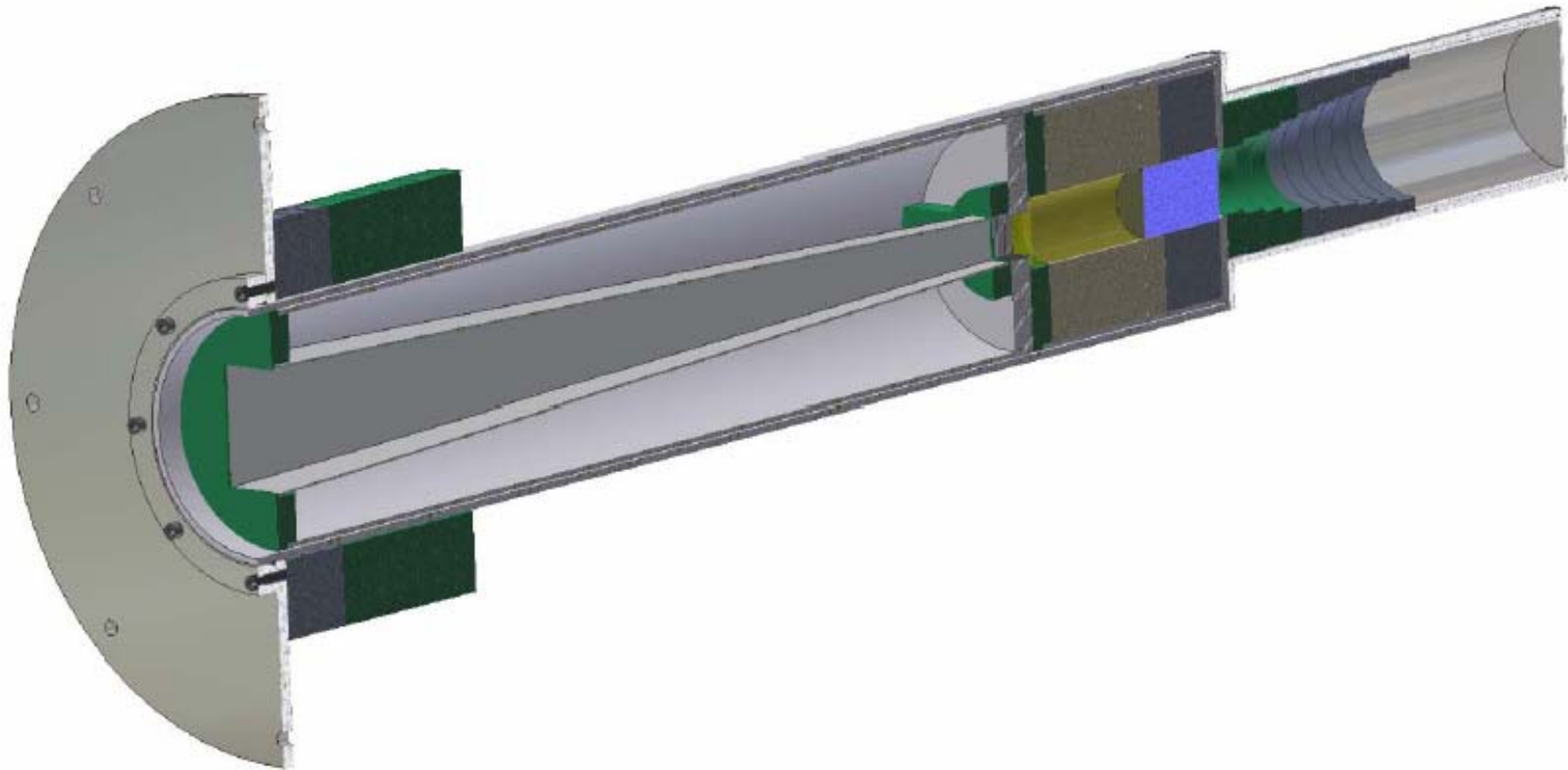


Fig. 3.14. A sectional view of the assembly drawing of the collimator.

The converging section was decided to be made in the form of stepped cylinders instead of the continuous cone section for ease of manufacturing. This change will not affect the collimator characteristics. Just before the converging section is an 8-inches long aluminum spacer which has been placed to keep the space for any other inserts which may be required in future. The collimator was sealed at the front face by welding a 0.25-inch aluminum plate so that it can be helium filled when ever required and also the beam tube can be flooded with water whenever the facility is not in use to reduce the dose. The filter holder is fabricated in separate pieces for bismuth and sapphire. This will allow for a change in beam characteristics by changing the filters in the beam. Three different combinations of filters: only 6-inches sapphire, only 4-inches bismuth or 4-inches bismuth followed by 6-inches sapphire can be obtained. The respective beam characteristics can be obtained from table 3.1. The bismuth filter holder is filled with 4-inches of lead and the sapphire filter holder is filled with RX-277 which was cast inside it. In the collimator design the provision of cooling of filters to liquid nitrogen temperature has been also kept. The cooling of bismuth or beryllium (which may be installed in future) will make the facility much more versatile in terms of beam characteristics. Figure 3.15 shows the sapphire filter which has been used in the collimator. The 6-inches sapphire crystal was obtained from Crystal Systems Inc. of Salem, Massachusetts USA. Two crystals of different grades namely B12 Hemlux and B34 Hemlux were obtained. The letter in the grade refers to the degree of lattice distortion which is present in the crystal. In B12 the measured distortion is $\pm 15'$ and in B34 the distortion is $\pm 28'$. The number in the grade refers to the light scattered by the crystal in a qualitative manner. The B12 grade has better light scatter characteristics than B34 and therefore it is more transparent. The 4-inches bismuth crystal filter was obtained from

Monocrystals Company, Cleveland Ohio. The filter is composed of crystals with average size ~0.5-inch oriented randomly. All the surfaces of the crystal are fine ground.

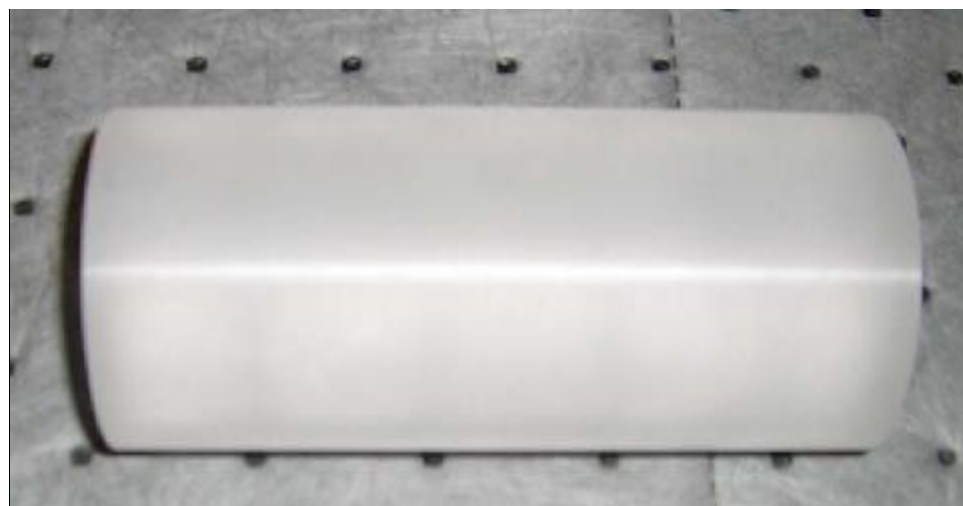


Fig. 3.15. The 6-inches sapphire crystal used in the collimator.



Fig. 3.16. Bare beam tube #5 of the reactor.



Fig. 3.17. The fabricated collimator casing.

RX-277 used in the collimator, was obtained in powder form from Thermo Electron Corporation, USA. The diaphragm is made by cutting 1/10-inch thick boral plate through water jet cutting. The boral plates for collimator lining are also cut the same way in a manner such that they lock against each other making the divergent square cross-section frustum. Bare BT5 in

which the collimator has been inserted is shown in Fig. 3.16. The fabricated collimator casing is shown in Fig. 3.17. The inserted collimator casing and the whole assembly along with the aluminum plate which holds the gasket to provide a water tight seal for beam tube flooding is shown in Fig. 3.18 and 3.19.



Fig. 3.18. Inserted collimator casing inside the beam tube.

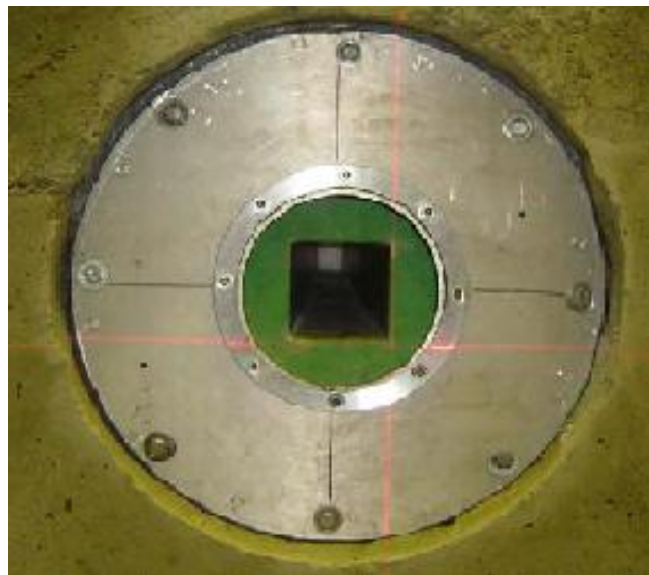


Fig. 3.19. The inserted collimator with the aperture alignment done using laser.

3.5 Beam Shutter

The beam shutter is basically there to shut the beam after the exposure of the sample. This has to have sufficiently thick shielding to stop both the neutrons and gammas when it gets closed. The shutter in our case is a rotating cylinder type. A picture of the beam shutter is shown in Fig. 3.20. In this a cylinder filled with neutron absorbing materials mainly RX-277 is being placed on two rollers in a concrete rectangular section cask. The cylinder has a rectangular hole made for the beam to come out when it opens. The hole has boral lining. This hole aligns with the beam line when it is opened and turns at 90° when it is closed. The closing of the shutter is by gravity and does not operate on any active device and hence there is no safety concern in case of power failure. Also the part of the cylinder which aligns with the beam when it is closed is having a quarter inch thick boral plate followed by 6-inches of lead and then rest is RX-277. The shutter is operated by an air cylinder device which is controlled by the control panel switch. This beam shutter was also included in the MCNP simulation as has been shown in Fig. 3.11 to take into account the scatter effects if any into the MCNP calculations.

3.6 Shielding for the imaging facility

The shielding for the facility is mainly made up of ordinary concrete. Ordinary concrete blocks have been used to make the concrete walls. The shield thickness is about 2-feet in all sides except the beam stop. The shielding calculations were done on MCNP and 2-feet thickness was found to be sufficient. The dose rate with this shielding decreased to about 1mR/hr. The height of the concrete walls has been kept about 6-feet 4-inches. The width of the shield cavity from inside is 4-feet and the available length is 16-feet. The beam stop is made up of one huge

piece of concrete block 3-feet thick with layer of lead inside around 8-inches thick. The shielding may be replaced with permanent cast concrete blocks in future.



Fig. 3.20. The beam shutter for the imaging facility.

3.7 Radiography and Tomography System

3.7.1 Film and Digital Radiography System

Both film and digital radiography system has been set up at the facility. The film radiography system contains:

- The film
- The film developing instruments.
- The film digitizer.

The film which is being used is Agfa D3 single coated manufactured by Agfa Structurix Film Systems. The estimated exposure time for the film at full power is around 30 minutes. For developing the film a dark room is available and presently chemical tank is used to develop the films. But the automatic film development processor will soon be installed for this purpose. A film digitizer is available to digitize the film when ever it is required.



Fig. 3.21. The image reader and the eraser system for digital radiography.

The digital radiography will be done using the neutron sensitive Image Plate (IP-ND) system as has been mentioned in chapter 1. The IP-ND's have been obtained from Fuji Photo Films Corporation. These IP-ND's have the Gd_2O_3 as the converter material. The size of the image plates is $20 \times 25 \text{ cm}^2$. These image plates are read by the BAS-1800 II image reader also manufactured by Fuji Photo Films Corporation. The minimum pixel size obtainable from this scanner is $50\text{-}\mu\text{m}$. This makes the total resolution obtainable from image plate system greater than the films. The scanned image is represented in terms of PSL or QL values. The estimated exposure time for the image plates is ~ 90 sec at full power. The image plate is placed inside a

cassette on which the sample can be placed for the radiography. The cassettes are made by Fuji Films are assumed to have low neutron attenuation. These IP's are fairly insensitive to photons and also have very large dynamic range compared to films as discussed in chapter 2. The read time of the IP is about 2-min. After reading, the IP can be erased by the image plate eraser. This process takes a comparatively longer time of ~40-min. The image reader and eraser system along with an image plate cassette placed on its side is shown in Fig. 3.21.

3.7.2 Real-time Radiography and Tomography System

The real-time radiography and tomography system need the following equipments:

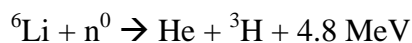
- The sample positioning system: The sample positioning system is required to position the sample accurately at the desired location in desired orientation and to achieve its desired motion during the radiography process to obtain its real-time radiograph or to collect data for tomographic reconstruction. The sample positioning system in our case has three degrees of freedom, two of them being linear along 'x' and 'z' axis and one rotational with axis along 'z' direction. The linear motion is controlled by two stepper motors and the rotational motion is controlled by the servo motor. The linear stages are mounted on the rotational platform. There are 6 position sensors attached to it (three on each linear axis) to get the negative limit, positive limit and home signals. One electromagnetic break is also attached to stop the heavy sample from falling and damaging equipment in case of power failure due to any wanted or unwanted reason. The motors are controlled by the controllers which are signaled by a personal computer. The system requires an initial calibration and after that the position, velocity and acceleration parameters can be controlled very precisely. The system has been manufactured by Cross Automation, N.C. and is shown in Fig. 3.22.



Fig. 3.22. The sample positioning system for real-time radiography and tomography.

- The camera and the camera box: For real-time radiography and tomography a detector system capable of taking data with very high time resolution is required. Also the detector should have an automatic read-out technique and should not need external erasing. A charged coupled device (CCD) camera is well suited for this purpose having the desired properties. But the problem with CCD is that it is sensitive to photons and not neutrons. This necessitates the use of a scintillation screen which will convert the neutron signal into photon signal which will then be read by the CCD. To keep the signal photon separate from the outside light photons a light tight camera box is required with the camera getting the photons reflected by a mirror by a 45° arrangement. The scintillator in our case is NDg

neutron sensitive screen of size 8x8 inch² obtained from Applied Scintillation Technologies. The screen is a blend of ⁶LiF:ZnS:Cu,Al,Au [77]. The screen uses ⁶Li as the converter. The following reaction is utilized to convert the neutrons into tritium and alpha particle [77].



The alpha particle interacts with the phosphor layer to emit photons with a peak at 540-nm which is green color. This is especially suited for CCD detectors. But this is more sensitive to gammas than ND screen. The screen is mounted on 0.5-mm aluminum sheet of the same dimension.

The camera box is made up of black anodized aluminum. The mirror for the camera box is a standard evaporated front surface mirror on soda-lime float glass substrate. The mirror is designed for broadband reflectance over the visible spectrum at 45° angle of incidence, typically utilizing a 4-layer coating design. The layer next to the glass surface is pure aluminum, and the few layers on top of this are typically alternating half-wave layers of two dielectric materials. The top layer of the mirror is silicon monoxide. Reflectivity at 550-nm is guaranteed to be minimum 94% but is typically better [78]. The mirror is of size 11.5”x14”x3mm and has been obtained from Midwest Optical Systems, Palatine, Illinois.

The camera has been obtained from Apogee Instruments Inc., CA. The camera is AP8p and has the CCD array size of 1024x1024. The pixel size is 24-μm and the digital resolution is 16 bit. The exposure time can be varied from 30 milliseconds to 10,400 seconds on 10 milliseconds increment. The typical download time is 30 seconds. To keep the dark current low in the CCD, the camera is cooled by the peltier coolers. The camera is fitted with Nikon 50-mm lens.



Fig. 3.23. The camera box and the camera box positioning system.

- The camera positioning system: The camera positioning system is needed to position camera box (on which camera is attached) at the desired distance and angle, precisely. The camera positioning system need not be moved during data collection and therefore no motorized control is applied. The system again has three degrees of freedom, two being linear along 'x' and 'z' axes and one rotational with its axis along the 'y' direction. In this case the rotational stage is mounted on the 'z' axis which in turn is mounted on 'x' axis. The camera will be mounted on the rotational platform. The system has been supplied by Cross Automation. In Fig. 3.23 the camera box with the camera and the camera positioning system is shown.

The actual setup of the real-time radiography and tomography facility is shown by a block diagram in Fig. 3.24. The image digitizer is attached with the camera and the frame storage and frame processor is inbuilt in the computer only.

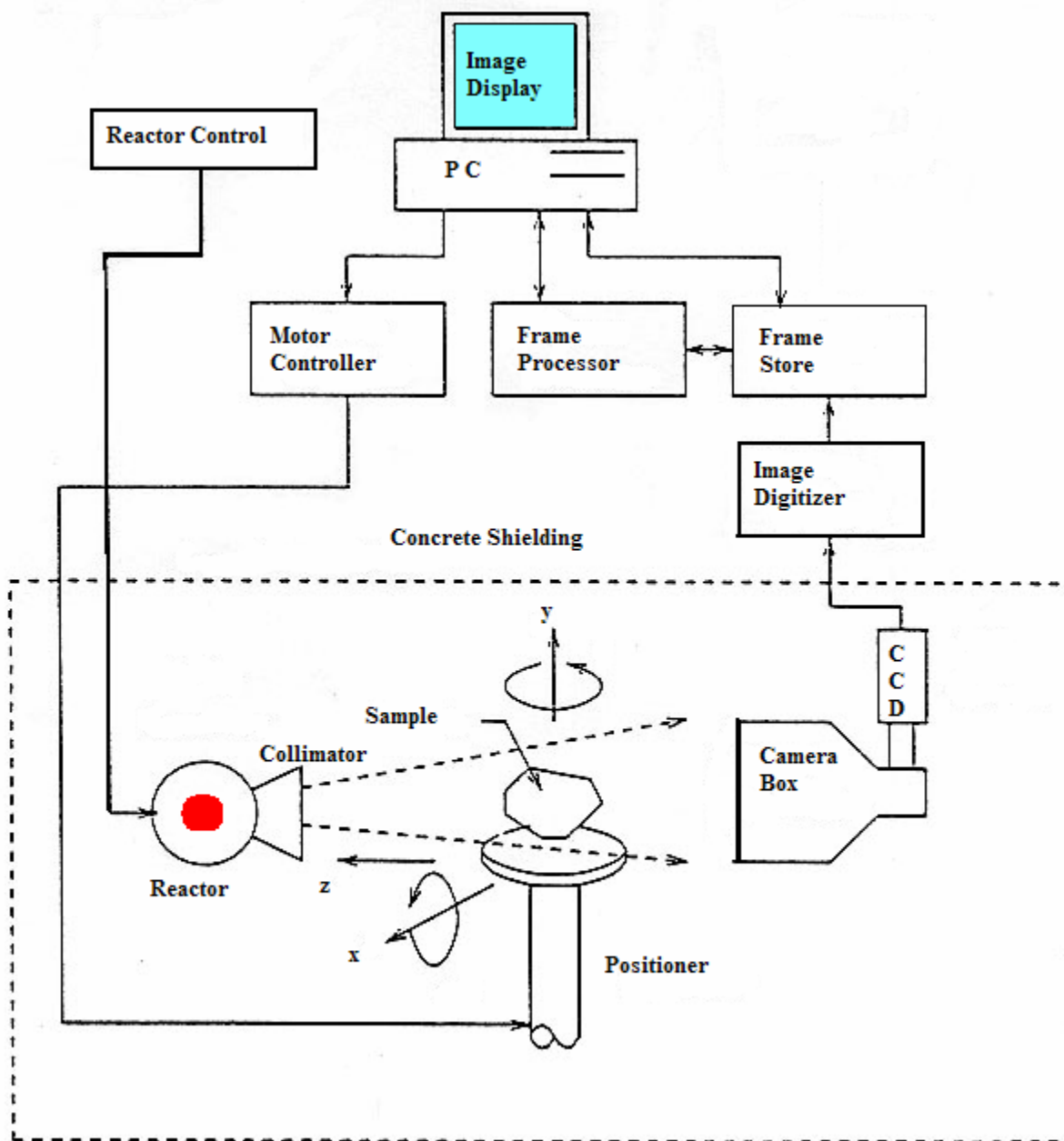


Fig. 3.24. A Schematic of the real-time radiography and tomography setup at the PULSTAR.

Chapter 4

Characterization and Test Results

4.1 Simulated Test Results

MCNP simulations were performed to assess the neutron radiography and tomography capabilities of the PULSTAR neutron imaging facility. From the simulation the quality of the radiograph and tomogram which will be obtained can be estimated. The pin-hole detector mesh tally was used for the simulation.

4.1.1 ASTM Beam Purity Indicator Radiograph Simulation

The ASTM standard for neutron radiography includes two sample radiograph tests:

- Beam Purity Indicator (BPI) test
- Sensitivity Indicator (SI) test

The BPI and SI are shown in Fig. 4.1 and 4.2. The dimensions of these samples and their exact make up are explained in ASTM standard E545 [22].



Fig. 4.1. ASTM BPI test sample.

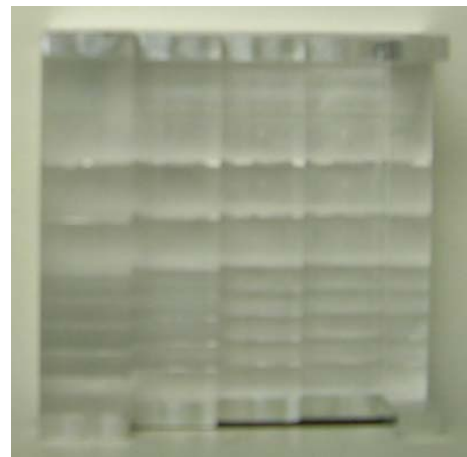


Fig. 4.2. ASTM SI test sample.

The BPI was simulated with MCNP5 using the designed collimator. The grid size taken for the detector array had a resolution of 50- μm . The distance between the sample and the image plane is 2.5-mm. The obtained radiographs of the uncollided and the total flux are shown in Fig. 4.3 from (a) to (d). The outer circle in the figure represents the pin-hole diameter. Figure 4.3 (a) and (b) are the direct flux images of the BPI. Figure 4.3 (c) and (d) are processed to be more smooth by inverse log transformation which is a one-to-one transformation. The difference between both of them can be clearly observed from the figure. The scatter component in the total flux radiograph can be clearly seen in the inverse log radiograph.

ASTM standard E545 specifies calculation of some parameters from the film radiograph of BPI based on which the beam quality is determined. Assuming the radiograph to be taken in the linear region of the response curve of the film, which is the desired case, the optical density should be directly proportional to the neutron flux. Therefore the neutron flux averages in different parts of the BPI were calculated and are given in table 4.1. Using these results, the ASTM specified parameters were estimated. The parameters are listed in table 4.2.

Table 4.1. Average neutron flux in different regions of BPI.

Region of BPI	Average Neutron Flux per source particle ($\text{n}/\text{cm}^2\cdot\text{sec}$)
Central Hole	4.3977×10^{-6}
Polytetrapolyethylene	3.3357×10^{-6}
Boron Nitride disc 1	2.0256×10^{-8}
Boron Nitride disc 2	1.9174×10^{-8}
Lead disc 1	3.3538×10^{-6}
Lead disc 2	3.3427×10^{-6}

Table 4.2. ASTM parameters calculated using the simulated BPI.

Description	TNC %	%Scatter
MCNP simulated BPI	99.3	0.45

The TNC matches closely the calculated value of the TNC obtained for the 6-inches sapphire and 4-inches bismuth in table 3.1.

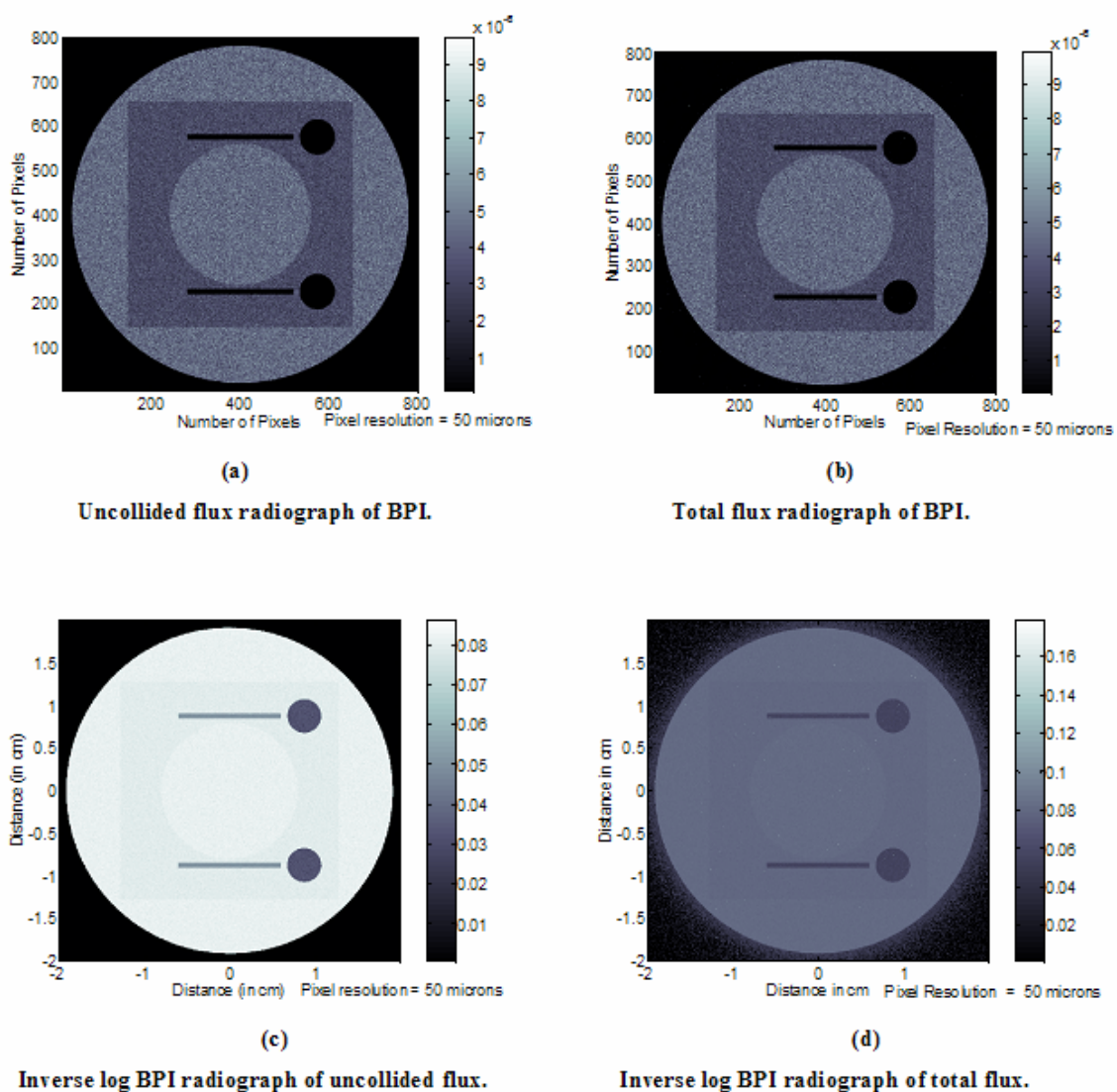


Fig. 4.3. The MCNP simulated radiograph of BPI. In figure (c) and (d) the inverse log image is the image where $\frac{-1}{\log(\phi)}$ is the neutron flux.

4.1.2 Tomogram Simulation

Two tomograms were simulated using MCNP5. The sample was selected to consist of common materials which are used in neutron radiography.

Sample 1- The first sample selected for tomogram simulation is of cylindrical shape with circular cross-section made up of iron. Along the axial direction there are 4 holes, one at the center with a 3.0-mm diameter and 3 others that are 2.0-mm in diameter. The 3 holes are equally spaced at 120° each on a radius of 3.25-mm. The center hole is filled with cadmium and the other three holes are filled with water, lead and air. The sample has 10-mm diameter and height of 10-mm. The sample cross-section is shown in Fig. 4.4 (a). The size is kept relatively small to have better projection data in less time with high grid resolution. The grid resolution in this case is 50- μm . The detector array was kept 0.25-cm apart from the sample. The number of rays in this case is equal to 400 and the number of views is 18, each at 10° interval. The projection data obtained was reconstructed using the FBP reconstruction technique as discussed in chapter 2 using a Ram-Lak filter. The reconstruction was done for both the uncollided and the total flux projection data. The expected difference between the two images is due to the noise due to scatter component in the beam. The sinogram and tomogram for both the uncollided and the total flux data is shown in Fig. 4.4. The outer circle in the figure is the pin-hole diameter taken in the projection data generation to improve the statistics. From the figure it can be clearly observed that the scattering component is degrading the image. But the noise is small and can be removed to a large extent using image processing techniques. Also it can be observed as expected that cadmium at the center of the cylinder is very clearly visible. Water is also visible inside the iron cylinder but lead and air are almost invisible as they have low thermal neutron cross-sections.

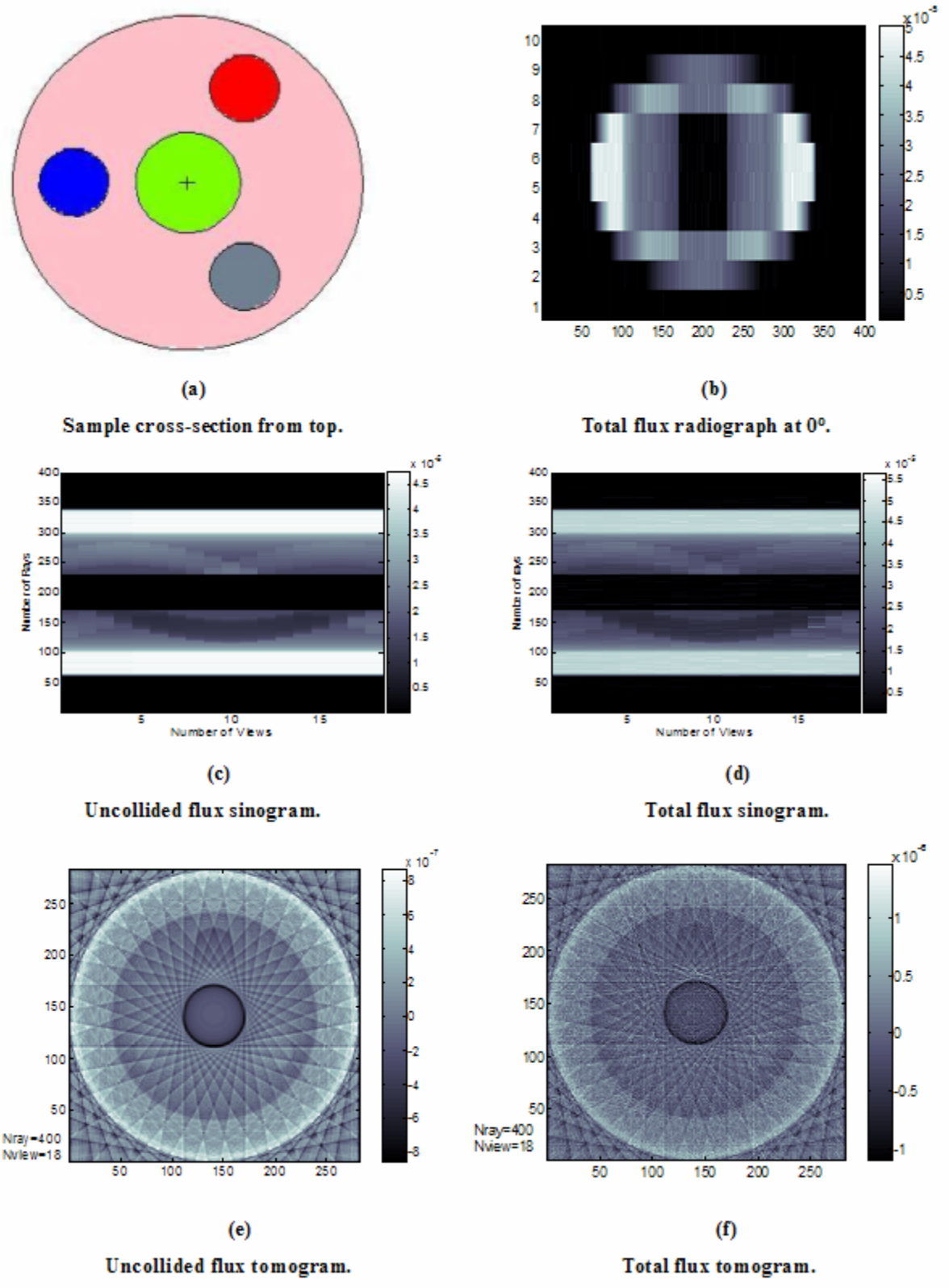


Fig. 4.4. Tomographic reconstruction of Sample 1.

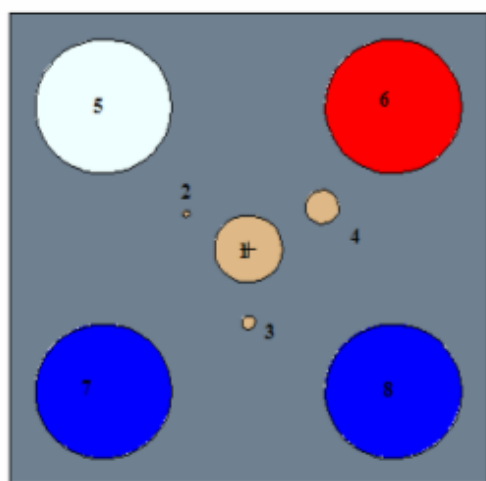
Sample 2 – The second sample selected was a square lead block in which there were 7 through holes and one cadmium cylindrical insert at the center. The sample cross-section from the top and side are shown in the Fig. 4.5 (a) and (b) respectively. The diameters of the cylindrical holes and the central insert along with the materials filled inside them are given in table 4.3. In this case the sample size was $7 \times 7 \times 10 \text{ mm}^3$. In this case the sample detector distance was 0.25-cm. The resolution of the image grid taken was again 50- μm which equal to the minimum scanner pixel size. The number of rays in this is 400 and number of views is 32 each at an increment of 5° . The reconstruction algorithm applied is FBP with a Ram-Lak filter. The reconstruction for both uncollided and total flux was done. The results of the simulation are shown in Fig. 4.5 from (c) through (h).

Table. 4.3. The specification of Sample 2 used for tomograph simulation.

Hole Number	Material	Center Location (x, y) (mm)	Diameter (mm)
1 (Insert)	Cadmium	(0,0)	1.0
2	Cadmium	(0.525, -0.9093)	0.1
3	Cadmium	(-0.11,0)	0.2
4	Cadmium	(0.0625,0.10825)	0.5
5	Steel	(0.2121, -0.2121)	2.0
6	Air	(0.2121,0.2121)	2.0
7	Water	(-0.2121,-0.2121)	2.0
8	Water	(-0.2121,0.2121)	2.0

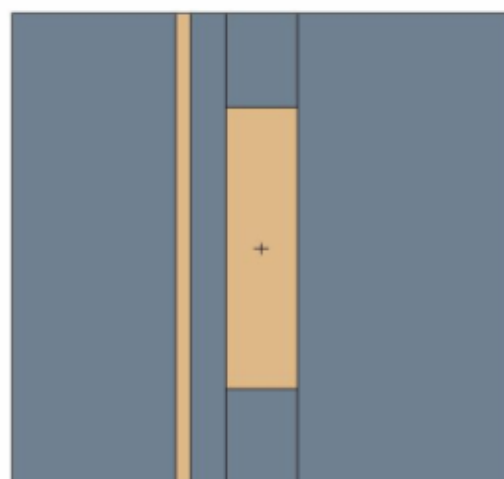
From the reconstruction it can be observed that there is not much scatter noise in the tomogram. Also the cadmium rod of smallest diameter of 100- μm is also clearly visible in tomogram. The two water holes in the lead are also visible. For neutron imaging, this exercise demonstrates that it is capable of imaging light materials like water even when it is inside high 'Z' material. The steel and air holes are not clearly visible as for the thickness taken there will

be a small attenuation difference between steel, air and lead. Also it can be concluded by comparison of the Sample1 and Sample2 tomograms that the image quality increases as the number of views are increased which is expected.



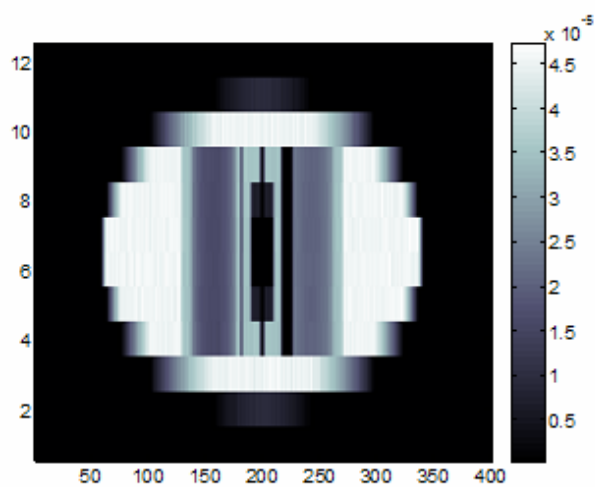
(a)

Sample cross-section from the top.



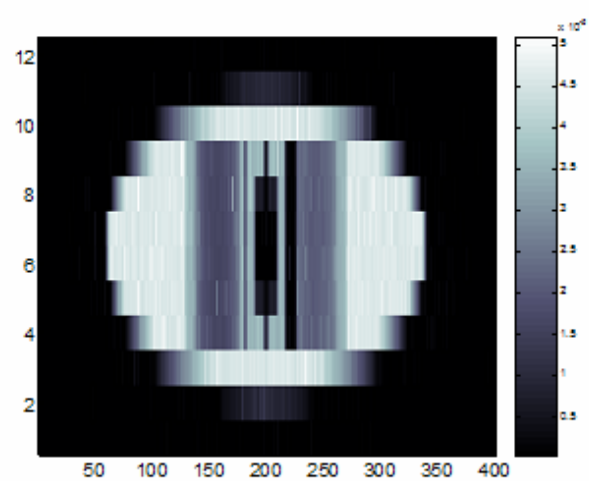
(b)

Sample cross-section from the side.



(c)

Uncollided flux radiograph at 0° .



(d)

Total flux radiograph at 0° .

Fig. 4.5. Imaging and tomographic reconstruction of Sample 2.

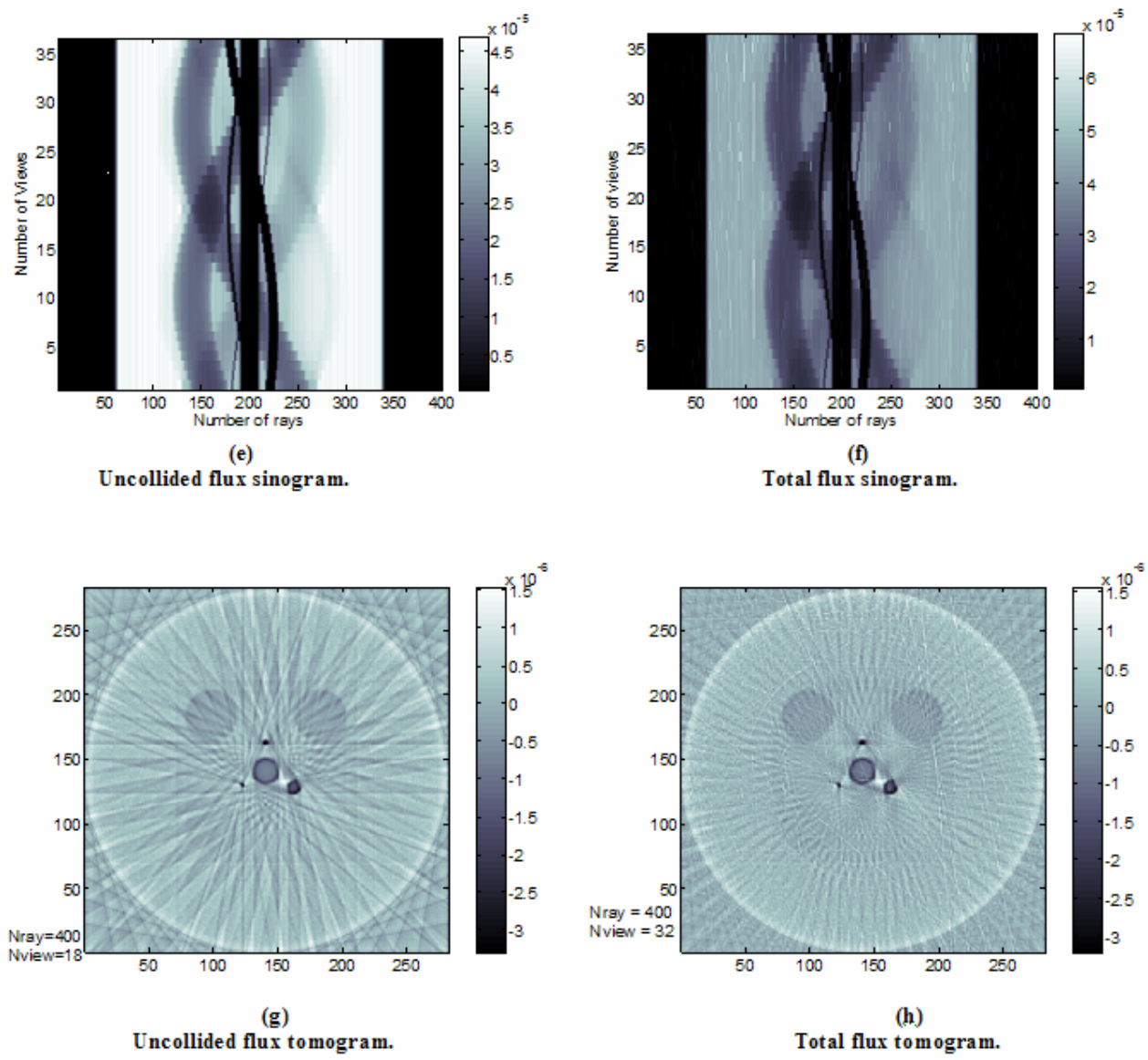


Fig.4.5. continued.

4.1.3 Point Spread Function MCNP Simulation

The point spread function (PSF) simulation for calculation of image resolution was done on MCNP using the above designed collimator. A general description of PSF has been done in chapter 2. In the PSF simulation done here the geometric unsharpness effect and the screen grid resolution unsharpness has been taken into consideration. The inherent unsharpness of the

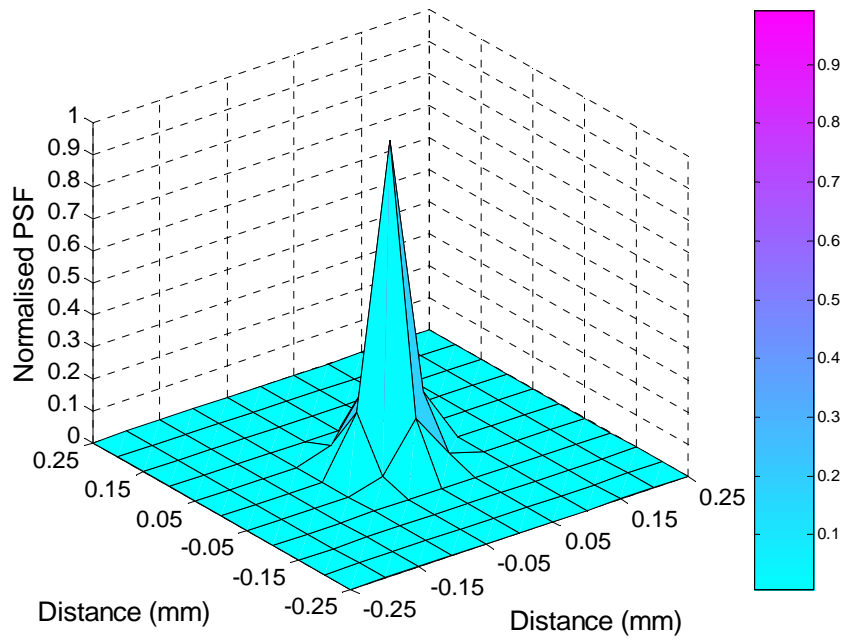
converter due to the phosphorescence or the photo stimulated luminescence and the unsharpness due to grain size of the emulsion has not been modeled. The integral of PSF over a line gives the line spread function (LSF). Therefore, if the material in the transverse direction is assumed to be purely absorbing the PSF cross-section from the central plane in that direction can be approximated as the LSF at that point.

The PSF was simulated for an L/D of ~ 100 . The object to image plane distance was 10-mm. The image grid was taken to have 50- μm resolution which is the smallest pixel size of the BAS 1800-II image reader. The PSF and the corresponding FWHM was observed to be dependent upon the location of the point source relative to the square grid. The PSF obtained for the point source located at the grid center and on the grid boundary using MCNP is shown in Fig. 4.6 (a) and (b) respectively. The PSF was normalized to have a maximum value of 1. The square grid or pixels taken give the PSF a discrete step look. The first observation which can be made from the simulated PSF is that it is not isotropic. This feature comes due to the pixel shape, which is square and therefore isotropy at the pixel size scale cannot be captured. But with more pixels taken into consideration the isotropy becomes more visible. This is supported by the shape of PSF which tends to become more isotropic as it starts spreading near the base. The transverse cross-section of the PSF along the X-axis is shown in Fig. 4.7. The FWHM which can be obtained from the PSF cross-section is between 61 to 100- μm . The calculated value of geometric unsharpness at 10-mm distance from the object plane is 100- μm which is the maximum value obtained from the PSF simulation. The smaller values in the range can be explained by the fact that lower beam divergence is observed by the pixel for some location of the point source than the other and therefore the grid discretization affects the resolution less at

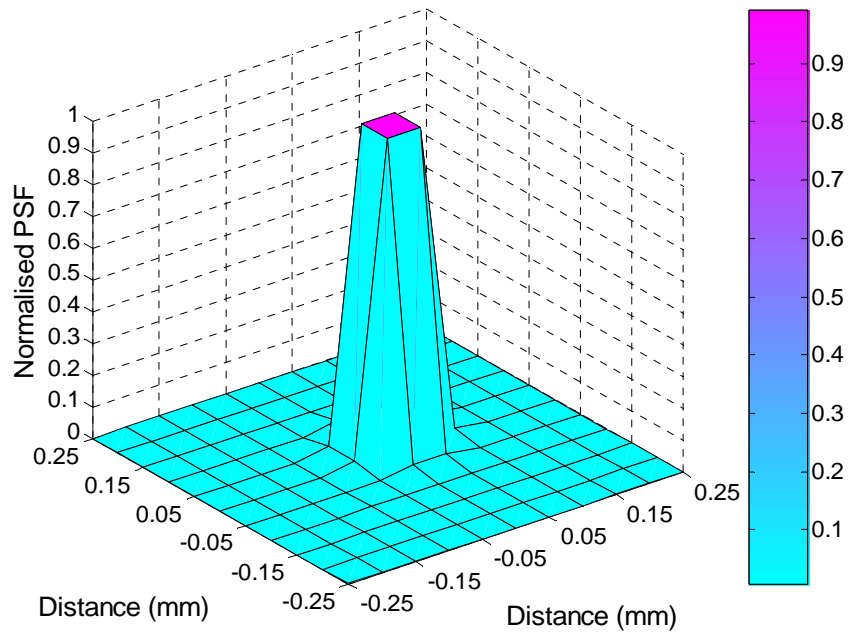
some locations than the other. The corresponding modulation transfer function (MTF) is shown in Fig. 4.8 obtained by calculating the 2D Fourier transform of the simulated PSF.

The PSF adjustment was also done for the film, image plate and scintillation screen (with CCD) using their inherent resolution (20- μm , 93- μm [79] and 100- μm [80] respectively) that was linearly added to the geometric resolution [53]. The object to recorder distance was taken to be ~2.5-mm which is the approximate thickness of the recorder cassette. The resultant unsharpness obtained was converted in terms of effective object image plane distance using L/D of 150 and the MCNP simulation was done to get the PSF. In this case also the PSF and the corresponding FWHM was observed to be dependent upon the location of the point source relative to the grid. But as the grid size tends to become smaller compared to the resolution this location effect diminishes. The adjusted PSF for the source at the grid center are shown in Fig. 4.9 (a) through (f). In the case of film the grid resolution taken was 25.4- μm which is the digitizing resolution for the film and for the real-time system PSF the pixel size was taken as 24- μm instead of 50- μm as the CCD resolution to be used has 24- μm pixel size. The obtained resolution range at FWHM is ~33 to 50- μm , ~106 to 118- μm and ~113 to 118- μm for the film, image plate and scintillation screen detection system respectively depending upon the location of the point source relative to the pixel.

The other feature which can be observed from the PSF is that the pixels adjacent to the pixel where FWHM was calculated also have effect on their average value. This effect will increase as the geometric unsharpness increases. Therefore the resolution can also be taken as the number of pixels required to fully confine the PSF. In this definition the resolution will change in steps of pixel size.

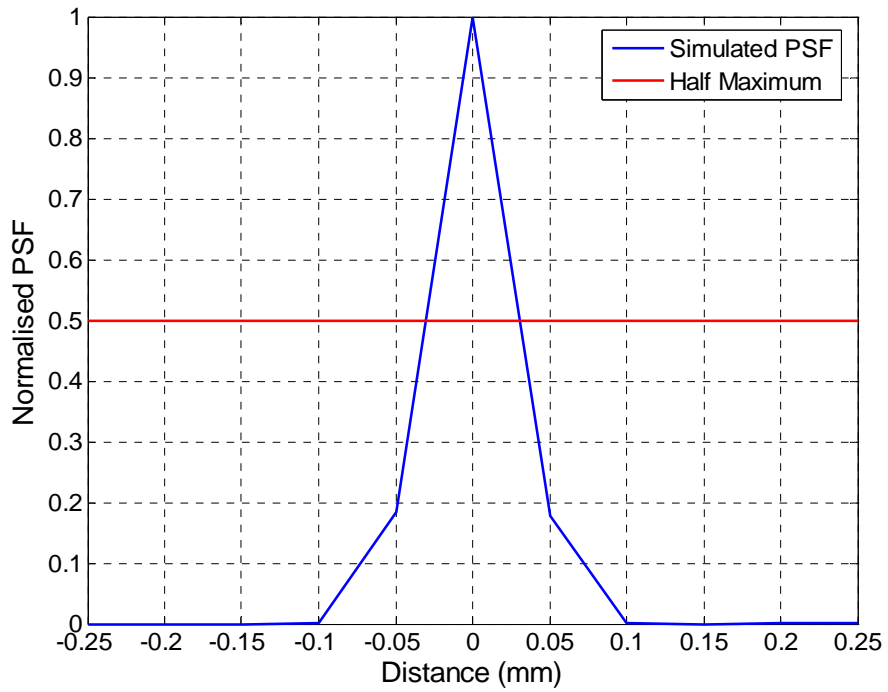


(a)

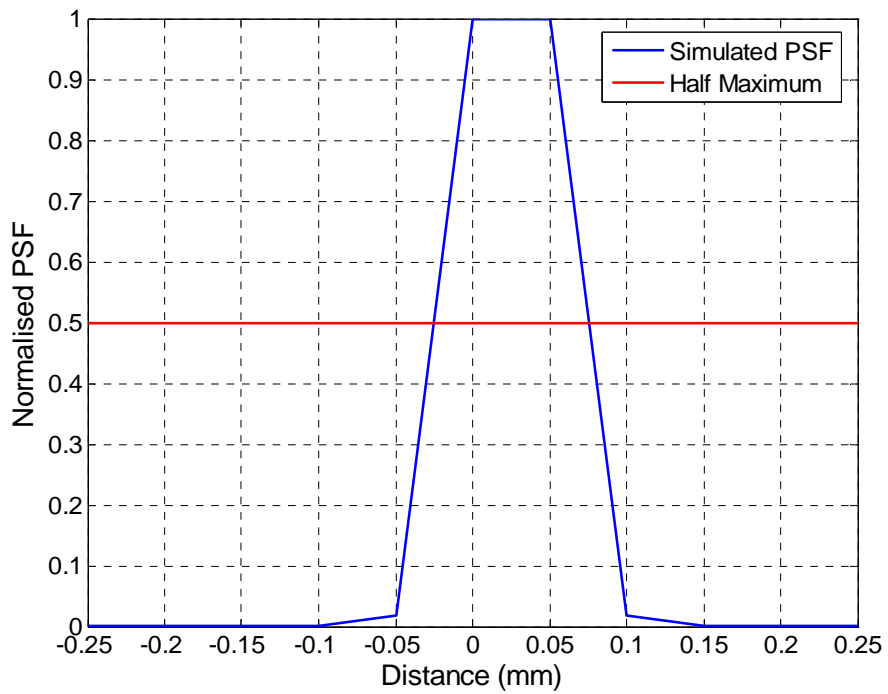


(b)

Fig. 4.6. The PSF obtained with MCNP using a 50- μm grid resolution for object screen distance of 10-mm and L/D of 100 (a) with point source at the center of the square grid and (b) at the boundary of the square grid.

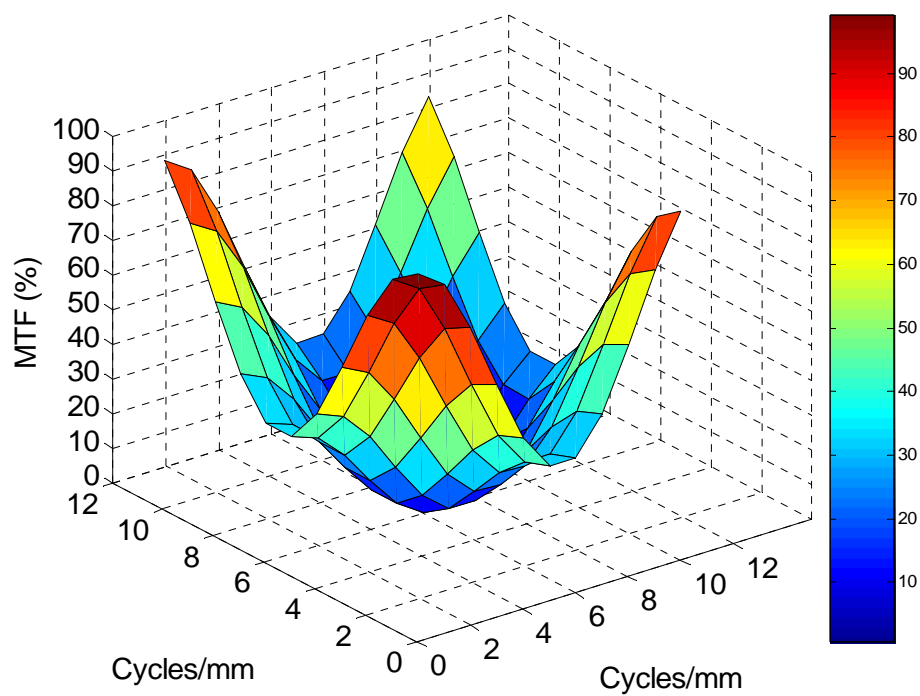


(a)

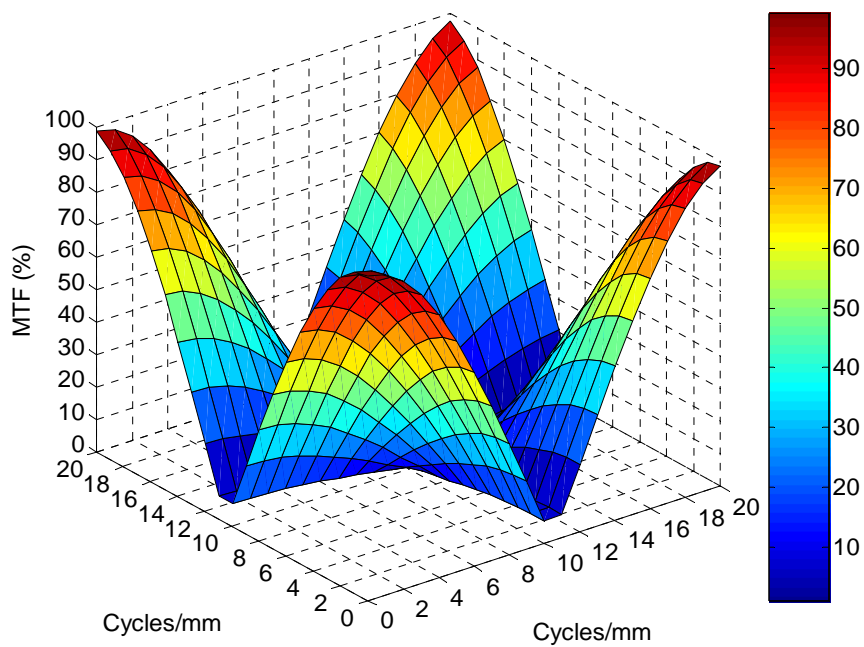


(b)

Fig. 4.7. Vertical cross-section of the PSF (a) for the point source at the grid center and (b) for the point source at the grid boundary.



(a)



(b)

Fig. 4.8. Modulation transfer function obtained using simulated PSF (a) for the point source at the grid center and (b) for the point source at the grid boundary.

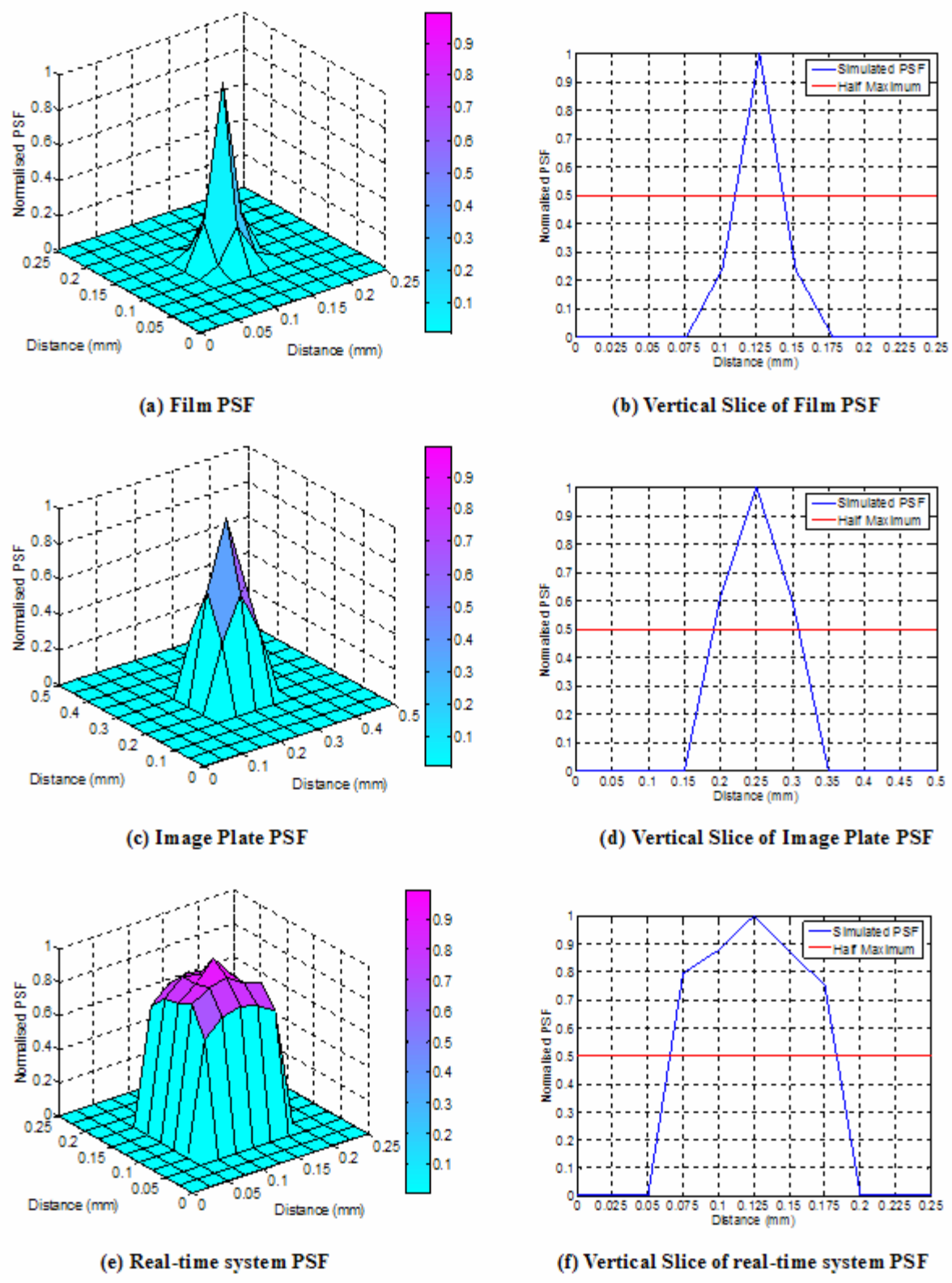


Fig. 4.9. Simulated PSF for different detection systems.

4.2 Measurements and Characterization

For the characterization of the neutron beam and the collimator and for the verification of the MCNP simulated results measurements were taken before and after the installation of the designed collimator in chapter 3. ASTM standardization of the beam was also done after the installation of the designed collimator.

4.2.1 Flux Measurements

The neutron flux measurement using 2-mm gold foils was performed using the designed collimator. Gold foil activation is a standard technique used for neutron flux measurement and its details can be found elsewhere [ASTM E-262 Ref. 22]. The average neutron flux obtained was 1.84×10^6 n/cm².sec at full reactor power. The Cd ratio was obtained ~450. The MCNP calculated thermal flux was 1.8×10^6 n/cm².sec. Thus the simulated result is in good agreement with the measured thermal flux.

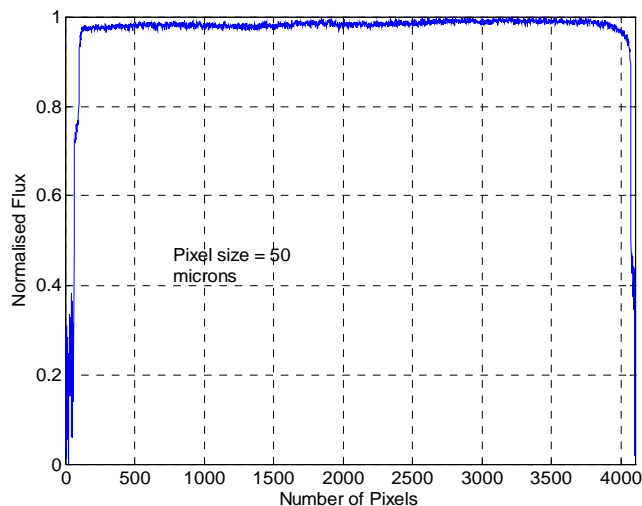


Fig. 4.10. The neutron flux profile on the image plate.

The neutron flux profile was also obtained using the bare image plate and is shown in Fig. 4.10. As estimated using MCNP the flux profile is very uniform and therefore there will be

uniformity in the exposure and hence density of the radiograph image. The beam size which has been calculated using MCNP is being verified presently.

4.2.2 ASTM Standardization

ASTM standardization of the imaging facility was done with the BPI and the SI according to the ASTM Standards E545. The digitized film radiographs of the ASTM samples are shown in Fig. 4.11 and 4.12. For qualitative comparison with the film the radiograph of ASTM samples obtained using the image plates is shown in Fig. 4.13 and 4.14. It can be clearly observed that film radiographs are sharper and have more resolution than the image plate radiographs. But image plate has a very big advantage of much less exposure time over the films. The results of the test are presented in the ASTM Test Report on page 89.

In the ASTM calculations that follows the effective thermal neutron content is $\sim 73.45\%$ which is much lower than the TNC calculated using simulated BPI radiograph which was $>99\%$. This is assumed to be due to the conversion process which has not been taken into consideration in the simulation. Also the type of recorder being used affects the values of the ASTM parameters as is clear from the table 4.4 which lists ASTM parameters calculated using image plate PSL values. This effect is probably due to the different sensitivity of the recorder to neutrons and gammas and the conversion efficiency which is energy dependent. That is the probable reason it is called *effective* thermal neutron content in the ASTM standard. In the TNC calculations done in the simulations the thermal neutron energy cut off was taken as 0.3eV. The 74% TNC is obtained from the neutron energy spectrum obtained from MCNP calculations when the energy cut off for the thermal neutrons is taken as $\sim 0.06\text{eV}$ which is slightly higher than the most probable energy of $\sim 0.045\text{eV}$. This difference is in further investigation presently.

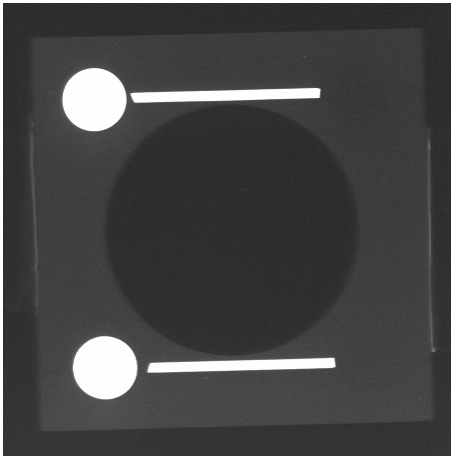


Fig. 4.11. BPI digitized radiograph from film.

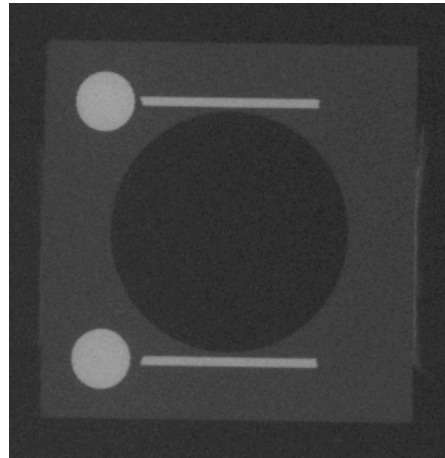


Fig. 4.13. BPI digitized radiograph from image plate.

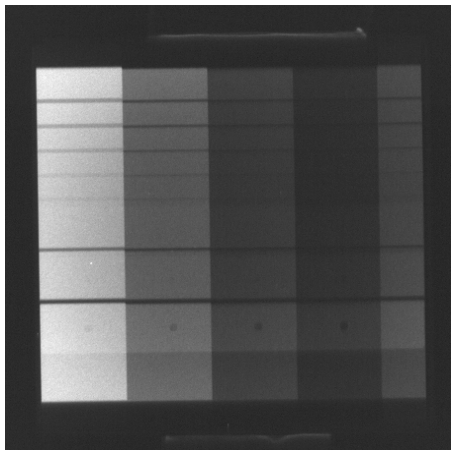


Fig. 4.12. SI digitized radiograph from film.

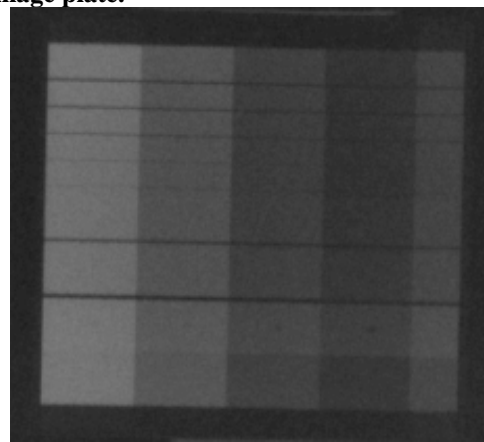


Fig. 4.14. SI digitized radiograph from image plate.

Radiography data of ASTM Beam quality Indicators on Film

Measurements done according to E-545.

Date- 12 June 05

BPI measurement data

D_{b1} = density in the 1st boron nitride disc = 0.72

D_{b2} = density in the 2nd boron nitride disc = 0.65

D_{L1} = density in the 1st lead disc = 2.52

D_{L2} = density in the 2nd lead disc = 2.57

D_H = density in the hole of BPI = 2.90

D_T = density in the polytetrafluoroethylene = 2.50

$\Delta D_b = D_{b1} - D_{b2} = 0.07$

$\Delta D_L = D_{L1} - D_{L2} = 0.05$

NC = effective thermal neutron content = $\frac{D_H - (\text{highest } D_b + \Delta D_L)}{D_H} \times 100$
= 73.45%

S = effective scattered neutron content = $\frac{\Delta D_b}{D_H} \times 100 = 2.41\%$

γ = Effective gamma content = $\frac{D_T - (\text{lowest } D_L)}{D_H} \times 100 = 0.689\%$

P = Pair Production content = $\frac{\Delta D_L}{D_H} \times 100 = 1.72\%$

Sensitivity Indicator

H = Number of Holes visible = 7

G = Number of gaps visible = 7

Neutron Radiography category = I^A

Table. 4.4 ASTM parameters calculated using image plate PSL values.

ASTM Parameters	Obtained Value (%)
NC	77.58
S	1.96
γ	0.1916
P	0.38
Number of holes visible in SI	4
Number of gaps visible in SI	7

4.2.3 Spread Function and Resolution

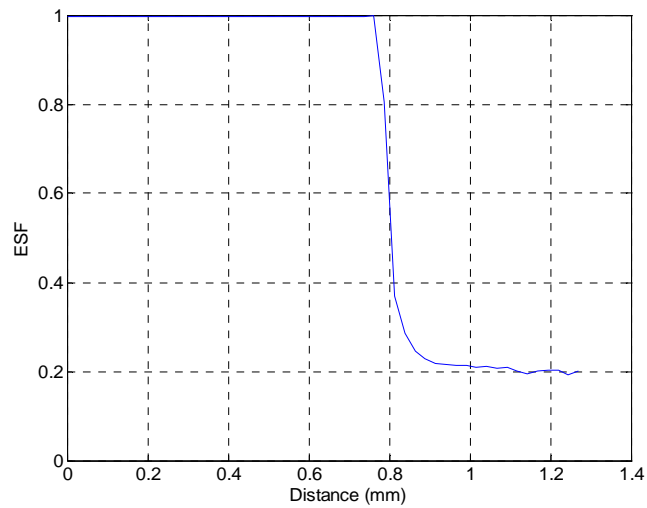
As discussed in chapter 2, spread functions are used to characterize the resolution of the imaging system. To get the estimate of resolution of our imaging facility at the 6-m image plane using films and image plates, the LSF was calculated from the ESF, obtained from a 25- μm thick gadolinium foil. The film was digitized at 1000-dpi which translates to 25.4- μm resolution. The image plate has been obtained from Fuji Films and has a pixel size of 50- μm . The foil was placed in contact with the cassette.

The ESF obtained from the film is shown in Fig. 4.15 (a). The ESF was numerically differentiated to get the LSF. The LSF is shown in Fig. 4.15 (b). The LSF was normalized to have a maximum of unity. The LSF is fairly smooth and the FWHM can be obtained from the LSF. Also as discussed in chapter 2 for films exponential and Lorentzian functions are fairly good approximations of the LSF. Therefore these two functions were tried for fitting the experimentally obtained LSF. The fitting functions are given by

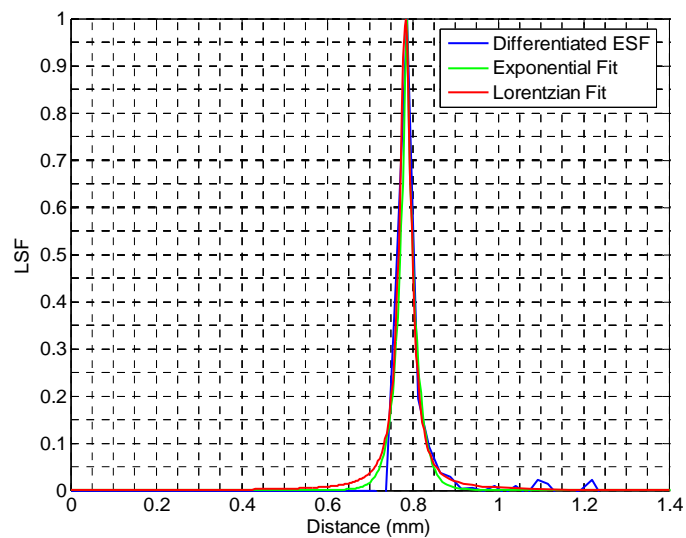
$$LSF(x) = a + \frac{1}{1 + [\lambda(x-b)]^2} \quad (4.1)$$

$$LSF(x) = a + \exp[-\lambda|x-b|]$$

Here a and b are the location parameters to account for the offset of the radiographic data from the origin. The parameter λ determines the actual resolution. These parameters were obtained by nonlinear curve fitting using MATLAB. The fitted parameters and the FWHM obtained from actual LSF and the fitted functions are given in table 4.5. In the table the norm is defined as the sum of square of deviations between the data point and the fitted function.



(a)



(b)

Fig. 4.15. (a) ESF obtained using films and (b) the LSF for the radiographic film.

Table. 4.5. The LSF data for the film.

Film LSF	a	b	λ	Norm	FWHM (μm)
Experimental	-	-	-	-	39
Lorentzian fit	0	0.7833	61.1007	0.0307	33
Exponential fit	0.0010	0.7861	47.9820	0.0421	29

The ESF obtained from the image plate is shown in Fig. 4.16 (a). The ESF was again differentiated numerically to obtain the LSF. The LSF obtained is shown in Fig. 4.16 (b). In this case the Lorentzian and Gaussian fitting functions were used to fit the LSF as given in Eq. 4.2. The obtained fitting parameters and the FWHM are given in table 4.6. It is clear from the norm value given that Gaussian is a better fit for the image plate as was mentioned in chapter 2.

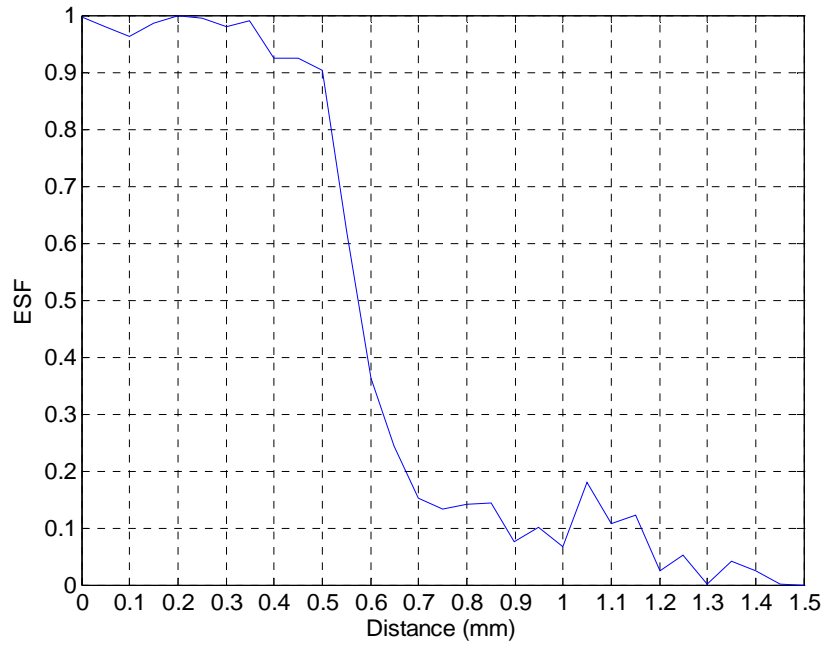
$$LSF(x) = a + \frac{1}{1 + [\lambda(x-b)]^2} \quad (4.2)$$

$$LSF(x) = a + \exp[-\lambda(x-b)^2]$$

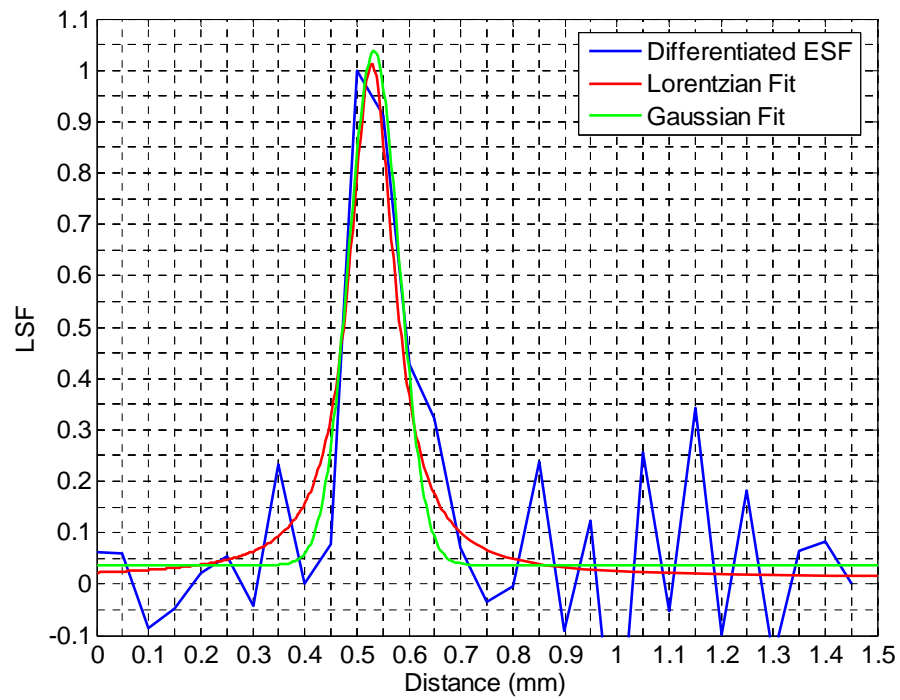
Using the same gadolinium foil and the same image plate system a FWHM spatial resolution of 93- μm was obtained at the neutron radiography facility NEUTRA located at PSI in Switzerland [79]. The difference in the values can be accounted for by the difference in the L/D effect used to take the radiograph which is confirmed by the resolution obtained by the PSF simulation done above for the image plates.

Table. 4.6. The LSF data for the image plate.

Image Plate LSF	a	b	λ	Norm	FWHM (μm)
Experimental	-	-	-	-	119
Lorentzian fit	0.0125	0.5288	18.8728	0.7044	106
Gaussian fit	0.0372	0.5328	214.7850	0.0421	113



(a)



(b)

Fig. 4.16. (a) ESF obtained from the image plate and (b) LSF for the image plate.

4.3 Comparison with other Neutron Imaging Facilities

The designed collimator and its estimated performance were compared with other existing facilities whose characteristics could be obtained from the literature. The comparison has been summarized in table 4.7. From the table it can be observed that our facility compares well with many of the existing facilities. But there are facilities with very long beam lines which makes their L/D much larger than our facility. The constraint of space restricts us from going to the larger values. But our facility compares very favorably in terms of TNC and the N/G value. It can be concluded that our facility has moderate flux with a high quality beam.

Table 4.7. Comparison table of some NR facilities.

Imaging Facility	Flux ($\text{cm}^{-2}\text{s}^{-1}$)	N/G	L/D	TNC	Filter Used	Other Characteristics
Our design	1.8x10 ⁶ 2.9x10 ⁶ 7.0x10 ⁶	1.34x10 ⁶ 4.5x10 ⁴ cm ² mR ⁻¹	150 150 100	Cd ratio 450 73.5% ASTM NC	6" Sapphire 4" Bismuth 6" Sapphire 6" Sapphire	Reactor source, Divergent collimator.
NIF at University of Texas [71]	5.2x10 ⁶	7.8x10 ⁶ cm ² mR ⁻¹	123	Cd ratio 3.6	3cm Bismuth	1MW TRIGA source, Divergent collimator, 22cm Beam size
NIST NIF [81]	5x10 ⁶ to 2x10 ⁷		300-600	79% ASTM NC	15 cm Cooled Bismuth Filter	20MW reactor source, 100micron resolution. 0.85" and 1.2o divergence angle colimation
NEUTRA at SINQ, PSI [82]	5x10 ⁶ 3x10 ⁶		350 550		5cm Bismuth	Spallation source SINQ, Divergent collimator, 11m beam line.
SPRR-300, Mianyang City China [83]	Max 4x10 ⁷	2x10 ¹⁰ cm ² Sv ⁻¹	60-660	Cd Ratio 4 – 150 Ajustable	55mm Lead, 45mm Bismuth plate	3.5MW Research Reactor, Film Real-time System.
ZPRL, INER Taiwan [84]	6.9x10 ⁵	~8.28x10 ⁵ cm ² mR ⁻¹	110	70%	Bismuth and Silicon	30kW Reactor, Collimator divergence angle 4.2°.
TRIGA MARK II Research Reactor Cornell University [85]	(6 ± 3)x10 ⁶		70-130		18 cm Sapphire 2.5" diameter	500kW steady state power shutdown on June 30, 2002.
Penn State Breazeale Reactor, Pennsylvania State University [86]	2.6x10 ⁶	~3.47x10 ⁵ cm ² mR ⁻¹	50-100	Cd Ratio 56		Divergent Collimator, Image size 22.9cm diameter.
NRAD Reactor Facility, Argonne National Laboratory-West [87]	~2.6x10 ⁶ ~4.3x10 ⁶	9.36x10 ⁴ 7.74x10 ⁴ cm ² mR ⁻¹	185-700 50-300	Cd Ratio 1.9 1.9		250 kW steady-state TRIGA reactor. Two horizontal, divergent, helium filled collimators.

Chapter 5

Conclusions and Future Work

5.1 Conclusion

This work describes the design of the Thermal Neutron Imaging Facility which has been built at the PULSTAR reactor at N.C. State University. The facility once completely setup will have the following types of neutron imaging capabilities:

- Film Radiography
- Digital Radiography
- Real-time radiography
- Computed Tomography

The collimator for the facility was designed using MCNP simulations. In the process of collimator simulation the MCNP cross-sections for sapphire which has been used as a neutron filter were also generated and verified. The usefulness of secondary collimation was also tested and was found to reduce the scattering noise at the image plane significantly without decreasing the flux. However, the possibility of increasing gamma-ray contamination due to neutron capture in the secondary collimator remains to be investigated. Also MCNP simulation of neutron radiographs and tomographs was done and the effect of scattering on the image quality was observed qualitatively. Furthermore, the PSF was simulated and was found to be in good agreement with the theoretically calculated value. The estimated parameters using MCNP are being tested with the experimental results as once they become available. Some of the key parameters like the neutron flux, the N/G ratio, the ASTM standards, and the resolution using the

line spread functions has already been tested and verified.

5.2 Future Work

5.2.1 Facility Improvements

The immediate future task is the setup of the real-time imaging system and the tomography setup and its verification. After the full setup of the facility the time resolution and the spatial resolution of the real-time system will be tested and if needed it will be improved. The fabrication and the installation of a secondary collimator will also be explored. The secondary collimator will be used only when it is required.

After the full verification of all the systems, a possible upgrade is to install the cooling system for the beam filters. The cooling to liquid nitrogen temperature is not necessary for sapphire but for beryllium cooling increases the flux by ~125% as has been mentioned in chapter 3. Cooled beryllium is often used to get cold neutron beam. Therefore with the installation of a cooling system and a beryllium filter cold neutron imaging will be possible. Cold neutron imaging is better suited for some applications than thermal neutron imaging. One of the applications where cold neutrons are better suited is imaging of radioactive wastes which are encapsulated in thick lead casks [88]. Lead has lower attenuation for cold neutrons than thermal neutrons. This makes the cold neutron images clearer even when they are placed inside the thick lead containers. Also with the cold neutron beam the difference in Bragg's cut off for different materials can be utilized for imaging and differentiation of crystalline materials.

For energy selective neutron imaging and time-of-flight experiments a neutron velocity selector may also be installed on the beam line. Energy selective neutron imaging has some further applications. Material discrimination becomes much easier with energy selective

imaging. Also it becomes possible to suppress some material in the sample radiograph to obtain more contrast for the material of interest. Table 5.1 lists the wavelengths of neutrons for different materials at which their attenuation becomes equal [89]. If these materials need to be suppressed in a radiograph then simply radiograph needs to be taken at the two given wavelength and then they have to be divided. A sample radiograph of suppression of material using this technique is shown in Fig. 5.1 [89]. It can be observed in the figure that after division the outer steel cover becomes almost invisible.

Table 5.1. Neutron wavelength pairs with an equal attenuation coefficient for different materials [89].

Material	λ_1 (Å)	λ_2 (Å)	Att. coefficient (cm ⁻¹)
Fe	2.68	6.39	1.16
	3.21	6.92	1.23
	3.78	5.38	0.96
Cu	2.95	4.27	0.97
	3.48	5.12	1.13
Pb	2.68	3.74	0.18
	6.39	7.45	0.07
Al	2.58	3.48	0.14
	4.01	5.33	0.10
	6.39	7.45	0.11
Plexiglas	6.39	7.45	3.30
Teflon	2.95	4.27	0.31
	5.28	7.42	0.40

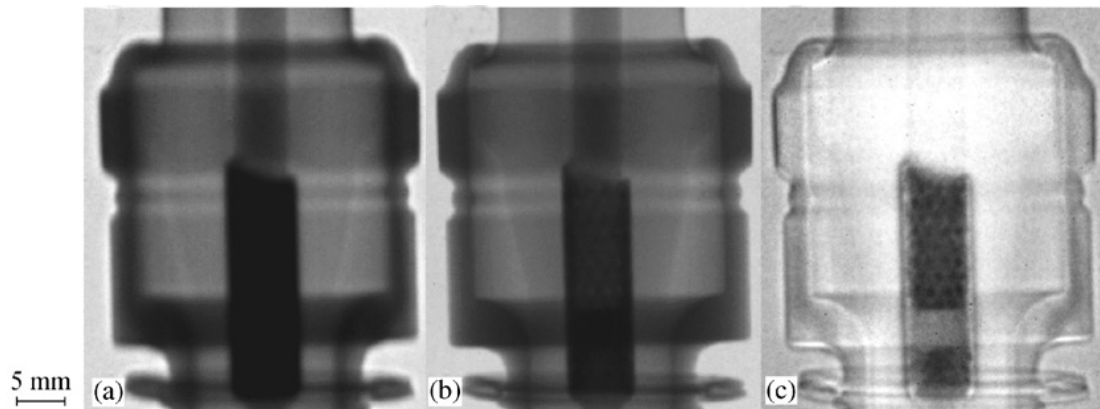


Fig. 5.1. Radiograph of a spark plug at (a) 6.9 Å (b) 3.2 Å (c) Division of the two radiographs [89].

5.2.2 Phase Contrast Imaging

Phase contrast imaging with neutrons is also intended to be performed with this facility. In the phase contrast image, both the amplitude and phase information is used to increase the contrast of the object's radiograph. It can be recalled from basic physics that when a wave changes its travel medium (change of refractive index) then a phase shift occurs in the wave. On traveling certain distance these invisible phase shifts transforms into visible intensity variations [90]. This downstream image formation due to variation in intensity is called the 'phase-contrast image' because it is enhanced by Fresnel diffraction, since interference due to phase differences corresponding to edge effects has had a chance to develop. An example of neutron phase-contrast is shown in Fig. 5.2 [91].

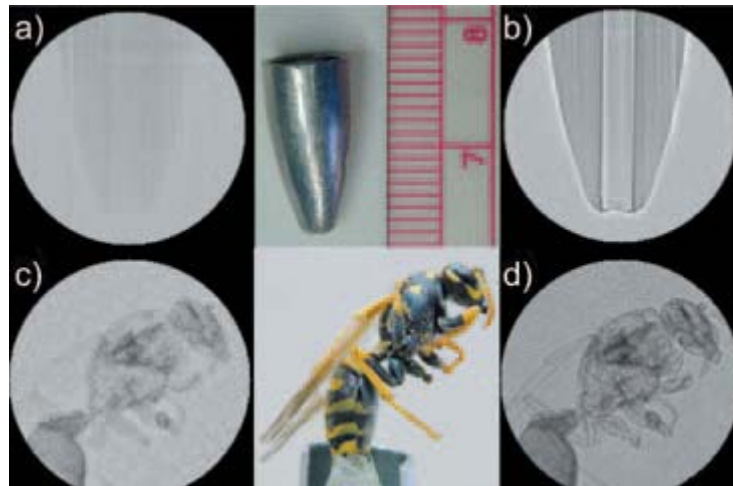


Fig. 5.2. (a) Contact (b) Phase contrast image of a lead sinker shown between them (c) Contact (d) Phase contrast image of a wasp [91].

References

- 1) "Neutron Radiography- Methods, Capabilities, and Applications," by Harold Berger, Elsevier Publishing Company, New York 1965.
- 2) "Uncovering Hidden Defects," Neutron radiography, Lawrence Livermore National Laboratory S & TR May 2001.
- 3) Faw R.E, Shultis J.K, "Radiological Assessment: Sources and Exposures," Prentice Hall New Jersey, 2nd Edition, 1993.
- 4) Berger H, Neutron Radiography- Annual Reviews, Argonne National Laboratory, Illinois, 1971.
- 5) Barton, J. P. Berger, H. Cutforth. Hinsdale, Proc. 16th Conf. Remote Systems Technology, American Nuclear Society 276-288, 1969.
- 6) Heuser B.J, Summerfield G.C, King J.S, "Deuterium trapping at metal defects," UIUC, Engineering research, Nuclear materials, radiation effects and radiological wastes.
- 7) Tamaki Masayoshi, Hara Shigeki et.al., "Visualization and analysis of forced diffusion of hydrogen in palladium by electrotransport," Nuclear Instruments and methods in physics A, 377, 166-169, 1996.
- 8) Takenaka Nobuyuki et.al., "Application of Neutron Radiography to visualization of cryogenic fluid boiling two-phase flows," Nuclear Instruments and methods in physics A, 377, 174-176, 1996.
- 9) Takenaka Nobuyuki et.al., "Void fraction distribution measurement in two-phase flow by real-time neutron radiography and real-time image processing," Nuclear Instruments and methods in physics A, 377, 174-176, 1996.
- 10) H. Kallmann Research 1 (1948), 254-260.

- 11) O.Peter, Z. naturforschung 1 (1946) 557-559.
- 12) Fischer Carl-Otto, The History of the First Neutron Radiographs in Berlin 1935-1944, Neutron Radiography Proceedings of the 4th World Conference, San Francisco California, May 10-16, 1992, 3-9.
- 13) Barton J.P, Opening Speech, Second World Conference on Neutron Radiography, 13-14.
- 14) Katsurayama Kosuke, Present Status of Neutron Radiography in Japan, Second World Conference on Neutron Radiography, 33-35.
- 15) Markgraf J.F.W., Neutron Radiography Working Group- Summary of activities and publications, International Neutron Radiography Newsletter, Second World Conference on Neutron Radiography, 59-67.
- 16) Domanus J.C., International Neutron Radiography Newsletter, Second World Conference on Neutron Radiography, 55-58.
- 17) Neutron Radiography, Proceedings of the Third World Conference 1989. Edited by S. Fujine et al. Hardback book 1011 pages, Kluwer Academic Publishing, Dordrecht, Holland ISBN 0-7923-0832-8.
- 18) Neutron Radiography System Design and Characterization 1995. edited by H. Kobayashi et al, hardback book 180 pages, North-Holland, Elsevier Science Publishing.
- 19) Nondestructive Testing and Evaluation - WCNR6 1999. Edited by S. Fujine et al, soft back book 455 pages, Gordon and Breach Science Publishers, Vol 16, No2-6, 2001.
- 20) Barton J.P., History and Foundation of ISNR, www.isnr.de .
- 21) Berger H, Advances in neutron radiographic techniques and applications: a method for nondestructive testing, Applied Radiation and Isotopes, 61, 437-442, 2004.
- 22) Annual Book of ASTM Standards, Section 3, Metals Test Methods and Analytical

- Procedures, 1999.
- 23) "Collimators for Thermal Neutron Radiography-An Overview," Compiled by Domanus J.C., D.Reidel Publishing Company, 1987.
 - 24) Barton J.P. 1967. *Material Evaluation*. 25: 45A-46A
 - 25) Giannini M, Pugnetti G, Ramorino M.C, Trezza G, "Neutron radiography facility for inspecting reactor fuel elements at C.S.N. Casaccia, RT/FI (78) 17, November 1978.
 - 26) Tyufyakov N.D., Shtan A.S. *Principles of Neutron Radiography*. Atomizdat Publishers. Moscow 1975.
 - 27) Barton J.P., Perves J.P.. Underwater neutron radiography with conical collimator. *British Journal of Non-Destructive Testing*. December 8, 1966, 79-83.
 - 28) Richards W.J., Petersen R.T., Prindle J.A., "The neutron radiography facility at the 3-MW Livermore pool-type reactor," UCRL-51906, 10.09.75.
 - 29) Janson C.N., Barton J.P. Jr, Proudfoot E.A, "Neutron radiography at the Hanford Engineering Development Laboratory," *Materials Evaluation*, June 1979, 55-61.
 - 30) Laporte A., Boulaumie J.P., "Neutron Radiography applied to the development of quality control of the pyrotechnic systems of the Ariane launcher," Paper 4K-3. Ninth World Conference on Non-Destructive Testing. Melbourne 1979.
 - 31) Bayon G., Laporte L., Gal J. Le, "A review of then years of operation of the industrial neutron radiography facilities associated with the Triton reactor at the Fontenay-aux-Roses nuclear research center," 67-76.
 - 32) Kok K.D., "Neutron Radiography of nuclear fuels at the Batelle research reactor," *ASTM STP* 1976, 183-194.
 - 33) Maene N., Tourwe H., Mostin N., Pleckmans E., "Quality control of plutonium oxide fuel

- elements by neutron radiography,” IAEA Vienna 1976, 323-331.
- 34) P. von der Hardt, Rottger H., (editors) Neutron radiography handbook. D. Reidel Publishing Co., Dordrecht/Boston/London. 1981.
- 35) Rogers J.D., “Cold neutron spectra of the General Atomic Triga MRF neutron radiography facility,” Proceedings of the First World Conference, San Diego, California, USA. 977-981
- 36) Swanson F.R., Kuehne F.R., “Neutron radiography with a van de Graaf accelerator for aerospace applications,” ASTM STP 1976, 158-167.
- 37) Neutronographie. Installations et applications auprès des reacteurs experimentaux du Centre d’Etudes Nucleaires de Grenoble. PJ/SEREG 910-237/81. 1981.
- 38) Practical Neutron radiography, Edited by Domanus J.C, NRWG, published by Kluwer academic publishers.
- 39) Hawkesworth, M.R, Neutron radiography: equipment and methods, Atomic energy review, 15 No. 2, 169-220, 1977.
- 40) Mildner D.F.R, Arif M., Stone C.A, “Neutron transmission of single crystal sapphire filters,” J. Appl. Cryst., 26, p438-447, 1993.
- 41) Brugger R.M, “A single crystal silicon thermal neutron filter,” Nuclear Instrum. Methods, 135, 289-291, 1976.
- 42) Adib M, Kilany M, “On the use of bismuth as a neutron filter,” Radiation physics and chemistry, 66, 81-88, 2003.
- 43) Tennant D.C, “Performance of a cooled sapphire and beryllium assembly for filtering of thermal neutrons,” Review of Sci. Instrum., 59 (2), February 1988.
- 44) Lehmann E.H, Vontobel P, Frei G, Bronnimann C, “Neutron imaging- detector options and practical results,” Nuclear instrum. methods A, 531, 228-237, 2004.

- 45) Harms A.A, Wyman D.R, Mathematics and physics of Neutron radiography, D. Reidel Publishing Company, 1986.
- 46) Hawkesworth M.R, "Films for neutron radiography: an investigation of film-intensifying screen image recorders," J. of Scient. Insts., Series 2, Vol 2, 235-242, 1969.
- 47) Allen Elizabeth, Latent Image Formation: The characteristic curve, How imaging Works, Module 2DPI403.
- 48) Mees C.E.K, James T.H, The Theory of Photographic Process, 3rd Edition, London: Collier-Macmillan, 1966.
- 49) Thoms M, Myles D, Wilkinson C, "Neutron detection with imaging plates Part-I Image storage and readout," 26-33, Nuclear Instruments and Methods in Physics Research A 424.
- 50) Takahashi Kenji, Tazaki Seiji, Miyahara Junji, Karasawa Yuuko, Niimura Nobuo, "Imaging performance of imaging plate neutron detectors," Nuc. Inst. and methods. In Phy. Res. A, 377, 119-122, 1996.
- 51) M. Thoms, H. von Seggern, A. Winnacker, Phys. Rev. 44 (17) (1991) 9240.
- 52) Metz C.E, Doi K, "Transfer function analysis of radiographic imaging systems," Physics in medicine and biology, 24, 1079, 1979.
- 53) Harms A.A, Zeilinger A, "A new formulation of total unsharpness in radiography," Physics in medicine and biology, 22 No.1, p70-80, 1977.
- 54) Day M.J, "Specification and additivity of unsharpness in diagnostic radiology," Physics in medicine and biology, 21 No 3, p399-405, 1976.
- 55) Harms A.A, Garside B.K, Chan P.S.W, "Edge-spread function in neutron radiography," Journal of applied physics, 43, p3863-3867, 1972.
- 56) Hofmann J, Rausch C, "Performance of a prototype detector system for thermal neutron

- based on laser stimulated luminescence,” Nuclear Instruments and Methods in Physics Research A, 355, 494-500, 1994.
- 57) Rossmann K, “Point spread-function, Line spread-function and Modulation transfer function,” Radiology, 93, 257, 1969.
- 58) Richard Bossi, Oien Charles, Paul Mengers, Real-time radiography, Section 14, The nondestructive testing handbook on radiography and radiation testing.
- 59) Menezes de M.O, Pugliesi R, Pereira M.A.S, Andrade M.L.G, Real time neutron radiography at IEA-R1m Nuclear Research Reactor, Brazilian Journal of Physics, 33, June 2003.
- 60) Dove E.L, Notes on Computerized Tomography, Physics of Medical Imaging.
- 61) Image Processing Toolbox, MATLAB Release 14 with Service Pack 1.
- 62) *Visitors Guide to the NCSU Pulsar Reactor*, Raleigh, NC, n.p., n.d.
- 63) Berger H, International Journal of Applied Radio Isotopes 15:407-414.
- 64) An Investigation of Neutron Collimators and their Application in Neutron Radiography. MS thesis, R. Morris. Univ of New Mexico, 76pp.
- 65) B.L. Blanks, D.A. Garrett, R. Morris, Proc. 5th Int. Conf. Nondestructive Test., Ottawa, 242-47, 1969.
- 66) Barton J.P., Perves J.P. 1966, British J. Nondestructive Testing. 8: 79-83.
- 67) Barton J.P. 1967. Material Evaluation. 25: 45A-46A.
- 68) Heat Resistant shielding catalog No- 277, Thermo Electron Corporation, www.thermo.com.
- 69) Mildner D.F.R, Lamaze G.P, “Neutron transmission of single crystal sapphire,” J. Appl. Cryst., 31, 835-840, 1998.
- 70) MCNP- A general Monte Carlo N-Particle Transport Code Version-5, X-5 Monte Carlo

Team, Diagnostics Application Group, LANL.

- 71) Jo Young Gyun, "Development of thermal neutron imaging facility for real time neutron radiography and computed tomography," PhD Dissertation, University of Texas at Austin USA, 1998.
- 72) Kresse G, Furthmuller J, Vienna Ab-Initio Simulation Package; VASP the Guide, Vienna, 2002.
- 73) Cassels J.M, Prog. Nucl. Phys. 1, 185-215, 1950.
- 74) Kittel C, Introduction to Solid State Physics, 7th Edition, Wiley, New York, 115-140 (Chapter 5), 1996.
- 75) Freund A.K, "Cross-section of materials used as neutron monochromators and filters," Nuclear Instruments and Methods, 213, 495-501, 1983.
- 76) G Jo. Young, Spiesman W.J, Abdurrahman N.M, "Development of a Neutron Imaging Facility at the University of Texas TRIGA reactor," IEEE, 1996.
- 77) Phosphor/Scintillator Data sheet 40, Applied Scintillation Technologies, USA.
- 78) Warzak B, Personal Correspondence with Midwest Optical Systems, Palatine, IL, 9th Oct 2004.
- 79) Kolbe H, Lehmann E, Gunia W, Korner S, "Applications and characteristics of imaging plates as detectors in neutron radiography at SINQ," Nuclear Instruments and Methods in Physics Research-A, 424, 40-47, 1999.
- 80) Baker R, Personal Correspondence with Applied Scintillation Technologies, Annapolis, MD, 1st June 2005.
- 81) Hussey D, Jacobson D.L, Arif M, Huffman P.R, Cook J.C, Williams R.E, Schröder I, Richards W, "New Neutron Imaging Facility at NIST," Presentation Talk, July 2004.

- 82) Vontobel P, Lehmann E, Frei G, "Performance characteristic of tomography setup at the PSI NEUTRA thermal neutron radiography facility," Report, PSI, Villigen, Switzerland.
- 83) Bin Tang, Zhang S, Zhu S, Xia M, The design of Neutron radiography facility and its application in SPRR-300, Report, Institute of Nuclear Physics and Chemistry of China Academy of Engineering Physics, Mianyang City, China.
- 84) Chia Wie-Min et.al., "Case studies of neutron radiography examination at INER," Nuclear Instruments and Methods in Physics Research- A, 377, 16-19, 1996.
- 85) Deimert M.R, Lowe C.W, Parlange J.Y, Unlu K, Cady K.B, "Performance and calibration of a Neutron Image Intensifier Tube based real-time radiography system," IEEE Transactions on Nuclear Science, 52, 1, 2005.
- 86) <http://www.anlw.anl.gov/nr/usa-25.htm>
- 87) <http://anlw.inel.gov/nr/usa-14.htm>
- 88) Baechler S, Kardjilov N, Dierick M, Jolie J, Kuhne G, Lehmann E, Materna T, "New features in Cold Neutron Radiography and Tomography- I," Nuclear Inst. and Methods in Phys. Res. A, 491, 481-491, 2002.
- 89) Kardjilov N, Baechler S, Basturk M, Dierick M, Jolie J, Lehmann E, Materna T, Schillinger B, Vontobel P, "New features in Cold Neutron Radiography and Tomography- II," Nuclear Inst. and Methods in Phys. Res. A, 501, 536-546, 2003.
- 90) Nugent K.A, Paganin D, Gureyev T.E, "A Phase Odyssey, Physics Today," 27-32, August 2001.
- 91) Jacobson D.L, Arif M, Werner S.A, Allman B.E, McMahon P.J, Nugent K.A, Paganin D, "Phase-Contrast Imaging with Neutrons," Research Highlights, NIST.